8-2006

Thermodynamic Characterization of Polymeric Materials Subjected to Non-isothermal Flows: Experiment, Theory and Simulation

Tudor Constantin Ionescu
University of Tennessee - Knoxville

To the Graduate Council:

I am submitting herewith a dissertation written by Tudor Constantin Ionescu entitled "Thermodynamic Characterization of Polymeric Materials Subjected to Non-isothermal Flows: Experiment, Theory and Simulation." I have examined the final electronic copy of this dissertation for form and content and recommend that it be accepted in partial fulfillment of the requirements for the degree of Doctor of Philosophy, with a major in Chemical Engineering.

Brian J. Edwards, David J. Keffer, Major Professor

We have read this dissertation and recommend its acceptance:

John R. Collier, James R. Morris

Accepted for the Council:

Carolyn R. Hodges

Vice Provost and Dean of the Graduate School

(Original signatures are on file with official student records.)

To the Graduate Council:

We are submitting herewith a dissertation written by Tudor Constantin Ionescu entitled "Thermodynamic Characterization of Polymeric Materials Subjected to Non-isothermal Flows: Experiment, Theory and Simulation". We have examined the final electronic copy of this dissertation for form and content and recommend that it be accepted in partial fulfillment of the requirements for the degree of Doctor of Philosophy, with a major in Chemical Engineering.

Brian J. Edwards
Major Professor

David J. Keffer
Major Professor

We have read this dissertation
and recommend its acceptance:

John R. Collier

James R. Morris

Accepted for the Council:

Anne Mayhew
Vice Chancellor and Dean of
Graduate Studies

(Original signatures are on file with official student records)

THERMODYNAMIC CHARACTERIZATION OF POLYMERIC MATERIALS SUBJECTED TO NON-ISOTHERMAL FLOWS: EXPERIMENT, THEORY AND SIMULATION

A Dissertation
Presented for the
Doctor of Philosophy
Degree

The University of Tennessee, Knoxville

Tudor Constantin Ionescu
August 2006

ACKNOWLEDGEMENTS

This work would not have been possible without the guidance and support of my advisor, Dr. Brian Edwards, to whom I am greatly indebted for giving me a second chance. I would also like to thank my co-advisor, Dr. David Keffer, first for teaching me the basics of Molecular Simulation and numerical methods, and last but not least for invaluable advice leading to the completion of this work. The Monte-Carlo codes used in this study are the product of years of development at the University of Patras in Greece, and Dr. Vlasis Mavrantzas was kind enough to lend them to us for use in this work. I would also like to thank Dr. Simioan Petrovan for making me familiar with the equipment in our laboratory and for the helpful discussions we have had regarding the experimental part of this project. On the same note, I would like to thank Doug Fielden from our mechanical shop for manufacturing essential parts used in the experiments. The computational resources used for the simulation part of this study were provided through UT-CSI by generous allocations of CPU time on one of the massively parallel supercomputers at ORNL – Cheetah, and through the SInRG cluster here at the University of Tennessee by granting access to the public node. The financial support for this research was provided by the donors of the Petroleum Research Fund, administered under Grant No. 41000-AC7.

ABSTRACT

Frictional or viscous heating phenomena are found in virtually every industrial operation dealing with processing of polymeric materials. This work is aimed at addressing some of the existing shortcomings in modeling non-isothermal polymer flowing processes. Specifically, existing theories suggest that when a polymer melt is subjected to deformation, its internal energy changes very little compared to its conformational entropy. This statement forms the definition of the *Theory of Purely Entropic Elasticity* (PEE) applied to polymer melts. Under the auspices of this theory, the temperature evolution equation for modeling the polymer melt under an applied deformation is greatly simplified. In this study, using a combination of experimental measurements, continuum-based computer modeling and molecular simulation techniques, the validity of this theory is tested for a wide range of processing conditions. First, we present experimental evidence that this theory is only valid for low deformation regimes. Furthermore, using molecular theory, a direct correlation is found between the relaxation characteristics of the polymer and the flow regime where this theory stops being valid. We present a new and improved form of the temperature equation containing an extra term previously neglected under the PEE assumption, followed by a recipe for evaluating the extra term. The corrected temperature equation is found to give more accurate predictions for the temperature profiles in the high flow rate regimes, in excellent agreement with our experimental measurements. Next, in order to gain a molecular-level understanding of our experimental findings, a series of polydisperse linear alkane systems with average chain lengths between 24 and 78

carbon atoms are modeled with an applied "orienting field" using a highly efficient non-equilibrium Monte Carlo scheme. Our simulation results appear to substantiate our experimental findings. The internal energy change of the oriented conformations is found to be similar in magnitude with the free energy change, indicating that it is not reasonable to be neglected from a macroscopic energy balance. Furthermore, the inter-molecular interactions are found to play a crucial role in the energy balance of the system, which explains why PEE is not obeyed when high degrees of orientation are achieved. In the end, a structural study is performed on highly oriented configurations of *n*-eicosane generated through steady-state non-equilibrium molecular dynamics (NEMD). We compare the simulated oriented structures to x-ray diffraction data for crystalline *n*-eicosane, and conclude that a crystalline precursor is formed during the simulations.

TABLE OF CONTENTS

LIST OF TABLES

LIST OF FIGURES

Chapter 1

Introduction

1.1 The Elastic Behavior of Polymeric Materials

At the beginning of the last century, polymers emerged as a new class of chemical compounds. Even though naturally occurring polymers have been used for quite some time before that (natural rubber), it wasn't until 1909 that the Poly-Phenol-Formaldehyde (PPF or Bakelite) resin was synthesized. Since then, a variety of other polymers were discovered and mass-produced. For example, Polystyrene (PS) (1930), Polyamide (Nylon) (1935), Poly-Vinyl-Chloride (PVC) (1938), Polyethylene (PE) (1939), Polyurethane (PU) (1940) are just a few of the most important ones.

We now live in a time when polymers are replacing traditional materials in almost every application. From the synthetic fibers that are replacing cotton, silk and wool in the clothes that we wear to the highly complex composite materials replacing metals in the automotive industry, polymers are playing an increasingly important role in almost every aspect of our everyday life.

Understanding the behavior of polymeric materials under industrial processing conditions has generated a tremendous amount of interest among engineering

communities over the past fifty years. This is due to a continuous growth of the polymer industry, driven by an increasing number of polymers being discovered and also an increasing number of applications in which polymers are used. It has been estimated that the polymer industry in the United States has surpassed the steel, copper and aluminum industries combined.

When subjected to industrial processing operations, polymeric materials undergo repeated deformations, associated with heating, cooling and phase transitions. To understand properly the thermodynamics and energy balance of such operations, it is necessary to understand fully the structure-property relationships exhibited by polymers at all length and time scales. It is well known that for a polymeric material, the final mechanical and thermal properties are greatly affected by its processing history. For example, the crystallinity of a polymer can be controlled by simply adjusting the cooling rate in conjunction with an applied deformation. Even though most processing operations are non-isothermal, the research in this area has been focused primarily on isothermal deformations of polymeric materials.

§1.1.1 *General Equations*

In a typical engineering analysis of an incompressible, isothermal polymeric flow, one has to solve a set of equations for the conservation of mass (eq. 1.1), momentum (eq. 1.2) and an appropriate constitutive equation that relates the stress to the strain rate (eq. 1.3). For example, in the case of the Upper-Convected Maxwell Model (UCMM), one has the equation set [1, 2]

$$\frac{\partial \rho}{\partial t} = -\left(\nabla \cdot \rho \mathbf{v}\right) = 0 \tag{1.1}$$

$$\rho \frac{D\mathbf{v}}{Dt} = -\nabla p - \left[\nabla \cdot \tau\right] + \rho g \tag{1.2}$$

$$\overset{\nabla}{\tau}_{\alpha\beta} + \frac{1}{\lambda}\tau_{\alpha\beta} = G\left(\nabla_\alpha v_\beta + \nabla_\beta v_\alpha\right) \tag{1.3}$$

along with appropriate initial and boundary conditions, where **v** is the velocity vector field, ρ is the fluid mass density, p is the hydrostatic pressure, τ is the extra stress tensor, G is the elastic modulus and λ is the relaxation time. The superimposed reverse hat denotes the upper-convected time derivative. In the non-isothermal case, when the temperature is taken as a variable, one has to add the energy conservation equation (eq. 1.4) to the above set of equations:

$$\rho \frac{D\hat{U}}{Dt} = -\left(\nabla \cdot q\right) - p\left(\nabla \cdot \mathbf{v}\right) + \left(\tau : \nabla \mathbf{v}\right) \tag{1.4}$$

where $\hat{U}$ is the internal energy per unit mass and q is the heat flux vector field. It is important to note that the UCMM constitutive equation (eq. 1.3) has additional terms under non-isothermal conditions [1, 2].

§1.1.2 *Polymeric Materials with Purely Entropic Elasticity*

In equation 1.4, the internal energy on the left hand side is not a quantity that can be measured directly, and a simplification needs to be made. In thermodynamics, the Helmholtz free energy is defined as the difference between two components: internal energy and entropy multiplied by the temperature,

$$A \equiv U - TS \tag{1.5}$$

If we define the "rate of accumulation of elastic energy" $\dot{E}$ as,

$$\dot{E} \equiv \dot{A} + S\dot{T} \tag{1.6}$$

then the "rate of accumulation of elastic energy" becomes

$$\dot{E} = \dot{U} - T\dot{S} \tag{1.7}$$

In equations 1.6 and 1.7, the superimposed dot represents the substantial time derivative. For an isothermal process, the rate of accumulation $\dot{E}$ is identified with the rate of accumulation of Helmholtz free energy $\dot{A}$.

Let us examine now both ends of the rheological spectrum. When purely viscous fluids (Newtonian, if the stress is linear with strain rate) are subjected to deformation, their conformational entropy does not change. In other words, the internal structure of a volume element will be the same whether the deformation is present or not. There have been simulation studies reporting the onset of the so-called "string phase" when extreme shear rates were applied to monatomic fluids [3, 4]. The authors of these studies however, have explained the existence of the string phase as being an algorithmic artifact. The appearance of ordered phases at extreme shear rates was eliminated when the systems were thermostated by fixing the configurational temperature, instead of the kinetic energy [3]. Therefore, it would be safe to assume that purely viscous fluids can accumulate elastic energy only by compression, thus by an increase in internal energy,

$$\dot{E} = \dot{U} \tag{1.8}$$

On the opposite side of the spectrum we find the rubbery solids, which under the very successful Theory of Rubber Elasticity (TRE) [5] are considered to accumulate

elastic energy exclusively through a decrease in conformational entropy. The significant decrease in conformational entropy is associated with the lower number of degrees of freedom of the extended chains:

$$\dot{E} = -T\dot{S} \tag{1.9}$$

Polymeric melts on the other hand, which are *viscoelastic* in nature, are treated as either simple fluids with fading memory [6, 7] or as cross-linked networks with temporary junctions [8].

Astarita and co-workers [9-12] set the basis for what it is known today as the *Theory of Purely Entropic Elasticity* (PEE) as applied to polymer melts, and have made the assumption that the internal energy of a polymeric fluid is a unique function of temperature, thus independent of deformation. Mathematically, this can be written as

$$\hat{U} = \hat{U}(T) \tag{1.10}$$

The immediate consequence of equation 1.10 is that the constant volume heat capacity per unit mass, defined the usual way as the derivative of the internal energy with respect to temperature at constant density, will also be independent of deformation:

$$\hat{c}_v = \frac{\mathrm{d}\hat{U}(T)}{\mathrm{d}T} \tag{1.11}$$

Based of the assumption of PEE, the energy conservation equation 1.4 can be greatly simplified and can be written in essentially the classical way:

$$\rho\hat{c}_v \frac{DT}{Dt} = -(\nabla \cdot q) - p(\nabla \cdot \mathbf{v}) + (\tau : \nabla\mathbf{v}) \tag{1.12}$$

We now have a more useful form of equation 1.4 written in terms of temperature, which is an easily measurable quantity. We should point out that equation

1.12 is exactly the same as for Newtonian fluid, and there is no explicit information related to the internal structure or conformation of the fluid, except only indirectly through the stress tensor.

1.2 Review of Previous Work

Driven by the explosive growth of the polymer industry since the 1940's, the engineering community recognized the need to study and characterize these materials at the greatest depth. Particularly, much information was needed in relation to the energy balances associated with deformation under processing conditions.

Recent advances in atomic force microscopy have made it possible to measure the mechanical properties of polymers at the molecular level. Consequently, a considerable amount of effort has been dedicated to measuring the elastic response of single polymer chains in various media [13-16]. The general consensus is that when single polymer chains are extended, their elastic response can entirely be attributed to a decrease in conformational entropy. A recent molecular simulation study appeared to substantiate this idea [17, 18]. In this study, the authors measured the elastic response of a single chain placed in a simulation box, which was then filled with a solvent (either chemically different or similar to the single chain). The authors then proceeded to extend the chain and map out the chain free energy using the "umbrella sampling" technique, while keeping the surrounding solvent at equilibrium. They concluded that unless the chain reaches its maximum extension length, the internal energy of the

system does not change. By definition, the chain adopts its maximum extension when all the torsional angles are in the *trans* conformation, while the bond angles and bond lengths are at their equilibrium values. Clearly, the internal energy increase observed at the highest extensions was due to modifications in bond angles.

As will be shown in Chapter 3, our simulation results suggest that when a polymer melt (or an ensemble of chains) is stretched, the most important contributor to the change in internal energy is the inter-molecular non-bonded energy. The two other major contributors are the torsional energy and the intra-molecular non-bonded energy. The two latter components are of about the same magnitude and of opposite sign, offsetting each other. We believe that the results obtained in the abovementioned study are not at all surprising. The medium surrounding the extended polymer chain was kept at equilibrium, thus the change in the non-bonded inter-molecular energy was negligible. In reality, when a polymer melt experiences deformation, the macromolecular chains tend to align in the direction of the deformation, establishing more favorable side interactions with the neighboring chains. This plays a major role in the energy balance of the system, because these favorable interactions lower the inter-molecular non-bonded energy significantly. In extreme cases, the oriented melts experience the phenomenon called "flow-induced crystallization". Indeed, we have shown evidence of crystalline-like structures forming during simulation of n-eicosane subjected to planar elongational flow [19] (also, see Chapter 4).

If we examine the internal structure of cross-linked rubbery solids, the chain segments connecting two network nodes can be modeled as isolated chains. When an

external deformation is applied, it is very difficult for the chain segments to establish favorable side interactions with neighboring chains, given the random distribution of the network nodes and the segment lengths. Thus, the inter-molecular interactions will be independent of deformation. Therefore, the energy accumulated through deformation will be entirely associated with a decrease in conformational entropy, as stipulated in TRE [5].

When the *Theory of Purely Entropic Elasticity* was applied to polymer melts, its authors attempted to test it experimentally. In their experimental procedure, the temperature increase due to viscous heating for planar shear flow and uniaxial elongational stretching was measured [10, 11]. Two different polymers were tested: Polyisobutylene (PIB) and Polyvinylacetate (PVA). From a theoretical perspective, they simplified the heat equation 1.4 by assuming a Purely Entropic Fluid (eqns. 1.10 and 1.11) by neglecting heat conduction effects and by considering the fluid homogenous; they subsequently solved equation 1.4 for the heat capacity in the transient regime. Under the experimental conditions, only PIB was found to be purely entropic in nature, while PVA was not. For PIB, the heat capacity was found to converge to the same value for all deformation rates investigated, thus concluding that equation 1.12 was obeyed, and that the PEE assumption used to derive it was reasonable. We believe that there are two main reasons why energetic effects were not captured by these early experiments: first, the spectrum of deformation rates employed was too low (up to 2.78 s^{-1}) ; second, the flow was homogeneous (i.e. there were no spatial gradients in the degree of orientation); in Section 2.5, we will derive a more general form of the temperature

equation by not including the PEE assumption and we will show that there is an extra heat generation term arising from the spatial gradients of the degree of orientation. We also believe that their interpretation for the PVA experimental results was faulty. The evidence provided only suggests that PVA has a different transient behavior than PIB. The authors did not show clear evidence that the heat capacity is not a constant with respect to deformation rate, as they did in the PIB case.

However questionable these results were, they established the theory of PEE as universally applicable in non-isothermal polymer rheology. We are aware of no further attempts to prove this theory experimentally.

1.3 Theoretical Deviations from the Theory of Purely Entropic Elasticity

Virtually all engineering analyses and commercially available software for modeling non-isothermal flow of polymeric fluids use equation 1.12 to describe the temperature evolution of the system. As Astarita and co-workers pointed out in their study, this approach has its limitations [9]:

> "The implications of this conclusion are very important in the engineering analysis of such polymer processing operations as extrusion and injection molding, where frictional heating is a crucial phenomenon. Polymer melts are known to be non-linear viscoelastic materials, and unless the assumption embodied in (eq. 1.10) is made, their frictional heating behavior *would not* be described by (eq. 1.12)."

Let us examine now the complete form of the temperature evolution equation if we do not make the assumption that the free energy is purely entropic in nature. First, we have to consider that aside from temperature, the internal energy of the fluid has an explicit dependence on one or more internal structural variables. In this case, the most widely used quantity to describe the internal structure of a polymer melt is the conformation tensor, **c**, which is defined as the second moment (dyadic product) of the end-to-end vector **R**, taken as an ensemble average:

$$\mathbf{c} \equiv \langle \mathbf{RR} \rangle \tag{1.13}$$

If we consider both temperature and conformation tensor functionalities of the internal energy, then the constant volume heat capacity per unit mass will be defined as the partial derivative of the internal energy with respect to temperature, at constant **c**:

$$\hat{U} = \hat{U}(T, \mathbf{c}) \tag{1.14}$$

$$\hat{c}_v = \left. \frac{\partial \hat{U}}{\partial T} \right|_{\mathbf{c}} \tag{1.15}$$

Then, the substantial time derivative of the internal energy found on the left side of equation 1.4 becomes:

$$\frac{D\hat{U}}{Dt} = \hat{c}_v \frac{DT}{Dt} + \left. \frac{\partial U}{\partial \mathbf{c}} \right|_{T,V} : \frac{D\mathbf{c}}{Dt} = \hat{c}_v \frac{DT}{Dt} + \left. \frac{\partial \hat{U}}{\partial \mathbf{c}} \right|_{T,V} : \left(\frac{\partial \mathbf{c}}{\partial t} + \mathbf{v} \cdot \nabla \mathbf{c} \right) \tag{1.16}$$

The complete form of the temperature evolution equation is thus

$$\rho \hat{c}_v \frac{DT}{Dt} + \rho \left. \frac{\partial \hat{U}}{\partial \mathbf{c}} \right|_{T,V} : \left(\frac{\partial \mathbf{c}}{\partial t} + \mathbf{v} \cdot \nabla \mathbf{c} \right) = -(\nabla \cdot \mathbf{q}) - p(\nabla \cdot \mathbf{v}) + (\tau : \nabla \mathbf{v}) \tag{1.17}$$

We now have an additional term on the right side of equation 1.17 that does not appear in equation 1.12. This term contains the structural information missing in equation 1.12. In order to evaluate this term, one has to invoke a viscoelastic model, such as the UCMM or the Finitely Extensible Nonlinear Elastic model with the Peterlin approximation (FENE-P) [20] to relate the conformation tensor **c** to the rate of strain tensor. In Section 2.5, equation 1.17 will be discussed in detail, and the relative importance of the abovementioned additional term will be assessed using the UCMM and the single-mode Giesekus models. However, by careful choice of the flow system conditions, this term can be made to vanish. For example, if one is interested in the steady-state ($\partial \mathbf{c}/\partial t = 0$) of a homogenous flow ($\nabla \mathbf{c} = 0$), then equation 1.17 takes the same form as equation 1.12. Furthermore, in this case the heat capacity is no longer independent of deformation rate, as PEE would suggest (see equations 1.14 and 1.15).

Some recent theoretical studies have brought the validity of PEE into question [1, 2]. Using the UCMM, a new temperature evolution equation was derived without using the PEE assumption. The new temperature equation has additional terms not appearing in equation 1.12, and includes terms describing the relaxational fluid processes. Furthermore, the heat capacity is written as a sum of two terms; one that is the equilibrium heat capacity and an explicit contribution from the conformational structure of the polymer,

$$c = c_0 - \frac{1}{2}\alpha T\left(\mathrm{tr}(\mathbf{c}) - \mathrm{tr}(\mathbf{c}_0)\right)\frac{\partial^2 K(T)}{\partial T^2} \tag{1.18}$$

where, c_0 is the equilibrium heat capacity, α is a material constant and is a measure of the degree of elasticity per unit mass, $K(T)$ is the overall chain spring constant, $\mathbf{c}$ is the conformation tensor in the deformed state, and $\mathbf{c}_0$ is the conformation tensor in the unperturbed state. It is important to note that if $K(T)$ is a linear function of temperature, the second term on the right side of equation 1.18 vanishes. However, as we shall see later in Chapter 3, our simulation results seem to suggest that $K(T)$ is not a linear function of temperature, and the conformational contribution to the heat capacity can be significant. Furthermore, it is worth emphasizing that the functional form of equation 1.18 is based upon the relatively simplistic UCMM. Other, more physically realistic models would produce different functional forms.

The heat capacity represents the amount of heat necessary to raise the temperature of an object by one degree Kelvin. This amount of heat is directly related to the degrees of freedom of the smallest components of that particular material (atoms). When a polymeric material is subjected to deformation, the macromolecular chains tend to align in the direction of the deformation, which results in a decrease of the total number of degrees of freedom for the chains, or in other words a reduction in the heat capacity. Therefore, one would expect the heat capacity for an aligned system of macromolecules to be always smaller than the quiescent state value. Indeed, as we shall see later in §2.5.6 and §3.3.3, the heat capacity is decreasing as the deformation rate is increased for our model polymer (polyethylene).

1.4 Concluding Remarks

In this chapter, we have reviewed some basic theoretical aspects regarding the elastic response of polymeric materials. We have identified two fundamentally different elastic responses for purely viscous fluids and purely elastic rubbers in the sense that for the former, the accumulation of elastic energy is entirely due to internal energy change, while for the latter it is entirely attributed to the conformational entropy. Furthermore, we have made a clear distinction between the elastic behavior of polymer melts on one hand and the elastic behavior of single polymer chains and cross-linked polymer networks on the other. This distinction has been overlooked before, in the sense that polymer melts were assumed to obey the Theory of Purely Entropic Elasticity. We also identified an additional term in the temperature evolution equation, which contains internal structural information (equation 1.17).

In the following chapters, we will test the validity of the PEE assumption as applied to polymer melts. In Chapter 2, we will extend the experiments of Astarita and co-workers [10, 11] to test the validity of equation 1.12 for a much wider range of deformation rates. Equation 1.12 will be solved numerically using a finite element method after removing some of the simplifying assumptions in the original approach. This will provide the basis for comparison with the experimental measurements. Then, in Chapter 3 we will perform detailed atomistic molecular simulations under non-equilibrium conditions for a series of polydisperse linear alkane systems under the

influence of an applied orienting field. These simulations will be performed in order to help us get a better understanding of the experimental results.

Chapter 2

Rheology of Non-Isothermal Polymeric Flows

2.1 Introduction

When a polymeric material is subjected to deformation, it experiences the so-called "frictional or viscous heating" phenomenon. This phenomenon occurs in both types of flow known in rheology, namely shear and elongational flows. The "viscous heating" term appears in the energy balance of the system (eq. 1.4), and is defined as the double dot product between the stress tensor and the rate of strain tensor ($\tau : \nabla \mathbf{v}$). Therefore, designing any industrial process that involves flow of polymeric materials requires accurate predictions of this particular term. By contrast, in the case of low viscosity Newtonian fluids (such as water), the heat generated through frictional phenomena is negligible, except under extreme conditions.

In some typical industrial processing applications, polymeric materials are subjected to flow regimes that are either purely shear or elongational. Primarily, shear flow is found in operations such as capillary extrusion, while elongational processes include fiber spinning, film blowing and blow molding. In most cases, however, the

design engineer is faced with a mixture of the two, and accurate knowledge of both shear and elongational viscosities is needed.

While the experimental techniques for determining the shear viscosity as a function of deformation rate are very well established, elongational viscosity measurements are still largely in the developmental stage and subject to some controversy. This is due to an array of technical difficulties encountered in these flows, which include the difficulty of generating a controlled steady-state elongational flow field, combined with the coexistence of shear effects. The shear viscosity of a polymer melt can easily be measured using "cone and plate" viscometers for low to moderate shear rates, or by using capillary extrusion rheometers for moderate to high shear rates.

In extensional rheometry, there are two basic techniques for determining the elongational viscosity: tensile testing methods and converging flow methods. Each of these two methods carries advantages and limitations. The most widely used devices for the direct measurement of the elongational viscosity are the Meissner-type rheometers [21-23]. In these devices, the polymer sample is placed between two pulling devices in an oil or air bath in order to control the temperature, and then the constant elongational rate is achieved by deforming the sample with an exponentially increasing force. In this case, the advantages include the ability to generate shear-free uniaxial, biaxial and planar elongational flows. Some of the disadvantages include the fact that the sample needs to be very viscous or viscoelastic, typically close to the melting point. Therefore, these devices are limited in the temperature and strain rate ranges, which are usually much lower than the industrial processing conditions they are trying to imitate.

The second category of experimental techniques for determining the elongational viscosity is represented by the converging flow methods. See ref. [24] for a comprehensive review of these methods. Perhaps the most theoretically sound method for determining the elongational viscosity belongs to Collier and co-workers [24-27]. They introduced the use of the semi-hyperbolically converging die, which will be described in detail in §2.2.1. The semi-hyperbolically converging die retains some of the advantages of the Meissner-type devices, in the sense that it has been shown to generate essentially purely uniaxial elongational flow under full-slip at the wall boundary conditions [24, 26], while eliminating some of the disadvantages of the tensile devices. Using the Advanced Capillary Extrusion Rheometer (ACER 2000), and a Hencky strain of 7, elongational strain rates of up to 740 s^{-1} can be attained. The temperature is only bound at the high end of the range by the thermal degradation point of the polymer under investigation, while the lower bound of the temperature is determined by the range of the pressure transducer used. These experimental conditions are similar to what one would expect to find in an industrial processing operation, which makes the use of the semi-hyperbolically converging dies in extensional rheometry very attractive from a practical point of view.

2.2 Materials and Experimental Strategy

§2.2.1 *Geometrical Characteristics of a Semi-hyperbolically Converging Die*

The semi-hyperbolically converging dies (or in short, Hencky dies) are designed to generate purely uniaxial elongational flow, which is given by the unique geometry of the channel. Collier and co-workers provided evidence that the amount of shear experienced by the fluid at the wall is negligible [26]. By conducting "core-skin" experiments, in which the core consisted of a polymer melt, and the skin was a lubricant, followed by "skinless" experiments under the same conditions in which the lubricant was removed, they concluded that within statistical uncertainty, the viscosity measured using both techniques fell on top of each other. In other words, the amount of shear experienced by the "skinless" fluid sample at the wall was minimal, and the assumption of total slip at the wall was implied. Unless this assumption is made, the flow within the semi-hyperbolic channel is not purely extensional, but a combination of shear and elongational flow [24]. Later, using finite element modeling methods it was confirmed that the uniaxial elongational flow field was indeed generated within the die under full-slip boundary conditions [24]. Moreover, it was proven that the strain rate inside the die was independent of either axial or radial position. Kamerkar and Edwards examined experimentally the boundary condition by measuring the slip velocity in both straight-walled capillary tubes and Hencky dies, with and without the addition of a viscosity reducing additive (stearic acid) [28]. They found that the degree of slip was significantly greater for flow through the Hencky dies than through the capillary ones,

with or without the additive, under all experimental conditions. This implies that there is a high probability that the full-slip boundary conditions considered earlier [24, 26, 27] are actually achieved in practice.

The characteristics of the Hencky dies are given by their unique geometry,

$$r(z) = \sqrt{\frac{A}{z + B}} \tag{2.1}$$

where *r(z)* is the radius of the channel at axial position *z* from the entrance of the die. In equation 2.1, *A* and *B* are geometry-defined constants, and their mathematical expressions are

$$A = L\frac{R_0^2 R_e^2}{R_0^2 - R_e^2} \tag{2.2}$$

$$B = L\frac{R_e^2}{R_0^2 - R_e^2} \tag{2.3}$$

where *L* is the length of the die, R_0 and R_e are the entrance and exit radii respectively. The Hencky dies are also characterized by the Hencky strain number ε_H, which is the natural logarithm of the ratio of the entrance and exit areas:

$$\varepsilon_H = \ln\left(\frac{A_0}{A_e}\right) = \ln\left(\frac{D_0^2}{D_e^2}\right) \tag{2.4}$$

where D_0 and D_e are the entrance and exit diameters respectively. In Figure 2.1, an axial cross-section of the Hencky die is presented, with the Hencky strain $\varepsilon_H = 6$.

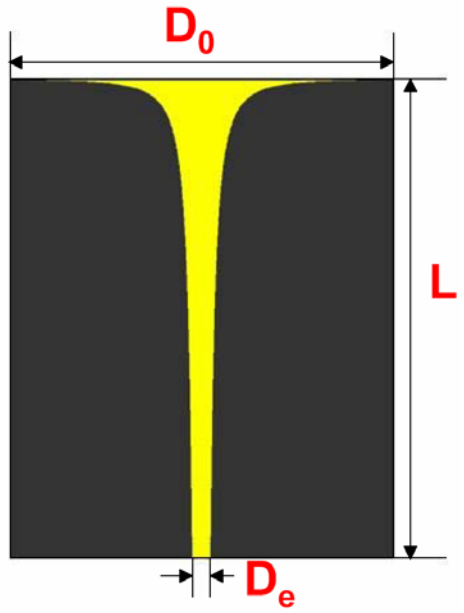

Figure 2.1: *Schematic representation of an axial cross-section of the Hencky 6 die.*

§2.2.2 *Materials*

In the present study, we decided on Polyethylene to be our polymer of choice, due to its importance in the polymer processing industry. We tested both a low density and a high density version, and their molecular characteristics are given in Table 2.1 below.

The thermal conductivity of polyethylene usually takes values in the interval $0.3<k<0.5$ W/m/K [29, 30]. Generally, the low density polyethylenes take values toward the lower limit of the interval, while high density polyethylenes take values toward the upper limit. For the two polymers considered in this study, exact measurements of the thermal conductivity have not been performed. The lower and upper limits of the interval have been considered for LDPE and HDPE respectively.

§2.2.3 *Advanced Capillary Extrusion Rheometer (ACER)*

So far, we have identified the possibility to generate a uniaxial elongational flow field under strictly controlled experimental conditions. This represents a major improvement over the original experiments reported in support of PEE [10, 11] in the

Table 2.1. *Molecular Characteristics of the Polymer Samples.*

Material	Grade	MI (g/10min)	Density (g/cm^3)	Thermal Conductivity ($Wm^{-1}K^{-1}$)	MW	PI
LDPE	Exact 3139	7.5	0.901	0.3	56,950	1.99
HDPE	Paxxon AB40003	0.3	0.943	0.5	105,200	9.74

sense that much higher levels of orientation can be achieved using the Hencky dies [28]. In this work, our goal is to perform similar tests as in the original experiments of Astarita *et al.* [10, 11], but for higher deformation rates, and also for higher temperatures.

Let us have another look at the temperature evolution equation for an incompressible fluid flow, which already contains the PEE assumption:

$$\rho \hat{c}_v \frac{DT}{Dt} = -(\nabla \cdot q) + (\tau : \nabla \mathbf{v}) \tag{2.5}$$

Our strategy is to solve this equation numerically for the temperature T using as few simplifying assumptions as possible. This will give us the expected temperature rise due to viscous heating for a spectrum of deformation rates. Note that the heat capacity here is a function of temperature only and not a function of conformation. Next, our plan is to measure experimentally the temperature rise due to viscous effects under the same flowing conditions and compare it to the predicted one from the numerical calculations. If the measured temperature rise is in agreement with the calculated one over the entire range of deformation rates, then the assumption of PEE will be verified.

The first step in our strategy is to evaluate the viscous dissipation term $(\tau : \nabla \mathbf{v})$ on the right side of equation 2.5. According to ref. [24], this term is given by:

$$\tau : \nabla \mathbf{v} = \frac{3}{2} \tau_{zz} \dot{\varepsilon} = \frac{\Delta P \dot{\varepsilon}}{\varepsilon_H} = \eta_{ef} \dot{\varepsilon}^2 \tag{2.6}$$

where τ_{zz} is the normal stress in the direction of the flow, $\dot{\varepsilon}$ is the elongation rate, ε_H is the Hencky strain, ΔP is the pressure difference between the entrance and the exit of the die, and η_{ef} is the effective elongational viscosity, as defined in ref. [24]. Therefore, in

order to evaluate the viscous dissipation term, it is necessary to measure the steady-state pressure drop, ΔP, as the elongation rate $\dot{\varepsilon}$ takes different values.

The elongational viscosity measurements are made using an Advanced Capillary Extrusion Rheometer (ACER 2000), in which the capillary die is replaced by a Hencky die. A schematic of the ACER 2000 apparatus is given below in Figure 2.2. It is worth pointing out that the schematic shown is not drawn to scale, and is made for illustrative purposes only.

In a typical viscosity measurement experiment, after the attachment of the die at the bottom, the barrel is first filled with polymer pellets and heated to the desired temperature. When the polymer is completely molten and the temperature inside the barrel wall has reached the prescribed value, the ram is attached. The drive mechanism will then push down the ram with precisely defined velocities, according to

$$v_{ram} = \frac{\dot{\varepsilon} L}{\exp(\varepsilon_H) - 1} \tag{2.7}$$

where $\dot{\varepsilon}$ is the elongation rate, L is the length of the die and ε_H is the Hencky strain.

This equation is programmed into ACER's software, and the parameters on the right side of equation 2.7 are specified by the user at the beginning of the experiment. For a particular elongation rate, the pressure drop along the die is measured using the pressure transducer and recorded as a function of time. The user has the option of deciding whether the steady state in terms of pressure drop has been attained, or the software can do it automatically according to a prescribed algorithm. The steady-state values of the pressure drop are then recorded and plotted as a function of strain rate.

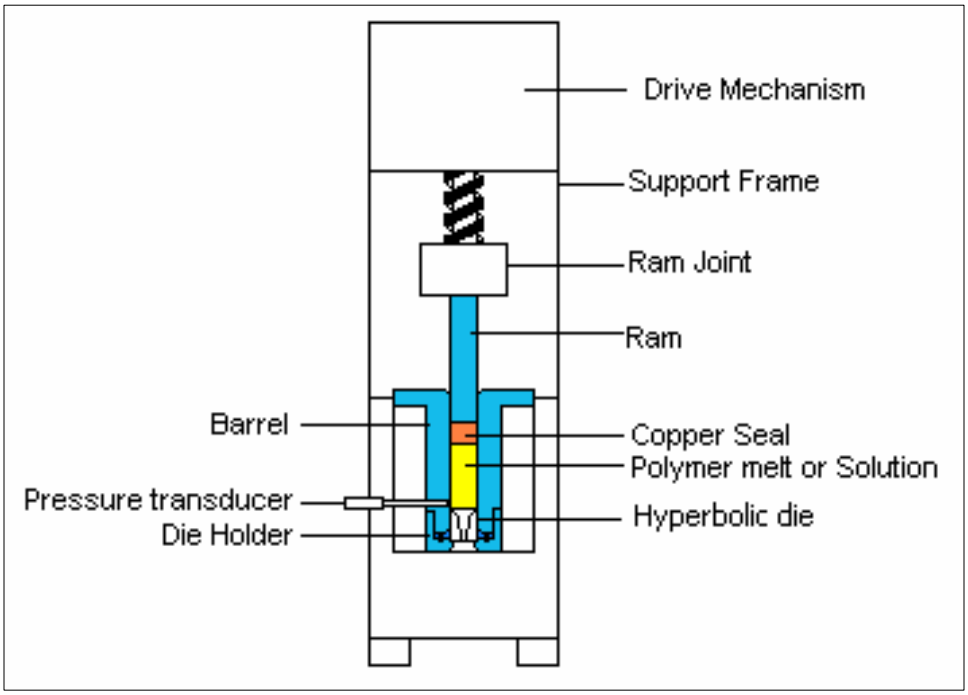

Figure 2.2: *Schematic representation of ACER 2000.*

The software can provide further manipulations of the data; for example, it can calculate the effective elongational viscosity according to equation 2.8 [24, 26],

$$\eta_{ef} = \frac{\Delta P}{\varepsilon_H \dot{\varepsilon}} \tag{2.8}$$

where $\Delta P = P_{in} - P_{exit}$ is the pressure drop along the die, P_{in} is measured by the pressure transducer and P_{exit} is the atmospheric pressure.

Following a similar procedure, the shear viscosity of a polymer melt can be measured using ACER by replacing the Hencky die with a capillary die. In this case, the ram is pushed down with prescribed velocities (v_{ram}) that are dependent on the shear rate values ($\dot{\gamma}$) defined by the user.

$$v_{ram} = \dot{\gamma} \frac{R_b^2}{4R_0^2} \tag{2.9}$$

where R_b is the radius of the barrel and R_0 is the radius of the capillary die. Solving the momentum equation 1.2 for the flow of an incompressible Newtonian fluid through a capillary tube, one gets the following for the shear stress at the wall [31]:

$$\tau_{rz}\big|_{wall} = \frac{\Delta P R_0}{2L} \tag{2.10}$$

where $\Delta P = P_{in} - P_{exit}$ is the pressure drop measured by ACER, and L is the length of the capillary tube. The shear viscosity at the wall for this case is:

$$\eta_{shear} = \frac{\Delta P R_0}{2L\dot{\gamma}} \tag{2.11}$$

§2.2.4 *Experimental Design for Temperature Measurements*

In section 2.4, the procedure for predicting the temperature profiles inside the die will be presented. In this procedure, the assumption that the elastic response of the polymer melt is purely entropic is embedded in the model equation (eq. 2.13). For a direct comparison, the temperature increase as a result of viscous heating effects is measured experimentally, under the same conditions simulated in the calculations. To this end, a thermocouple is placed at the bottom of the die, and the set of experiments described in §2.2.4 was redone for the same data points (in terms of inlet temperature, set flow rate and polymer used). In Figure 2.3, the schematic of the experimental design for measuring the temperature of the fluid coming out of the die is presented. Both dies (Hencky die and reverse conical converging die) were placed inside the barrel, therefore both dies were thermostated at T_{in}. The attachment of the reverse cone die was necessary to ensure proper measurement of the temperature of the fluid exiting the die. Preliminary attempts were made in which the reverse cone die was not used. At the highest flow rates, the velocity of the fluid coming out of the die reaches values up to 1.25 m/s. The presence of the thermocouple at the bottom made the fluid stream coming out of the die shoot randomly in all directions, never completely touching the tip of the thermocouple. We did try to explore another non-invasive procedure to measure T_{exit} using an infrared camera. The major inconvenience of this approach is the fact that the camera focuses on the surface of the fluid stream, thus recording the temperature at the surface. As we shall see in §2.4.1 later on, there are significant radial temperature gradients at the exit of the die. The infrared camera would

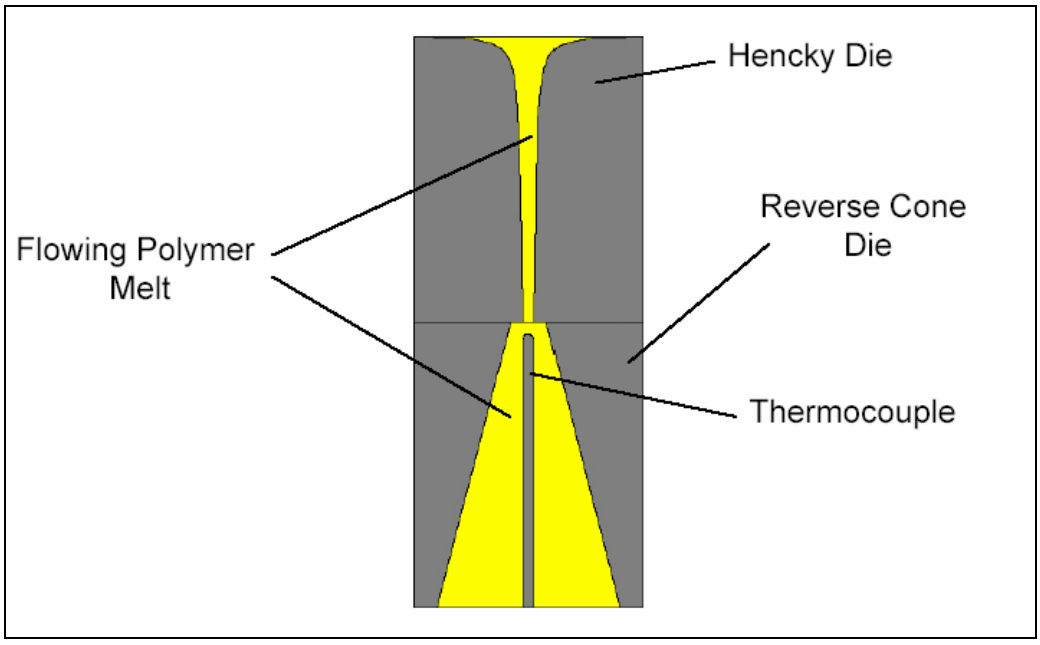

Figure 2.3: *Schematic of the experimental design for measuring the temperature of the fluid at the die exit.*

actually record the temperature at the die wall (same as T_{in}). Therefore, we decided that the design presented in Figure 2.3 yielded the best results, which were reproducible from run to run.

First, the temperature of the fluid at the die inlet (T_{in}) was monitored separately in a preliminary set of experiments by replacing the pressure transducer with a thermocouple of the same shape and size. This step was necessary in order to verify that there are no temperature gradients along the axis of the barrel, and also to check that the fluid temperature inside the barrel is at the prescribed value. Therefore, in our subsequent calculations, T_{in} was considered as the set temperature on ACER. The temperature probe used to measure the temperature of the fluid at the die exit (T_{exit}) was obtained from Omega Engineering Inc. using a J-type iron-constantan thermocouple, with part number JMQSS-032U-6. The temperature readings were made on a DP26-TC Differential Temperature Meter, also obtained from Omega Engineering Inc., with a precision of 0.1^{o}C. The temperature increase (ΔT) was recorded as a function of strain rate for various inlet temperatures for the two polymers mentioned in §2.2.2. The results will be presented in §2.4.2.

§2.2.5 *Advanced Rheometric Expansion System (ARES)*

In section 2.5, a theoretical procedure for generalizing the traditional temperature equation 1.12 using the UCMM will be presented. This procedure will require accurate knowledge of the characteristic relaxation times of the polymers under investigation. The characteristic relaxation time λ can be determined by measuring the

dynamic loss and storage moduli for the polymer melt. This can be achieved by performing a Dynamic Frequency Sweep (DFS) using the "cone-plate" geometry on an Advanced Rheometric Expansion System (ARES) rheometer.

In Figure 2.4, a simplified schematic of the experimental design on ARES is presented. The lower plate of the apparatus is connected to an electric motor, while the force and torque sensors are attached to the conic upper plate. The polymer sample is placed between the plates, which are surrounded by a gas convection chamber. The temperature is thus controlled by circulating pressurized gas (nitrogen or air) over two resistive heaters and through the chamber at a precise temperature. Furthermore, the temperature control loop of the system contains a temperature probe inserted into the lower plate for precise control of the temperature inside the sample. The polyethylene samples are prepared by compression molding at 160°C into flat sheets 1 mm thick. Circular discs 25 mm in diameter are then cut from the flat sheets after cooling to room temperature.

At low frequencies, when the loss modulus G'' is greater than the storage modulus G', the polymer melt is considered to behave as a viscous fluid, while at high frequencies, the storage modulus is greater, and the material is considered to develop elastic characteristics [27]. The frequency where the two moduli intersect is called the "crossover point", and its reciprocal ($1/\omega_{crossover}$) gives the characteristic relaxation time λ. The dynamic moduli, as well as the dynamic viscosity can be measured using the "cone-plate" viscometer (ARES), by applying shear step strains of prescribed frequencies ω in the interval $10^{-2} - 10^{2}$ s^{-1}.

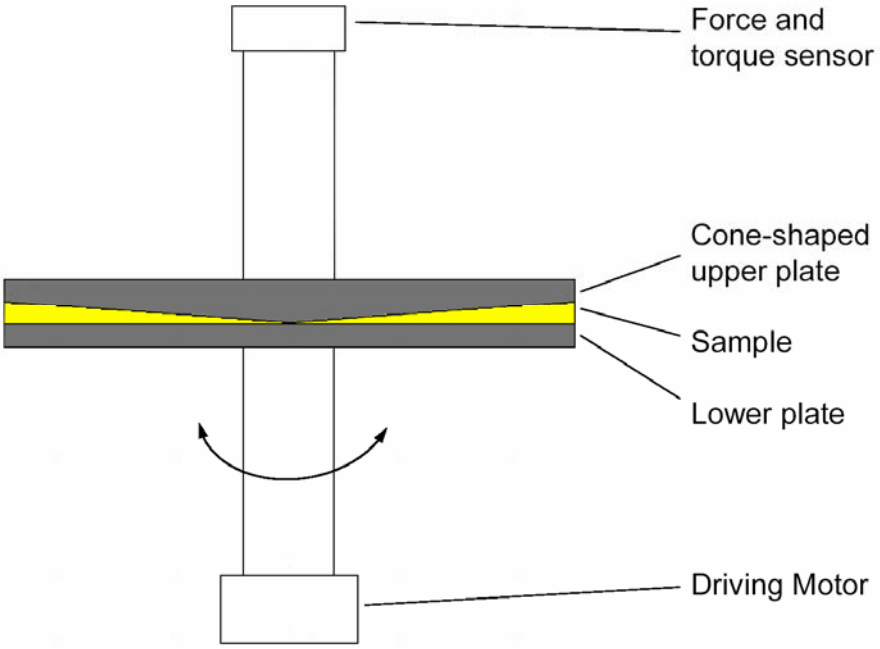

Figure 2.4: *Schematic representation of the "cone-plate" geometry on ARES.*

2.3 Elongational Viscosity Measurements for HDPE and LDPE

Let us first examine the elongational viscosity for the two polymers investigated. In Figures 2.5a) and 2.5b), the effective elongational viscosity (eq. 2.8) is plotted for HDPE (Fig. 2.5a) and LDPE (Fig. 2.5b) at strain rates in the interval $2 < \dot{\varepsilon} < 50\ s^{-1}$. The measurements were made at three temperature set points for each polymer. For LDPE, the measurements were performed at 150°C, 170°C and 190°C, while for HDPE the measurements were performed at 190°C, 210°C and 230°C. The upper limit of the temperature interval was dictated by the thermal stability of the polymers, and we observed changes in the color of the polymers from translucent to light brown when the temperature was increased further. Clearly, HDPE has a higher thermal stability than LDPE, as expected. The lower limit of the temperature interval was dictated by the physical limit of the pressure transducer. It is well known that the viscosity of a fluid is a strong function of temperature, and it increases as the temperature is decreased. Consequently, the pressure drop recorded by the pressure transducer will increase as the temperature is lowered for a particular flow rate, which in turn puts limitations on the upper boundary of the strain rate spectrum that can be investigated. We observed that the safety limit of the pressure transducer (56 MPa) was approached at the highest flow rates as the temperature was lowered below the abovementioned limits.

The purpose of measuring the elongational viscosity at different temperatures is two-fold. First, it will allow us to test the PEE assumption at more than one temperature. Second, the viscosity data at a given elongation rate can be fitted to an

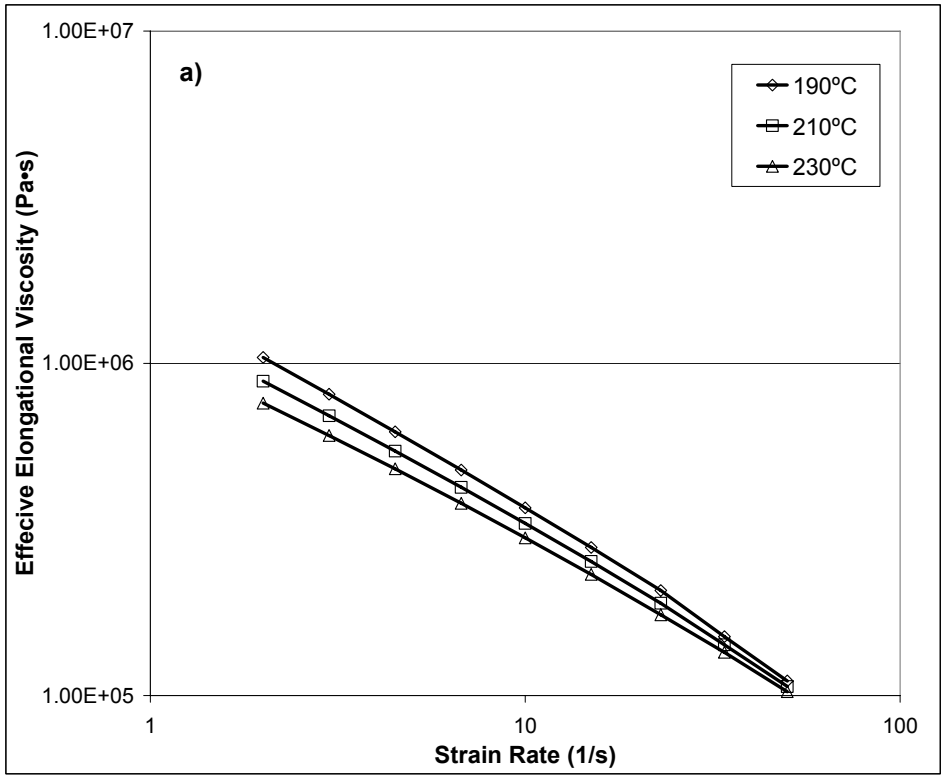

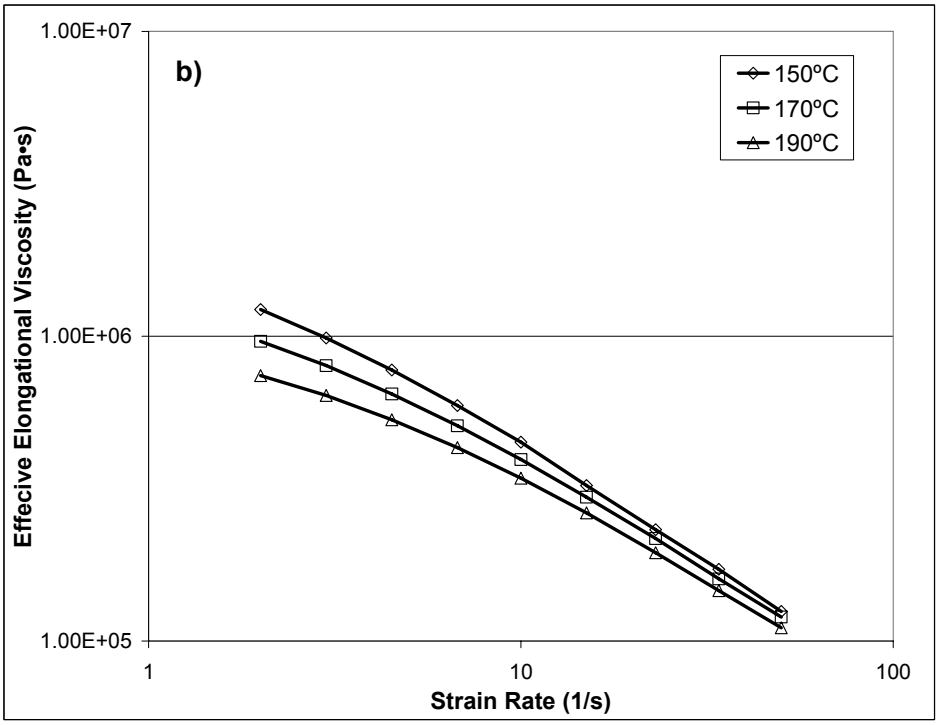

Figure 2.5: *Effective elongational viscosity for a) HDPE and b) LDPE.*

Arrhenius type expression [1],

$$\eta(T) = \eta_0 \exp\left(\frac{A_0}{k_B T}\right) \tag{2.12}$$

where η_0 is the "infinite temperature" viscosity, and A_0 is an activation energy. The fitting parameters η_0 and A_0 for a given strain rate are then input into the finite element code and will account for the temperature dependence of the viscosity in §2.4.1. In Table 2.2, the fitting parameters are given for both polymers investigated.

2.4 Finite Element Modeling

The viscous heating term (eq. 2.6) can be determined from the experimental measurements described in §2.2.3, and the next step in our analysis is to compute the

Table 2.2. *Arrhenius Fitting Parameters for the Viscosity of HDPE and LDPE.*

	HDPE		LDPE	
$\dot{\varepsilon}$ (1/s)	η_0 (Pa·s)	A_0/k_B (K)	η_0 (Pa·s)	A_0/k_B (K)
2	20315.723	1834.177	4141.544	2420.944
3	23065.660	1656.095	6997.973	2106.395
4.5	25873.061	1481.147	10712.899	1821.999
6.75	27098.328	1336.516	15810.890	1542.317
10	27646.919	1205.008	20286.351	1318.180
15	27491.897	1079.504	30646.385	1005.090
23	25539.599	974.864	32226.460	842.302
34	39019.108	628.583	27349.012	783.112
50	43942.717	430.121	31115.282	594.244

radial and axial temperature profiles inside the die channel as a result of the frictional heating effects. This will be accomplished by solving equation 2.5 at steady state using as few limiting assumptions as possible.

For this system, the steady-state temperature distribution equation can be written as

$$\rho\hat{c}_v\left(\mathbf{v}\cdot\nabla T\right)=k\nabla^2 T+\left(\tau:\nabla\mathbf{v}\right) \tag{2.13}$$

where k is the thermal conductivity of the polymer melt. Given the complex nature of this partial differential equation, unless highly restrictive limiting assumptions are made, it is not possible to solve it analytically. We did succeed to find an analytical solution (eq. 2.14) to this equation by assuming an adiabatic system (by effectively zeroing the conduction term $k\nabla^2 T$) and by considering the temperature gradient having a non-zero component in the axial direction only.

$$\Delta T = T_{exit} - T_{in} = \frac{\Delta P}{\rho\hat{c}_v} \tag{2.14}$$

where ΔP is the pressure drop along the die, ρ is the fluid density and c_v is the constant volume heat capacity. However, we found that this level of approximation produced a severe over-prediction of the actual temperature increase along the die channel and proceeded to find a numerical solution to this equation without the abovementioned simplifications using a finite element technique. At this point, it is worth emphasizing that equation 2.13 has the assumption of PEE embedded in it, in the sense it does not contain the term dependent on the internal structure of the fluid (see eq. 1.17).

We used FEMLAB® [32] to find numerical solutions to equation 2.13 for various inlet temperatures, elongation rates and the polymers given in Table 2.1. We built our model based on the "Steady-State Convection and Conduction" model in the Chemical Engineering module, using the 2D axially symmetric space dimension. We incorporated temperature functionalities into the heat capacity from ref. [33] for generic polyethylene, and into the elongational viscosity from our own experimental measurements. The velocity field is user pre-defined, and constitutes an input variable which will define the convection term on the right side of equation 2.13. The velocity field profile used in this study was previously calculated as [24]

$$v_r = -\frac{1}{2}\dot{\varepsilon} r \tag{2.15}$$

$$v_z = \dot{\varepsilon} z \tag{2.16}$$

As detailed in ref. [24], this velocity profile corresponds to a purely uniaxial elongational field. In the present study, we did verify that the velocity profile is that described by equations 2.15 and 2.16 by solving the momentum equation 1.2 independently in a separate set of FEM calculations, using the same full-slip boundary conditions. In the FEM analysis, equation 2.13 was solved numerically using the following set of boundary conditions:

1. At the die entrance, $T(r, z = 0) = T_{in} = T_{set}$; (2.17)

2. At the wall, $T\left(r = \sqrt{\frac{A}{z + B}}, z\right) = T_{set}$. (2.18)

§2.4.1 *FEM Temperature Profile Predictions*

The FEM calculations gave us the radial and axial temperature profiles inside the die channel, which allowed us to compute average temperature values for the exit cross-section of the die. The Hencky strain number for the die used in our calculations is 6 (see eq. 2.4), the same as in the experimental part. The FEM calculations enabled us to predict an effective temperature increase (eq. 2.19) due to viscous heating along the die axis:

$$\Delta T = \langle T \rangle_{exit} - T_{in} \tag{2.19}$$

$$\langle T \rangle_{exit} = \frac{\int_0^R T(r, z = L) r \mathrm{d}r}{\int_0^R r \mathrm{d}r} \tag{2.20}$$

where T_{in} is the inlet temperature, R is the radius of the die channel at the die exit, r is the radial position, z is the axial position and L is the die length.

In Figure 2.6, the axial temperature profile at r = 0 (Fig. 2.6a) and the radial temperature profile at z = 25mm (Fig. 2.6b) are given for the HDPE melt at the inlet temperature of 190°C in terms of the net increase $\Delta T = \langle T \rangle_{exit} - T_{in}$ at all elongation rates. For all cases considered, these profiles are qualitatively similar. In the axial temperature profiles there is a maximum occurring close to the entrance at the lowest flow rates, due to two competing phenomena taking place. First, heat is generated due to friction within the body of the fluid. The stresses and the velocity gradients giving rise to the heat generation term are constants with respect to axial and radial positions

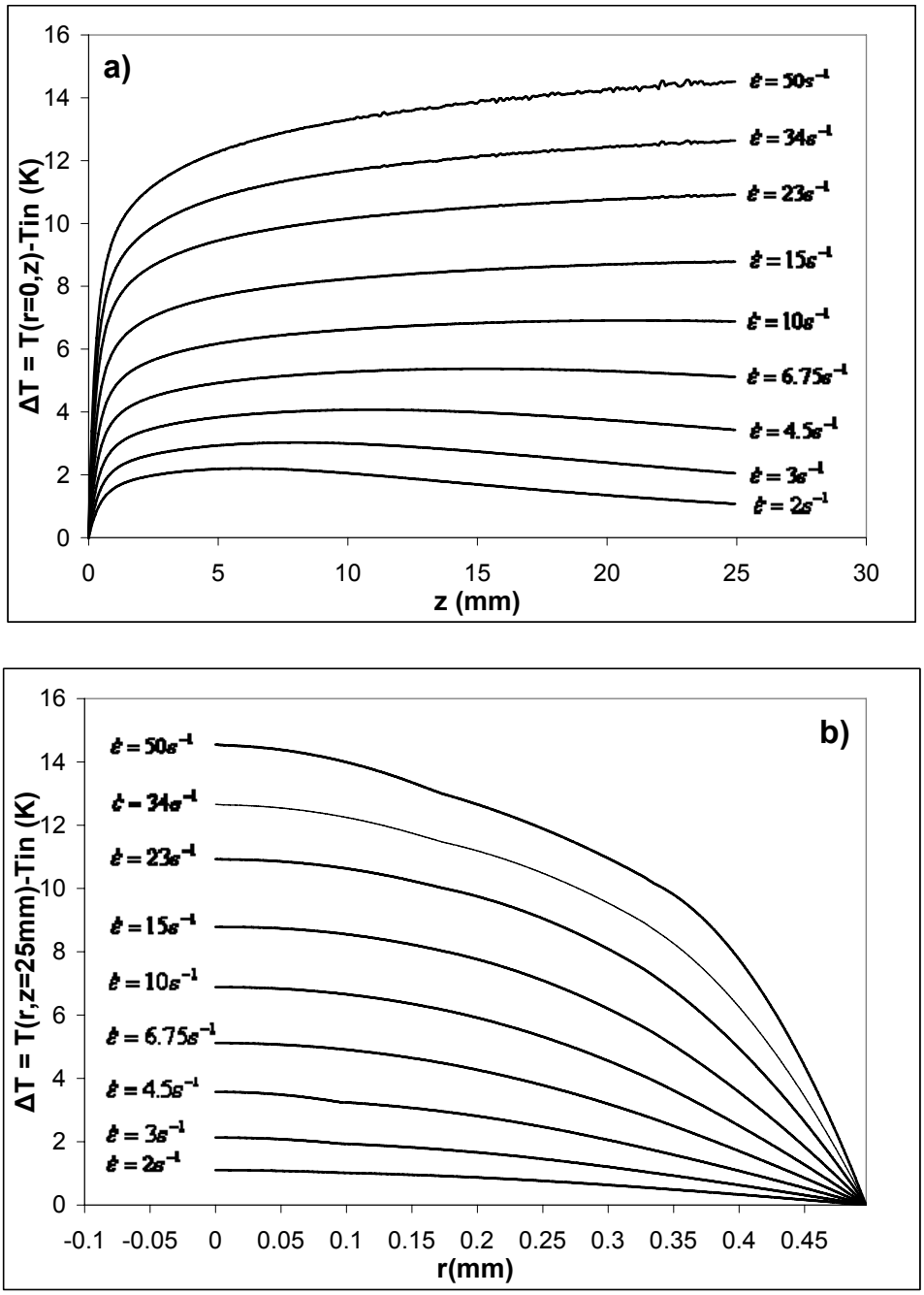

Figure 2.6: *a) Axial and b) radial calculated temperature profiles for HDPE at* T_{in} *= 190°C.*

for a particular flow rate [24], which in turn will make the heat generation term a constant throughout the entire spatial domain. Second, heat is removed by conduction through the die wall. This term is not a constant with either the radial or the axial position. As the radius of the channel gets smaller, the heat loss through the die wall increases. The heat conduction term is compensating the generation term, thus reducing the temperature. However, as the flow rate is increased, the maximum in the axial temperature profile will be pushed towards the exit. While the heat conduction term is increasing slowly with strain rate (due to sharper temperature gradients), the heat generation term is increasing much faster with strain rate and eventually it will overcome the heat loss through the die wall throughout the entire spatial domain.

At the die exit, an average value for the temperature can be calculated by numerical integration using equation 2.20. Typically, the average temperature for a cross-section (or the "bulk temperature" [31]) is also weighted by the axial velocity v_z. In this case, v_z is independent of the radial position r and it will drop out of the equation:

$$\langle T \rangle_{exit} = \frac{\int_0^R T(r, z=L) v_z(r) r \mathrm{d}r}{\int_0^R v_z(r) r \mathrm{d}r} = \frac{v_z \int_0^R T(r, z=L) r \mathrm{d}r}{v_z \int_0^R r \mathrm{d}r} = \frac{\int_0^R T(r, z=L) r \mathrm{d}r}{\int_0^R r \mathrm{d}r} \qquad (2.21)$$

In Figure 2.7, the average temperatures at the exit cross-section of the die resulting from the FEM calculations are presented for HDPE (Fig. 2.7a) and LDPE (Fig. 2.7b). For consistency, the temperatures are given in terms of the net change with respect to the inlet temperature. The FEM calculation results are not surprising. We observe a steady temperature increase as the strain rate is increased for both HDPE and LDPE. This can easily be explained if we take another look at the heat generation term.

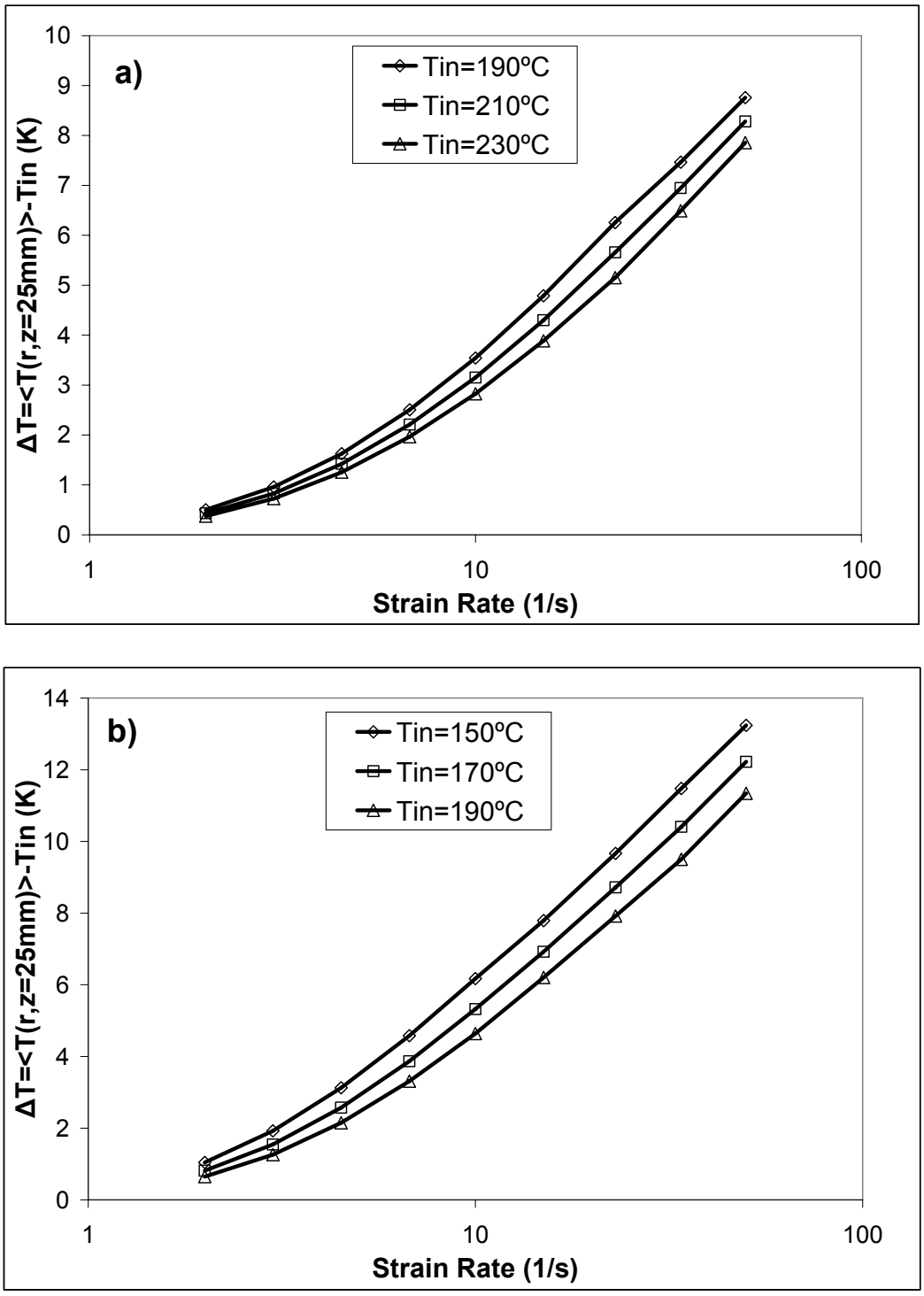

Figure 2.7: *Calculated average temperature changes at the die exit for a) HDPE and b) LDPE.*

$$\tau : \nabla \mathbf{v} = \eta_{ef} \dot{\varepsilon}^2 \tag{2.22}$$

Even though the viscosity is decreasing as the strain rate increases, the heat generation term is directly proportional to the second power of the strain rate. Overall, the heat generation term will increase almost linearly with strain rate. Moreover, for a given flow rate, the temperature change will increase as the inlet temperature is decreased. Again, this is a consequence of the generation term, because the viscosity increases as the temperature is decreased. It is worth pointing out that at the same inlet temperature (190°C), the temperature increase is larger for LDPE than it is for HDPE. This is somewhat counterintuitive, given the fact that the viscosity of HDPE is greater than that of LDPE at the same temperature (see Fig. 2.5). Nevertheless, this behavior is easily explained if we take the thermal conductivity into consideration. In Table 2.1 the thermal conductivity values for typical HDPE and LDPE are given. In our FEM calculations we observed that the temperature profiles are sensitive to the thermal conductivity, and the lower value for LDPE fully accounts for the abovementioned behavior.

§2.4.2 *Experimental Temperature Measurements*

With the temperature profile calculations completed, we proceeded to measure the temperature change under the same conditions using the experimental design described in §2.2.4. In Figure 2.8, the complete results for HDPE are given.

For the experimental measurements, we observe the same qualitative behavior predicted by the FEM calculations. We observe an excellent agreement between the

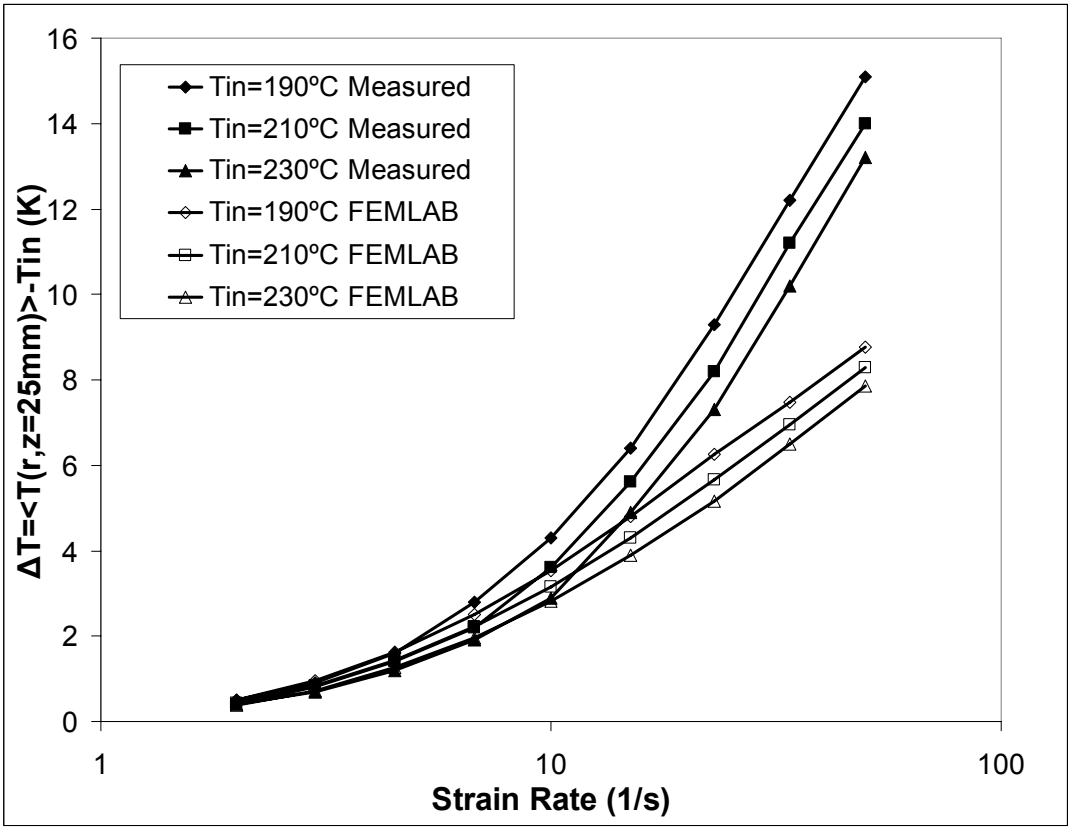

Figure 2.8: *Temperature changes for HDPE: filled symbols represent the measured values; open symbols represent the FEM calculated values.*

simulated and measured values for the temperature changes at low to moderate elongation rates, as is clearly shown in Figure 2.8. However, at high elongation rates, we notice a systematic deviation from the calculated values. Moreover, as the inlet temperature is decreased, the deviation starts to occur at lower flow rates.

In Figure 2.9, we compare the behavior of HDPE and LDPE under the same conditions (T_{in} = 190°C). We notice that the agreement between measured and predicted temperature changes for LDPE is maintained for a wider range of elongation rates. As we shall see later on, this is due to differences in the relaxation times between the two polymers. Clearly, both polymers investigated show deviations from the predicted temperature profiles to various degrees. This is clear evidence that equation 2.13 is not obeyed for the entire range of elongation rates employed in this study. From this point on, we will try to find possible explanations as to why deviations from equation 2.13 are observed.

2.5 Theoretical Analysis for Improving the Temperature Equation

Let us examine the temperature distribution equation 2.13, and also the assumptions that were made in deriving and solving it. The analysis started with the energy balance equation 1.4.

$$\rho \frac{D\hat{U}}{Dt} = -(\nabla \cdot \mathbf{q}) - p(\nabla \cdot \mathbf{v}) + (\tau : \nabla \mathbf{v}) \tag{2.23}$$

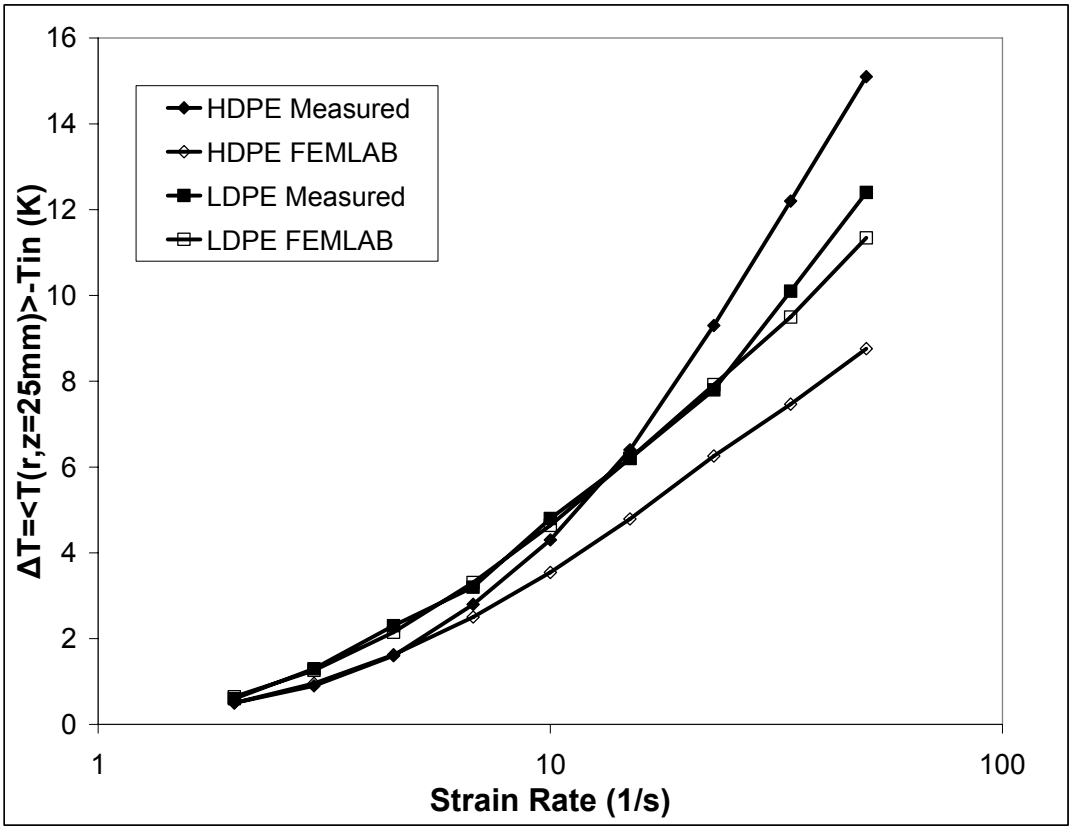

Figure 2.9: *Measured (filled symbols) and calculated (open symbols) temperature changes for HDPE (diamonds) and LDPE (squares) at* T_{in} *= 190°C.*

Then, the following assumptions were made:

1. The fluid is incompressible ($\nabla \cdot \mathbf{v} = 0$) (2.24)

2. The flow is steady ($\frac{\partial \hat{U}}{\partial t} = 0$) and ($\frac{D\hat{U}}{Dt} = \mathbf{v} \cdot \nabla \hat{U}$) (2.25)

3. The fluid is purely entropic ($U = U(T)$) and ($c_v = \frac{\mathrm{d}U(T)}{\mathrm{d}T}$) (2.26)

4. Full-slip boundary conditions at the die wall.

Certainly, one would expect assumption 1 to be true for a wide range of pressures when it comes to liquids. In our experiments, we encountered pressures of up to 50 MPa, which is not enough to observe density changes through compression. The second assumption is also reasonable in this case. We have allowed sufficient time in our measurements for both the pressure and the temperature to reach steady-state values. As a direct consequence of the third assumption, the constant volume heat capacity is a constant with respect to elongation rate (i.e. the degree of orientation developed in the melts) and there is no conformation dependent extra term (see equation 1.17). At this point, we will retain assumption 3 and will call it into question later on.

Applying the first three assumptions above, the energy balance equation 2.23 becomes the steady-state temperature distribution equation 2.27,

$$\rho \hat{c}_v (\mathbf{v} \cdot \nabla T) = -(\nabla \cdot \mathbf{q}) + (\tau : \nabla \mathbf{v}) \tag{2.27}$$

where **q** is the heat flux vector. Including assumption 4, the heat generation term is given by equation 2.28 [24]

$$\tau : \nabla \mathbf{v} = \eta_{ef} \dot{\varepsilon}^2 \tag{2.28}$$

By applying the three dimensional Fourier's law (eq. 2.29) [31] and considering the fluid isotropic in the sense that heat is conducted in all directions with the same thermal conductivity, we get the final form of the temperature distribution equation used in our FEM calculations 2.30,

$$\mathbf{q} = -k\nabla T \tag{2.29}$$

$$\rho\hat{c}_v\left(\mathbf{v}\cdot\nabla T\right) = k\nabla^2 T + \eta_{ef}\dot{\varepsilon}^2 \tag{2.30}$$

§2.5.1 *Effect of the Boundary Conditions*

In ref. [24] it has been shown that the effective elongational viscosity η_{ef} measured using the semi-hyperbolically converging die technique is an accurate approximation of the true elongational viscosity under full-slip boundary conditions (assumption 4). In this study we tested the effect of assumption 4 on the temperature profiles by performing a set of FEM calculations in which the momentum and heat equations were solved simultaneously as a coupled system of partial differential equations. The full-slip boundary conditions were replaced by no-slip boundary conditions, and the resulting velocity profiles were used to define the convection term on the left side of equation 2.30. In this case, the radial and axial components of the velocity field will differ significantly from equations 2.15 and 2.16 respectively, as shown in ref. [24]. In figure 2.10, the axial temperature profiles obtained using the full-slip and no-slip boundary conditions are presented for the HDPE melt at T_{in} = 190°C

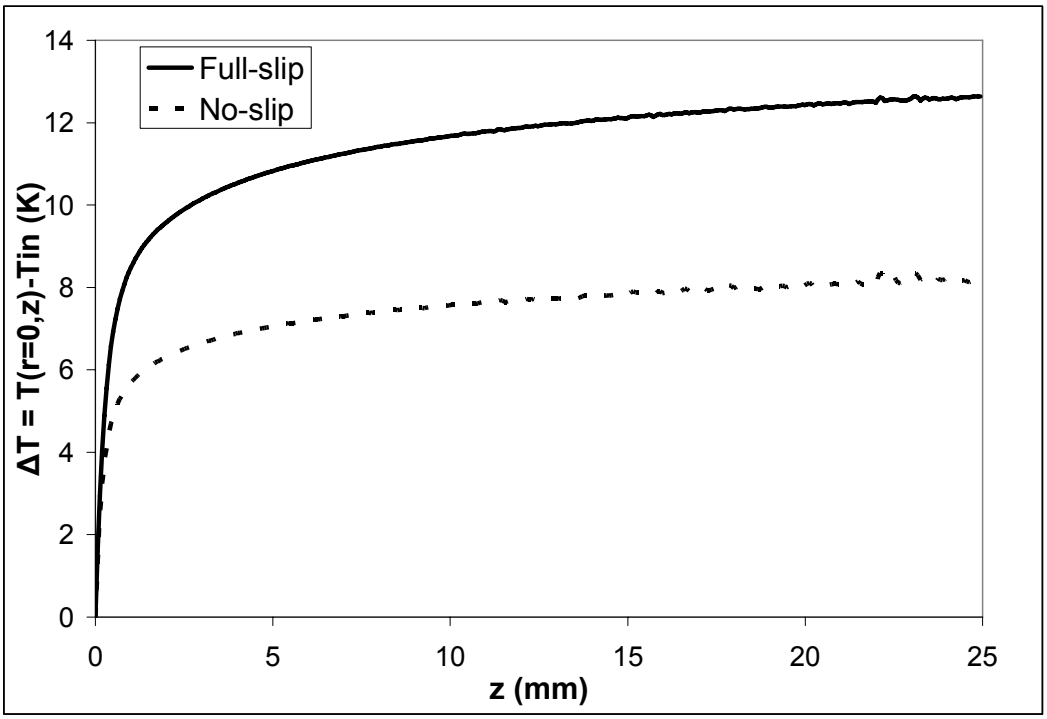

Figure 2.10: *Effect of the applied boundary conditions on the calculated axial temperature profiles for the HDPE melt at* T_{in} *= 190°C and* $\dot{\varepsilon} = 34 s^{-1}$.

and $\dot{\varepsilon} = 34 s^{-1}$. It is clear from figure 2.10 that changing the boundary conditions has a significant effect on the temperature profile, mainly because the convection term was altered. However, introducing no-slip at the wall seems to lower the temperature profile. Therefore, we conclude that the boundary conditions used in this study (assumption 4) cannot be responsible for the deviations observed in figures 2.8 and 2.9, given the opposite behavior observed.

In equation 2.30, we are left with two possible causes that may be responsible for the deviations observed in Figures 2.8 and 2.9. First, the thermal conductivity, *k* may not be a constant with the degree of orientation; second, the third assumption made above (eq. 2.26) may not be valid. In §2.5.2, the thermal conductivity effect on the solution of equation 2.30 will be investigated. In §2.5.6, the PEE assumption (eq. 2.26) will be removed and the relative importance of the two consequences of equation 2.26 will be discussed in detail.

§2.5.2 *Effect of the Thermal Conductivity*

Let us focus our attention now on the thermal conductivity *k*. While the thermal conductivity of polymeric materials at equilibrium is isotropic (i.e., has the same value in all directions), it is generally accepted that for deformed polymers, the thermal conductivity becomes anisotropic [29, 34-43]. This phenomenon can be explained if we examine the way thermal energy is conducted in oriented polymeric materials. In a polymeric material subjected to deformation, the chains become stretched out and partially aligned with each other. Kinetic theory suggests that the propagation of the

thermal vibrations is accomplished more efficiently along the backbone of the chain, because it consists of strong covalent bonds. The van der Waals interactions established between side chains are weaker and longer ranged, which will make it more difficult for the thermal vibrations to propagate in a direction perpendicular to the polymer chains.

Experimentally, it has been shown that the thermal conductivity in the direction parallel to the direction of deformation ($k_{\|}$) increases with degree of orientation, while the thermal conductivity perpendicular to the direction of deformation ($k_{\perp}$) decreases. This phenomenon is highly sensitive to temperature and to the physical state of the polymer. For example, it has been measured that when solid high-density polyethylene is subjected to uniaxial extension at room temperature with draw ratios λ between 1 and 25, $k_{\perp}$ suffers a reduction of up to 50% with respect to the isotropic value accompanied by a simultaneous increase in $k_{\|}$ of up to 2000%, approaching the value for stainless steel [29]. In polymer melts subjected to shear or extensional flows, the extent to which the two components of the anisotropic thermal conductivity tensor change is much lower. Notable is the work of Venerus and co-workers, in which they developed a non-invasive method for measuring the anisotropic thermal conductivity in polymer melts under static or dynamic conditions through Forced Rayleigh Light Scattering (FRLS) [37, 39-42, 44]. Decreases in $k_{\perp}$ of up to 10% and increases in $k_{\|}$ of up to 20% were observed during shear [37, 39, 40, 42, 44] and extensional [40] flows. In an effort to relate the anisotropic thermal conductivity tensor to the extra stress tensor, van den

Brule suggested a linear relation between the two tensors using a simple network model for polymer liquids [45]:

$$\mathbf{k} - \frac{1}{3}\mathrm{tr}(\mathbf{k})\delta = k_{iso} C_t \tau \tag{2.31}$$

where k_{iso} is the isotropic thermal conductivity and C_t is the so called "stress-thermal coefficient". Equation 2.31 is the formulation of the "stress-thermal law", which is analogous to the stress-optical law relating the refractive index tensor to the extra stress tensor. Subsequent research has found the stress-thermal law to be valid for a wide range of polymers and deformations [35, 39, 40, 42, 44].

With that in mind, we proceeded to test the effect of changing the thermal conductivity in our FEM calculations. Following the recipe reported in literature, we have set $k_{\perp} = 0.9 \cdot k_{iso}$ and $k_{\parallel} = 1.2 \cdot k_{iso}$ for HDPE at $T_{in} = 190^{\circ}\mathrm{C}$, at a strain rate where deviation from the calculated temperature profile was observed ($\dot{\varepsilon} = 34 s^{-1}$). It is important to point out though that we can only make qualitative assessments at this point, given that the stress-thermal coefficient for HDPE under uniaxial elongational flow has not yet been reported. We have purposely chosen the most extreme situation reported in literature (10% decrease in $k_{\perp}$ and 20% increase in $k_{\parallel}$) in order to prove our point. As detailed in [24], the extra stress tensor is constant throughout the entire spatial domain; therefore the stress-thermal law may prove to be valid in this case as well. However, it has been inferred that the level of orientation achieved within the Hencky dies increases steadily with axial position *z* [24, 28]. If we assume that the anisotropic thermal conductivity is related to the internal degree of orientation, then a more refined

expression for the thermal conductivity as a function of axial position could be introduced. Therefore, we would not expect a quantity that is dependent on the degree of orientation to reach a plateau value either. As we shall see later on, an exact expression to relate the thermal conductivity tensor to the axial position is not needed, and useful conclusions can be inferred from the general trends observed.

In our FEM analysis, we have the ability to specify an anisotropic form for the thermal conductivity. In this specific case, when cylindrical coordinates have been used, the anisotropic thermal conductivity is defined by two values: the perpendicular component (k_{rr}) and the parallel component (k_{zz}).

In Figure 2.11 we show the axial temperature profiles in terms of the temperature change with respect to the inlet temperature for the two cases when the isotropic thermal conductivity (k_isotropic) and the anisotropic thermal conductivity (k_anisotropic) were considered for the HDPE melt. The system conditions are T = 190°C and $\dot{\varepsilon} = 34 s^{-1}$. We observed that even in the most extreme case considered, changing the thermal conductivity from isotropic to anisotropic has a minimal impact on the calculated temperature profiles. The profiles in Figure 2.11 were calculated using constant values for k_{rr} and k_{zz} with respect to axial position. As detailed above, we would expect those values to change gradually from k_{iso} at the die entrance to a specific value towards the exit, which will make the difference shown in Figure 2.11 even less pronounced.

It is clear from Figure 2.11 that the thermal conductivity cannot be responsible for the deviations shown in Figures 2.8 and 2.9. Moreover, it is shown that even if the

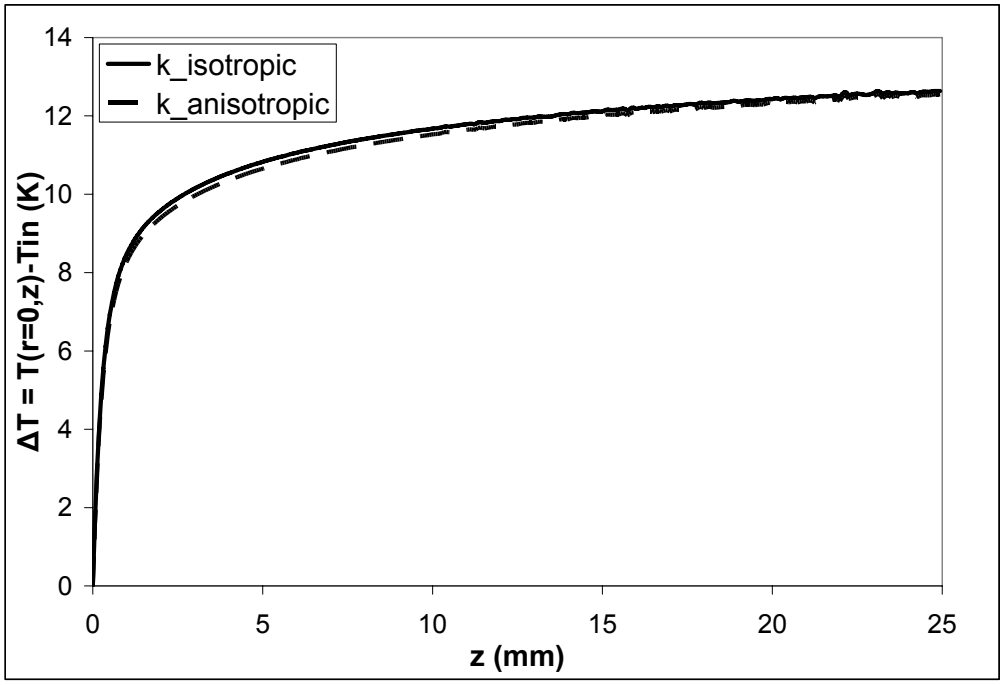

Figure 2.11: *Effect of anisotropy in thermal conductivity on the axial temperature profile.*

anisotropy in *k* does have an impact in our measurements, it is going to be minimal and in the *opposite direction* (i.e., it tends to decrease the temperature profile, rather than increase it in order to approach the experimentally measured temperature profile).

This conclusion is very important in our analysis, because by process of elimination, the only remaining cause for the deviations shown in Figures 2.8 and 2.9 is the third assumption (eq. 2.26) made to derive equation 2.30. Eliminating this assumption has two consequences: first, the heat capacity can no longer be independent of the degree of orientation; second, the extra term on the right side of equation 1.17 is potentially important, and can no longer be neglected. This result disproves the validity of PEE under the high strain-rate experimental conditions employed in this study.

§2.5.3 *The Conformation Tensor Evolution Equations*

Using the UCMM, Beris and Edwards wrote down the time and space evolution equations for the conformation tensor [20]:

$$\overset{\nabla}{c}_{\alpha\beta} = -\frac{1}{\lambda} c_{\alpha\beta} + \frac{k_B T}{\lambda K(T)} \delta_{\alpha\beta} \tag{2.32}$$

where $\overset{\nabla}{c}_{\alpha\beta}$ is the upper-convected time derivative of the $\alpha\beta$ component of the conformation tensor (eq. 1.13), λ is the relaxation time, *K(T)* is the chain spring constant and $\delta_{\alpha\beta}$ is the Kronecker delta. The upper-convected time derivative is defined as

$$\overset{\nabla}{c}_{\alpha\beta} = \frac{\partial c_{\alpha\beta}}{\partial t} + v_\gamma \nabla_\gamma c_{\alpha\beta} - c_{\alpha\beta} \nabla_\gamma v_\beta - c_{\alpha\beta} \nabla_\gamma v_\alpha \tag{2.33}$$

In Cartesian coordinates, the velocity gradient field developed in the Hencky die corresponding to a uniaxial extension is written as:

$$\nabla v = \begin{pmatrix} -\dot{\varepsilon}/2 & 0 & 0 \\ 0 & -\dot{\varepsilon}/2 & 0 \\ 0 & 0 & \dot{\varepsilon} \end{pmatrix} \tag{2.34}$$

where $\dot{\varepsilon}$ is the elongation rate. In this case, the fluid is extended in the z direction, while it is being contracted in the x and y directions. Consequently, equation 2.33 can be rewritten for the diagonal components of the conformation tensor as:

$$\breve{c}_{xx} = \frac{\partial c_{xx}}{\partial t} + \dot{\varepsilon} c_{xx} \tag{2.35}$$

$$\breve{c}_{yy} = \frac{\partial c_{yy}}{\partial t} + \dot{\varepsilon} c_{yy} \tag{2.36}$$

$$\breve{c}_{zz} = \frac{\partial c_{zz}}{\partial t} - 2\dot{\varepsilon} c_{zz} \tag{2.37}$$

Obviously, the off-diagonal components of the conformation tensor are zero. If we rewrite equation 2.32 in terms of the normalized conformation tensor, and combine it with equations 2.35 through 2.37, we get the following system of partial differential equations for the diagonal components of the normalized conformation tensor:

$$\frac{\partial \tilde{c}_{xx}}{\partial t} = c_{xx}\left(-\dot{\varepsilon} - \frac{1}{\lambda}\right) + \frac{1}{\lambda} \tag{2.38}$$

$$\frac{\partial \tilde{c}_{yy}}{\partial t} = c_{yy}\left(-\dot{\varepsilon} - \frac{1}{\lambda}\right) + \frac{1}{\lambda} \tag{2.39}$$

$$\frac{\partial \tilde{c}_{zz}}{\partial t} = c_{zz}\left(2\dot{\varepsilon} - \frac{1}{\lambda}\right) + \frac{1}{\lambda} \tag{2.40}$$

Integrating, and using equation 2.4 for the definition of the Hencky strain number ε_H, the following analytical solution is found to this system of equations (eqns. 2.38 through 2.40):

$$\widetilde{c}_{xx} = \widetilde{c}_{yy} = \frac{\lambda\dot{\varepsilon}}{\lambda\dot{\varepsilon}+1}\left[\left(\frac{z}{L}\right)^{-\left(1+\frac{1}{\lambda\dot{\varepsilon}}\right)} \cdot \exp\left[-\left(\frac{t_R}{\lambda}+\varepsilon_H\right)\right]\right] + \frac{1}{1+\lambda\dot{\varepsilon}} \tag{2.41}$$

$$\widetilde{c}_{zz} = \frac{2\lambda\dot{\varepsilon}}{2\lambda\dot{\varepsilon}+1}\left[\left(\frac{z}{L}\right)^{\left(2-\frac{1}{\lambda\dot{\varepsilon}}\right)} \cdot \exp\left[-\left(\frac{t_R}{\lambda}-2\varepsilon_H\right)\right]\right] - \frac{1}{2\lambda\dot{\varepsilon}-1} \tag{2.42}$$

where z is the axial position inside the die channel, L is the centerline length of the die channel and t_R is the residence time of a fluid particle in the die [24].

Using the single-mode Giesekus model, Beris and Edwards wrote down the conformation tensor evolution equations as [20]:

$$\breve{c}_{\alpha\beta} = -\frac{1}{\lambda}\left((1-\beta)\delta_{\alpha\gamma} + \beta\widetilde{c}_{\alpha\gamma}\right)\left(\widetilde{c}_{\gamma\beta} - \delta_{\gamma\beta}\right) \tag{2.43}$$

where β is an empirical constant between 0 and 1 ($0 \leq \beta \leq 1$). Clearly, when $\beta = 0$, the UCMM is recovered (equation 2.32). For $\beta > 0$, equation 2.43 is quadratic in terms of the conformation tensor components, which makes it more difficult to be solved analytically. However, equation 2.43 can easily be solved numerically using a fourth order Runge-Kutta method. The parameter β is not known *a priori*, and is typically determined by fitting experimental data. In this study, the single-mode Giesekus model will be used to refine the UCMM predictions.

§2.5.4 *Relaxation Time Measurements*

Up to this point, we have everything we need in order to evaluate the normalized conformation tensor components as a function of axial position and strain rate, except for the relaxation time λ. The relaxation times were measured following the procedure described in §2.2.5. In Figure 2.12 we present a typical result for the evaluation of the relaxation time. The material used was HDPE, at 190°C.

In the case of the LDPE melt, the relaxation time is smaller than the reciprocal of the highest frequency that can be attained on ARES (10^2 s^{-1}) in the entire range of temperatures considered (120°C – 170°C). Below 120°C the LDPE samples were no longer in the molten state, making it impossible for the prescribed gap between the upper and lower plated to be achieved. Even for this case, when the relaxation time was too low for the apparatus to capture it, relatively accurate estimates can be made from the measured data. In this case it is useful to examine the ratio of the two dynamic moduli and make a prediction beyond the range of the apparatus as to what would be the frequency where the ratio would reach a value of unity. This procedure is illustrated in Figure 2.13. For HDPE, the crossover frequency measurements were taken at 200°C, 210°C and 220°C. For LDPE, the measurements were taken at 120°C, 130°C, 140°C, 150°C, 165°C and 170°C. In Figure 2.14, the complete results for the relaxation time measurements are given for both polymers. Note that for LDPE, the presented results are estimates using the procedure described in Figure 2.13. The temperature functionality of the relaxation times has been successfully fitted to an exponential function (eq. 2.44), which is also shown in Figure 2.14 for both polymers:

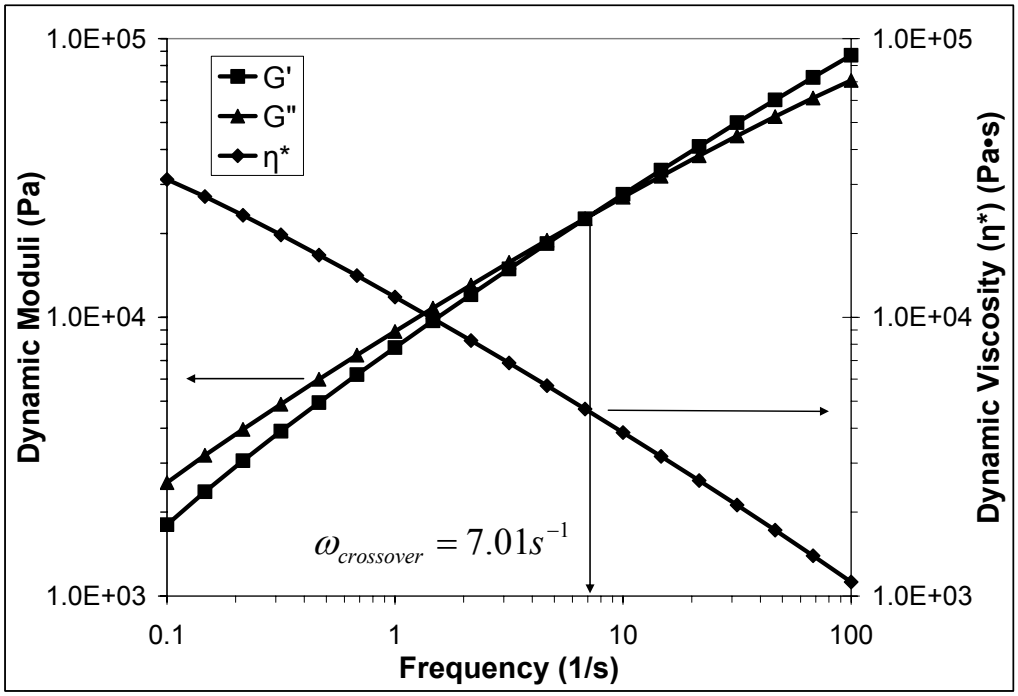

Figure 2.12: *Dynamic moduli G' and G" (left axis) and dynamic viscosity η* (right axis) for the HDPE melt at T = 190°C.*

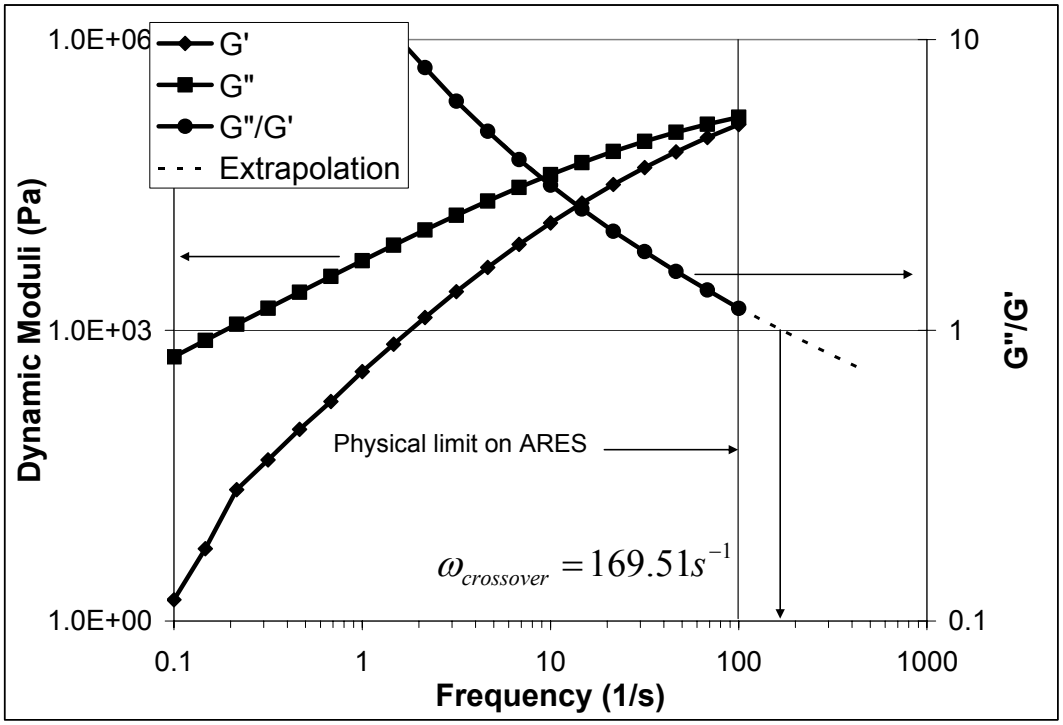

Figure 2.13: *Details of the method for estimating the crossover frequency outside the range of ARES for LDPE at T=120°C.*

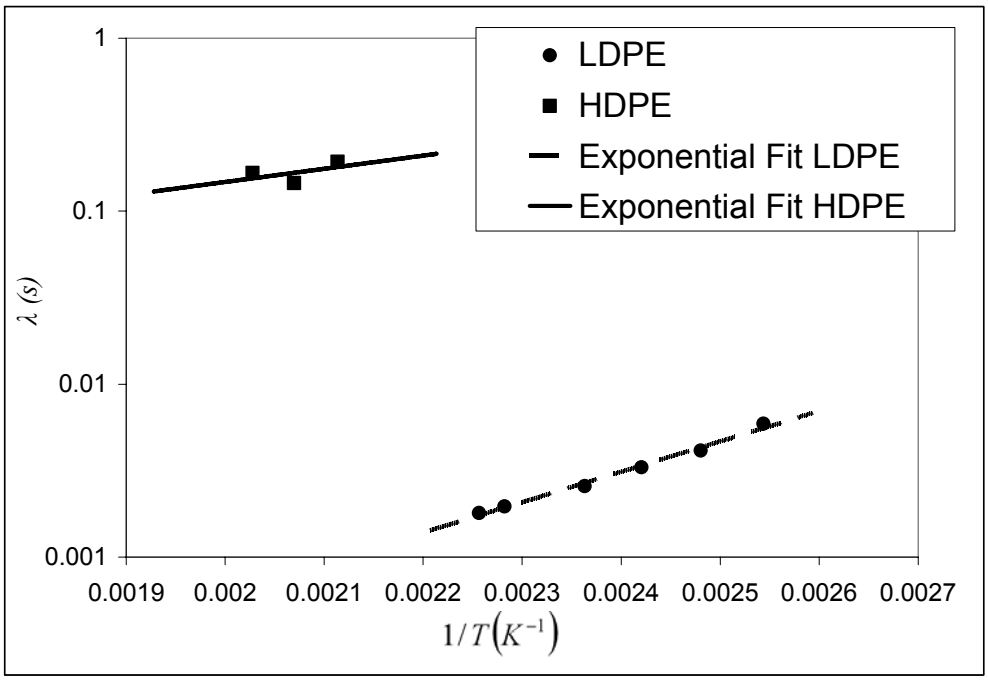

Figure 2.14: *Temperature dependence of the relaxation times for LDPE and HDPE.*

$$\lambda = A\exp\left(\frac{B}{T}\right) \tag{2.44}$$

where A and B are fitting constants. As expected, the relaxation time for both polymers is decreasing with temperature. Moreover, the relaxation times measured for HDPE are about two orders of magnitude larger than the ones estimated for LDPE.

This is not at all surprising, given the larger molecular weight of HDPE compared to LDPE (see Table 2.1). The exponential function fitting parameters in equation 2.44 are given in Table 2.3 below.

§2.5.5 *Conformation Tensor Predictions inside the Die Channel*

With the measured relaxation time λ, the diagonal components of the conformation tensor can be easily calculated using equations 2.41 and 2.42 for the UCMM, and by numerically integrating equation 2.43 for the single-mode Giesekus model. In this case it is useful to use the trace of the conformation tensor as the general descriptor for the degree of orientation achieved,

$$\mathrm{tr}(\tilde{\mathbf{c}}) = \tilde{c}_{xx} + \tilde{c}_{yy} + \tilde{c}_{zz} \tag{2.45}$$

Table 2.3 *Relaxation Time Exponential Fitting Parameters for HDPE and LDPE*

Polymer	A	B
HDPE	4.422738×10^{-3}	1.753809×10^{3}
LDPE	1.898411×10^{-7}	4.043431×10^{3}

As previously shown, the strain rate inside the die channel is independent of either axial or radial position, under the full-slip boundary condition assumption. Therefore, we would not expect any radial dependence of the conformation tensor either. However, as we have seen in §2.4.1, there are significant radial temperature gradients inside the die channel, which will definitely have an impact on the radial dependence of the relaxation time. According to equations 2.41, 2.42 and 2.43, the conformation tensor has an explicit dependence on the relaxation time; therefore it will also have a dependence on the radial position. For reasons of simplicity, we will consider the relaxation time as a constant throughout the entire spatial domain, with the value calculated for the temperature of the fluid at the die inlet. Under this assumption, the conformation tensor will only be a function of axial position z.

In Figure 2.15, the calculated $\mathrm{tr}(\tilde{\mathbf{c}})$ is given for the HDPE melt as a function of axial position at T_{in} = 190°C for selected elongation rates considered in the experiment. For clarity, it is convenient to normalize $\mathrm{tr}(\tilde{\mathbf{c}})$ with the value calculated at the exit (z = 25 mm). In Figure 2.16, the $\mathrm{tr}(\tilde{\mathbf{c}})$ values calculated at the die exit (z = 25mm) from the UCMM are given for the HDPE melt for all inlet temperatures and elongation rates.

First, in the case of UCMM we notice that the degree of orientation only approaches a constant value at the lowest elongation rates. As the elongation rate increases, the "degree of orientation" profiles shown in Figure 2.15a) change towards a steady increase with axial position, which becomes increasingly abrupt as the strain rate increases. In the case of the single-mode Giesekus model (Figure 2.15b), we notice the same qualitative behavior as in the UCMM case at the lowest strain-rates. At high

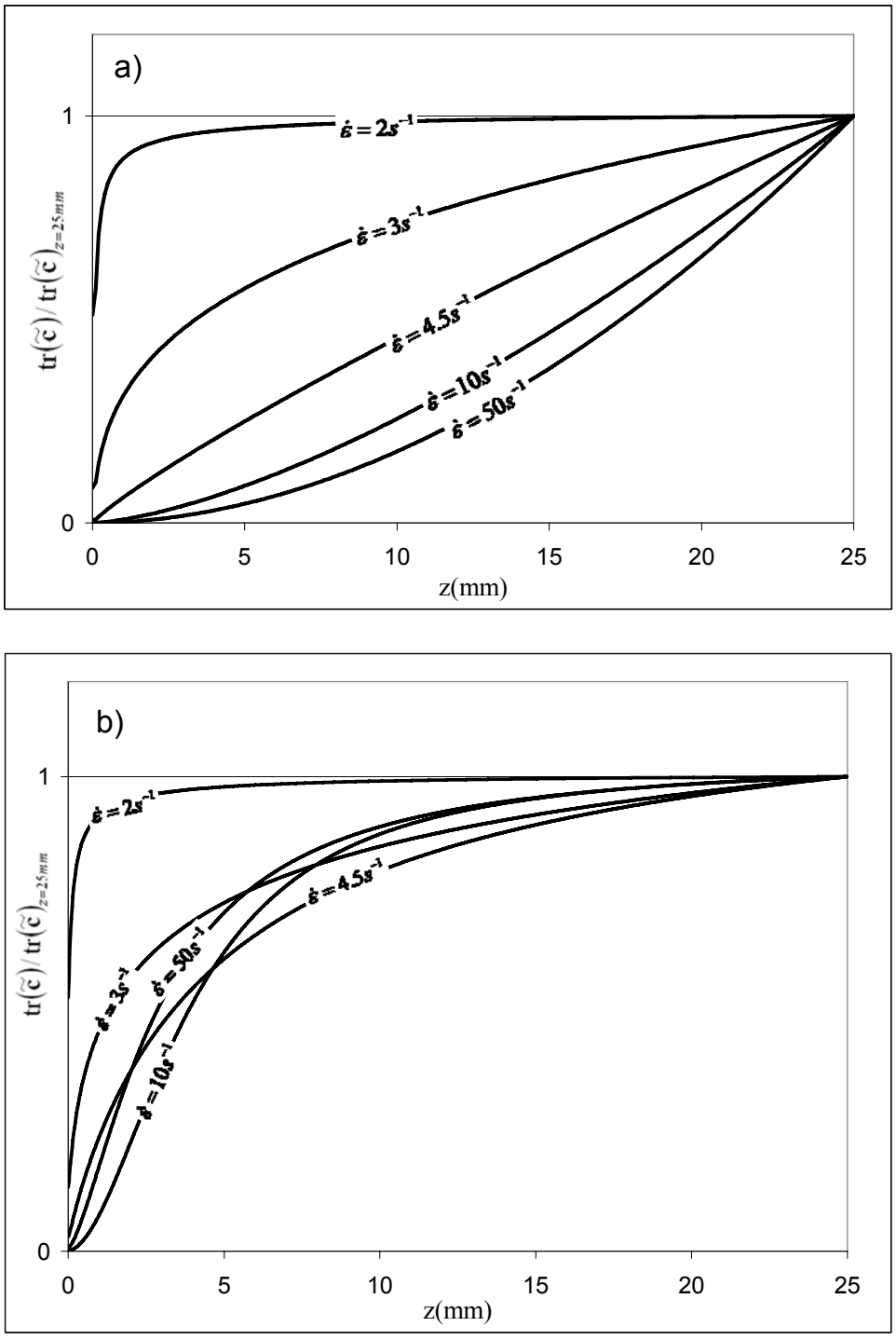

Figure 2.15: *Axial dependence of the degree of orientation for the HDPE melt at T = 190°C: UCMM a); Single-mode Giesekus model b).*

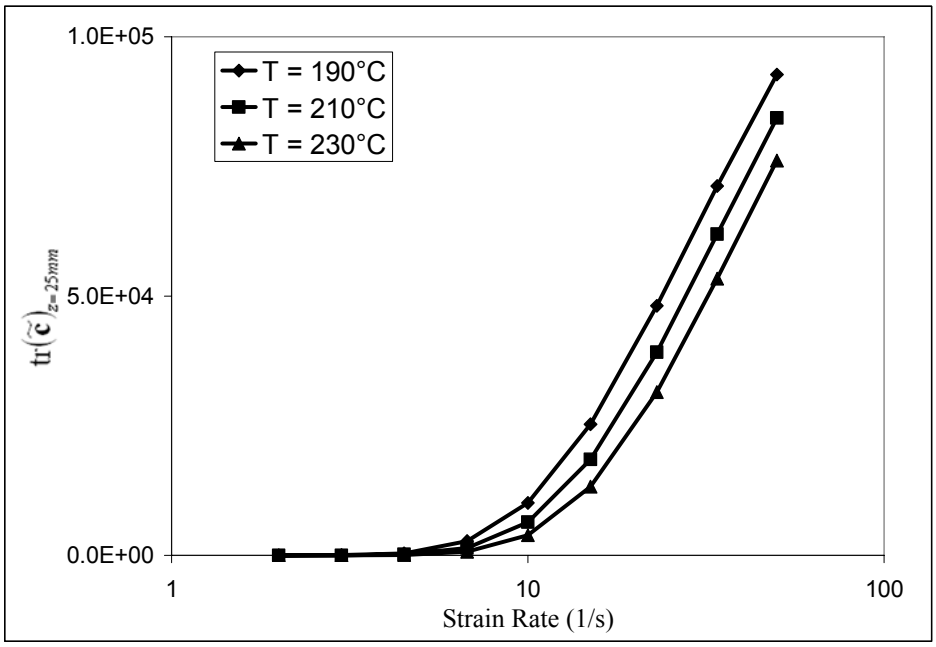

Figure 2.16: *Strain rate dependence of* $\mathrm{tr}(\tilde{\mathbf{c}})$ *at the die exit for the HDPE melt at* T_{in} *= 190°C, 210°C and 230°C from the UCMM.*

strain-rates, the parameter β acts to limit the growth of $\mathrm{tr}(\tilde{\mathbf{c}})$ towards a constant value. As we shall see later, the value of the parameter β that predicted the closest agreement with the experimental measurements is $\beta = 0.0065$. Perhaps the most important result of this analysis is the amazing qualitative agreement found between Figures 2.16 and 2.8. The trace of the conformation tensor (i.e., the degree of orientation) becomes important virtually in the same region in the strain-rate spectrum where we observed the deviations in Figure 2.8. Furthermore, the influence of the temperature seems to be preserved as well, and the same qualitative behavior with respect to temperature is observed in both figures. This new theoretical evidence seems to indicate a definite correlation between the degree of orientation and the region in the strain-rate spectrum where PEE is not obeyed. It is worth emphasizing that the data in Figure 2.16 was generated using the rather simplistic UCMM and the measured relaxation times. Therefore, the relaxation time may prove itself useful in predicting the region where the orientation effects in the energy balance of the system become important.

To emphasize the points made in the previous paragraph, the data in Figures 2.8 and 2.16 are shown together on the same plot in Figure 2.17. The trace of the conformation tensor is given on the left *y*-axis and is represented by the filled symbols, while the difference between the measured and the calculated temperature changes shown in Figure 2.8 represented by the open symbols is shown on the right *y*-axis. The diamond, square and triangle symbols represent data at inlet temperatures of 190°C, 210°C and 230°C respectively. The purpose of Figure 2.17 is to emphasize the almost

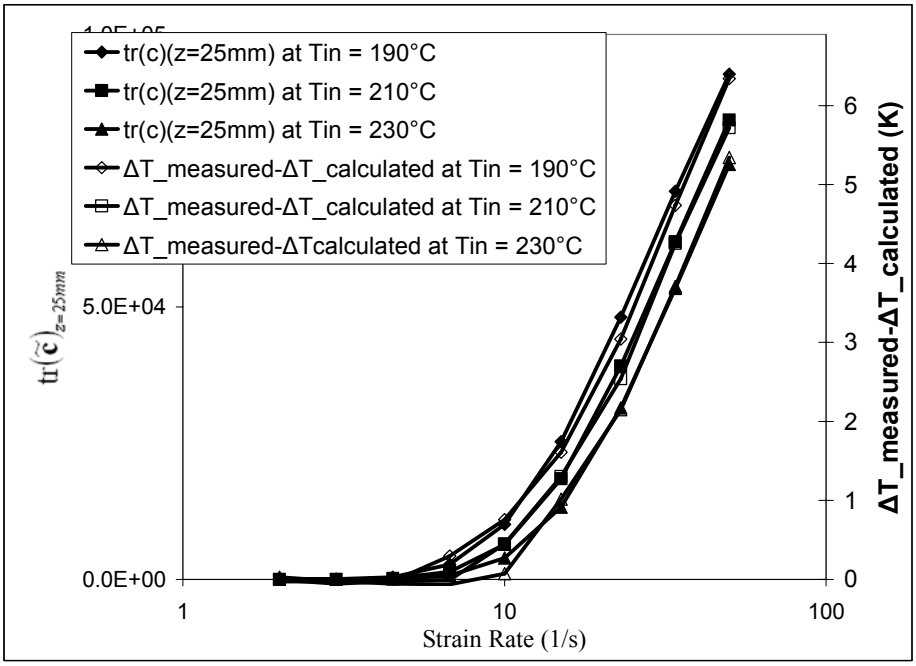

Figure 2.17: *Correlation between the degree of orientation developed in the die and the deviation of the measured temperature increase from the theoretical prediction.*

perfect correlation mentioned above, which was predicted by means of the UCMM and relaxation times alone.

§2.5.6 *The Complete Form of the Temperature Equation*

Let us have another look at the complete form of the temperature equation 1.17. If we rewrite it for an incompressible fluid at steady-state, we get

$$\rho\hat{c}_v\left(\mathbf{v}\cdot\nabla T\right)+\rho\left.\frac{\partial\hat{U}}{\partial\mathbf{c}}\right|_{T,V}:\left(\mathbf{v}\cdot\nabla\mathbf{c}\right)=k\nabla^2T+\left(\tau:\nabla\mathbf{v}\right) \tag{2.46}$$

Now, we shall focus our attention on the second term on the left side of equation 2.46. In Cartesian coordinates, considering the case of uniaxial elongational flow produced by the Hencky dies and *z* the direction of the elongation, ($\mathbf{v}\cdot\nabla\mathbf{c}$) becomes

$$\mathbf{v}\cdot\nabla\mathbf{c}=\begin{pmatrix} v_z\dfrac{\partial c_{xx}}{\partial z} & 0 & 0 \\ 0 & v_z\dfrac{\partial c_{yy}}{\partial z} & 0 \\ 0 & 0 & v_z\dfrac{\partial c_{zz}}{\partial z} \end{pmatrix} \tag{2.47}$$

For the same flow situation, the off-diagonal components of the conformation tensor are zero, and ($\partial\hat{U}/\partial\mathbf{c}$) is

$$\frac{\partial\hat{U}}{\partial\mathbf{c}}=\begin{pmatrix} \dfrac{\partial\hat{U}}{\partial c_{xx}} & 0 & 0 \\ 0 & \dfrac{\partial\hat{U}}{\partial c_{yy}} & 0 \\ 0 & 0 & \dfrac{\partial\hat{U}}{\partial c_{zz}} \end{pmatrix} \tag{2.48}$$

Performing the double-dot product in the second term on the left side of equation 2.46, we get:

$$\rho \frac{\partial \hat{U}}{\partial \mathbf{c}} : \left(v \cdot \nabla \mathbf{c} \right) = \rho v_z \left(\frac{\partial \hat{U}}{\partial c_{xx}} \frac{\partial c_{xx}}{\partial z} + \frac{\partial \hat{U}}{\partial c_{yy}} \frac{\partial c_{yy}}{\partial z} + \frac{\partial \hat{U}}{\partial c_{zz}} \frac{\partial c_{zz}}{\partial z} \right) \tag{2.49}$$

Typically, the conformation tensor component in the direction of the flow (c_{zz}) is several orders of magnitude larger than the other two diagonal components in the high flow rate regimes. Furthermore, the diagonal components of the conformation tensor normal to the direction of flow will asymptotically approach zero quite rapidly as a function of axial position z; therefore the first two terms inside the parentheses on the right side of equation 2.49 will be several orders of magnitude smaller relative to the third, and can be neglected. Combining equations 2.46 and 2.49, we can write an appropriate form for the temperature evolution equation,

$$\rho \hat{c}_v \left(v \cdot \nabla T \right) = k \nabla^2 T + \left[\left(\tau : \nabla v \right) - \rho v_z \left(\frac{\partial \hat{U}}{\partial c_{zz}} \frac{\partial c_{zz}}{\partial z} \right) \right] \tag{2.50}$$

Comparing this equation to the traditional form derived using PEE (for example equation 2.13), we notice the appearance of the extra heat generation term inside the square parentheses on the right side of equation 2.50. Normally, the minus sign in front of that term would indicate a heat loss, but as we shall see in our simulation results (see §3.3.2), the internal energy of the melt is decreasing with increasing degree of orientation. Therefore, the derivative $\partial \hat{U} / \partial c_{zz}$ will always be negative, making the extra term a generation term. Indeed, our experiments indicated that the traditional temperature equation 2.13 under-predicted the measured temperature profiles; therefore

the consistency with the present theory is preserved. Using equation 2.50, two corrections can be made to the traditional temperature equation. The first correction will involve introducing the conformation tensor functionality into the heat capacity (equation 1.18). In what follows, this correction will be referred to as "correction 1". The second correction will involve introducing the conformation dependence on the internal energy into the heat generation term. This will be referred to as "correction 2". Next, the relative importance of these two corrections will be discussed.

Using the same FEM procedure described in Section 2.4, the new temperature distribution equation 2.50 can be introduced and solved under the same conditions described therein. Having the functional forms for the conformation tensor components with respect to axial position completely defined (eqns. 2.41 and 2.42), we can easily evaluate the "conformational part" of the heat capacity (eq. 1.18) and the axial gradient of c_{zz} ($\partial c_{zz}/\partial z$). The only missing piece of the puzzle is $\partial \hat{U}/\partial c_{zz}$. Using UCMM, Dressler *et al.* [1, 2] derived the following functional form for the internal energy density of a fluid particle:

$$u = \frac{1}{2}\rho\alpha\left(K(T) - T\frac{\partial K(T)}{\partial T}\right)\mathrm{tr}(\mathbf{c}) \tag{2.51}$$

where u is the internal energy density of a fluid particle. At high degrees of orientation, the diagonal component of the conformation tensor in the direction of the deformation (c_{zz}) will be several orders of magnitude larger than the other two, which will make it identifiable with the trace of the conformation tensor $\mathrm{tr}(\mathbf{c})$. Consequently, the derivative

of the internal energy with respect to c_{zz} will be approximately equal to the derivative with respect to $\mathrm{tr}(\mathbf{c})$. Mathematically, this statement can be expressed as

$$c_{zz} \cong \mathrm{tr}(\mathbf{c}) \Rightarrow \frac{\partial \hat{U}}{\partial c_{zz}} \cong \frac{\partial \hat{U}}{\partial \mathrm{tr}(\mathbf{c})} \tag{2.52}$$

Combining equations 2.52 and 2.51 and transforming to proper dimensions, we get the following for the derivative of the internal energy with respect to c_{zz} from equation 2.50:

$$\frac{\partial \hat{U}}{\partial c_{zz}} = \frac{1}{2}\left(K(T) - T\frac{\partial K(T)}{\partial T} \right) \tag{2.53}$$

Combining equations 2.53, 3.15 and 3.17, we get

$$\frac{\partial \hat{U}}{\partial c_{zz}} = \frac{1}{2} k_B T (B+1) \tag{2.54}$$

For this analysis, the value for B is taken as the experimentally measured one by Flory for a polyethylene melt [46] (B = − 1.45) (see §3.3.1 for details). Equations 2.51 thorough 2.54 will also apply to the single-mode Giesekus model, since it shares the same Hamiltonian with the UCMM [20]. However, in the case of the single-mode Giesekus model, the conformation tensor components and their derivative with respect to axial position will be different from the UCMM, as given by equation 2.43. With the extra generation term in equation 2.50 completely defined, a new set of FEM calculations have been performed in order to determine the relative magnitude of corrections 1 and 2 mentioned above. First, let us examine the total heat capacity (eq. 1.18) as a function of axial position for the HDPE melt at T_{in} = 190°C. In Figure 2.18, the total heat capacity with the UCMM conformation tensor is shown for selected strain-rates. We observe a reduction in the heat capacity of up to 18% at the die exit for

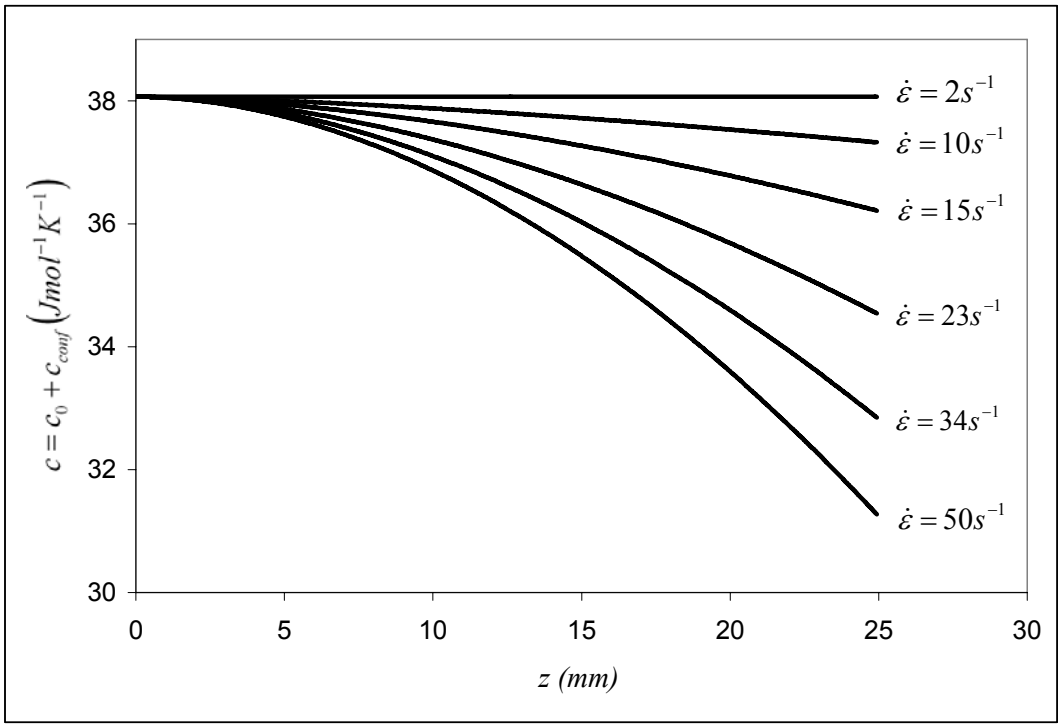

Figure 2.18: *The total heat capacity predicted by UCMM for the HDPE melt at T_{in} = 190°C.*

the highest strain-rate. The axial position functionality can then be embedded into the modeling equation 2.50 in the FEM code. This will account for correction 1 defined above. Next, the extra heat generation term can be input into the FEM software as given by equations 2.54 and 2.42 for the UCMM. In the case of the single-mode Giesekus model, the derivative of the internal energy with respect to c_{zz} will also be given by equation 2.54, while the numerical solution to equation 2.43 will be used to obtain the derivative of c_{zz} with respect to axial position z. In Figure 2.19, we present the temperature changes due to viscous heating calculated using the traditional temperature equation 2.13 (no correction), the measured temperature changes and the calculated temperature profiles by adding corrections 1 and 2 to the traditional temperature equation for the HDPE melt at T_{in} = 190°C.

Even though the predicted heat capacity changes are quite significant (see Figure 2.18), correcting for the conformational part of the heat capacity yields results that are virtually indistinguishable from the ones calculated the traditional way. By contrast, including the extra generation term into the temperature equation yields a significant improvement over the previous results that are in improved quantitative agreement with the measured values. However, as we see clearly from Figure 2.19, adding correction 2 from the UCMM yields a slight over-prediction of the measured values. Using the single-mode Giesekus model and different values for the parameter β, an iterative procedure has been employed in order to match the measured temperature profiles. The value of β that yielded the best predictions was β = 0.0065. It is worth emphasizing that for β = 0, the UCMM is recovered. The value found from our

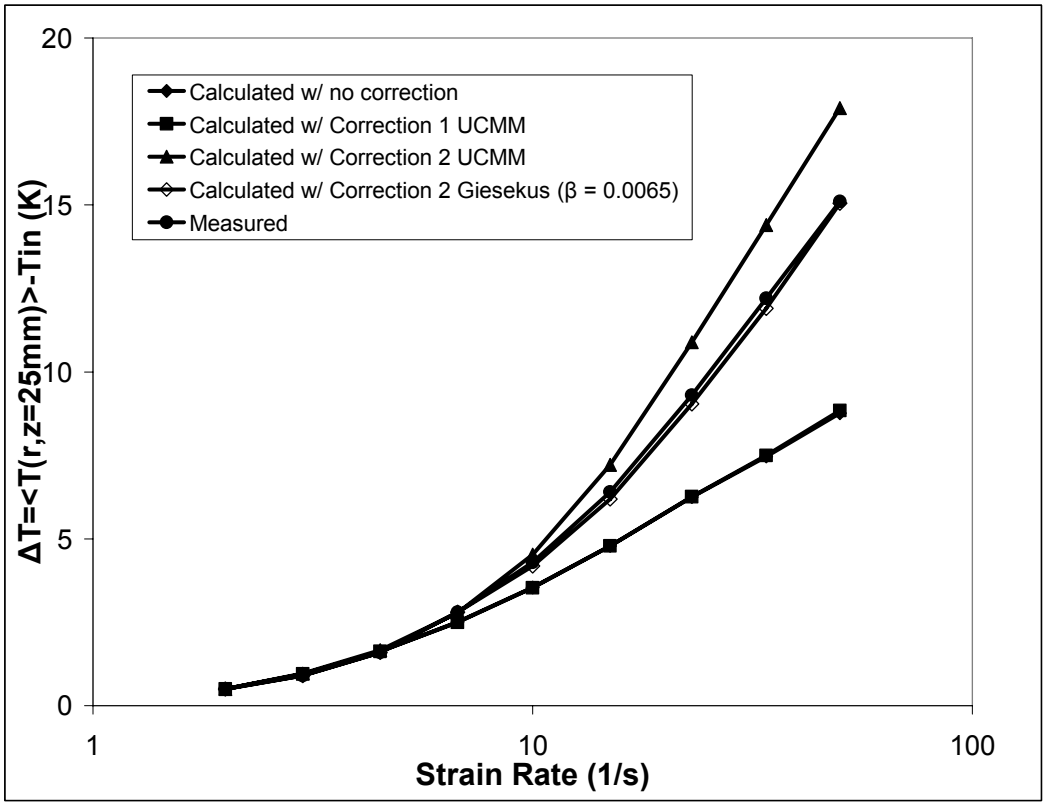

Figure 2.19: *Relative effects of correcting for the conformational part of the heat capacity (correction 1) and for the extra heat generation term (correction 2) in the calculated temperature profiles for the HDPE melt at* T_{in} *= 190°C.*

calculations of 0.0065 is not too far from zero, which substantiates the fact that the correction needed for the UCMM was minimal.

2.6 Concluding Remarks

In this chapter, we have established that the assumption of PEE is not universally valid, as previously believed. We have shown clear experimental evidence that the assumption of PEE is not valid for both polymers studied at high strain rates. Furthermore, it has been shown that temperature and molecular architecture have a profound effect on the measured temperature profiles relative to the predicted ones.

This statement has two major consequences with far reaching implications. First, the classical temperature evolution equation 1.12 used so far in nearly every engineering analysis of non-isothermal polymer flows only seems to be valid for low deformation rates. For wider ranges of deformation rates when significant orientation is present, a more general form of the temperature evolution equation is needed (eq. 1.17), which contains additional terms accounting for internal structural contributions to the internal energy. However, as shown in Section 1.3, under appropriate flow conditions, these terms can vanish. In the case of elongational flow generated inside the Hencky dies investigated in this chapter, the fluid is not homogeneous in terms of internal orientation ($\nabla \mathbf{c} \neq 0$), thus the second term on the left side of equation 1.17 is non-zero. As we have shown in §2.5.6, the extra term accounting for internal orientation is significant, therefore it should be included in a complete analysis. Furthermore, we have

proposed a recipe for estimating that term using molecular theory. Second, the constant volume heat capacity ceases to be a constant with respect to deformation rate at high degrees of orientation. This behavior needs to be incorporated into the temperature evolution equation as well. However, we have shown that incorporating the structural information into the heat capacity has a negligible effect on the predicted temperature profiles. This statement may not be true if a different flow situation is modeled. For example, if there is significant orientation present, but there are no orientation gradients in the fluid (i.e., the flow is homogeneous), then the heat capacity will drop to a fraction of its equilibrium value throughout the entire spatial domain. In this case, the heat capacity will have a more significant impact on the predicted temperature profiles.

In Chapter 3, molecular simulation will be used to help us get a better understanding of the reasons why PEE is not universally valid for polymer melts. To this end, a series of detailed atomistic simulations of long linear alkanes under non-equilibrium conditions will be performed in order to establish the relationship between the internal energy and the internal degree of orientation.

Chapter 3

Molecular Simulation of Oriented Polymer Melts

3.1 Introduction

From an experimental perspective, studying the structure-property relationships in a polymeric material is not always an easy task. Over the past three decades, computer simulation techniques have been developed as useful tools to aid researchers in understanding many problems concerning the dynamic, structural and thermodynamic properties of physical systems.

Computer simulation techniques can be divided into four major categories: quantum methods, in which the length scales involved are sub-atomic and the time scales involved are sub-femtosecond; molecular level methods, in which the length scales are on the order of nanometers, and time scales are on the order of nanoseconds; mesoscale methods, which employ time scales on the order of microseconds and length scales on the order of micrometers; and continuum methods, in which finite element techniques are used to model macroscopic time and length scales. All of these methods are inter-related and complementary to each other, and are designed to investigate

different aspects of a particular problem. For example, quantum methods involve solving Schrödinger's equation for a particular group of atoms, and are generally used to generate interaction potential functions that are further used in the molecular level methods. Molecular Dynamics (MD) and Monte-Carlo (MC) simulation techniques are the most widely used methods to investigate properties at the molecular level and were originally developed to study simple fluids, or low molecular weight compounds. This was due in part to the limited availability and performance of computational resources at the time. Simulating systems of up to a few thousand particles over a few nanoseconds was very challenging to most supercomputers available in the 1960's and 1970's. Nowadays, computers have developed tremendously and billion particle simulations have been achieved.

In general, relatively small systems are required to generate thermodynamic properties of small molecular weight compounds. This is not the case for polymer systems. Unlike small molecule compounds, polymers exhibit a wide spectrum of time and length scales characterizing their dynamic behavior and internal structure. This is the source of many challenges to be overcome when simulating polymeric systems. With the rapid advancements of computational capabilities and the development of new, accurate algorithms, molecular simulation of polymeric systems is becoming increasingly available. While generating structural and thermodynamic properties for polymeric systems at equilibrium is relatively easy and employs the use of relatively short chains, simulating such systems under flow conditions is still under development. While there has been a large amount of effort dedicated to studying polymeric systems

under shear flow (see for example [47-49]), studying polymeric systems under elongational flow is still in the developmental stage. Notable is the work of Baig and coworkers, in which a theoretically sound nonequilibrium molecular dynamics (NEMD) algorithm for simulating planar elongational flow of n-alkane systems of up to 128 carbon atoms was developed [50, 51].

Typically, MD methods are used when dynamic information such as viscosity or diffusion coefficients is needed. Given the large relaxation times of polymeric systems, simulation times on the order of tens of nanoseconds are often required to sample such properties. On the other hand, when static properties such as internal conformation, density or internal energy are needed, nonequilibrium Monte Carlo (NEMC) methods emerged as a very useful tool for efficiently sampling such properties away from equilibrium for systems inaccessible to NEMD [52-57].

Recently, Mavrantzas and co-workers developed a novel molecular simulation framework for simulating long chain alkane systems away from equilibrium [53-57] based upon a very efficient Monte-Carlo algorithm developed earlier by Pant and Theodorou [52]. The focal point of this algorithm is the so called “end-bridging” move, which allows chains to be broken and reformed according to a prescribed chemical potential. This introduces polydispersity in the system in the sense that chain lengths are uniformly distributed within a pre-defined interval, and around a pre-defined average value. The computational efficiency was evaluated for this algorithm by simulating alkane systems up to 500 carbon atoms in length. It was concluded that the end-bridging algorithm is a least two orders of magnitude faster in equilibrating long chain systems

than any other molecular simulation method known at the time. Surprisingly, it was also shown that the algorithm was faster as the average length of the simulated chains increased. This is somewhat counterintuitive, but its explanation lies at the very heart of the algorithm. The longer the chains, the more options there are for them to break and recombine, thus the greater acceptance ratio of the end-bridging move.

The non-equilibrium version of this algorithm was developed for simulating oriented alkane melts under an applied uniaxial orienting field. This was accomplished by defining a set of thermodynamic conjugate variables (the conformation tensor **c** and the "orienting field" $\boldsymbol{\alpha}$) [53]. Later, a different approach has been taken in order to develop a similar thermodynamic framework called GENERIC MC [56]. This time, the conjugate variables were introduced as proper Lagrange multipliers, and a slightly different form for the "orienting field" $\boldsymbol{\alpha}$ was derived, which eliminated unwanted density fluctuations observed using the original form.

In this chapter, we use the same procedure to simulate systems with average chain lengths between 24 and 78 carbon atoms, at temperatures between 300K and 450K, with applied "orienting fields" of varying strength. We are greatly indebted to Dr. Vlasis Mavrantzas for lending us the NEMC source codes.

3.2 Simulation Methodology

In a typical Monte-Carlo algorithm, the initial configuration is defined by a set of Cartesian coordinates defining the position in space of every interaction site (or

atom). The algorithm starts by randomly picking an atom or group of atoms and applying a random displacement to them. Then, the energy of the new system is evaluated, and the move is accepted or rejected with a probability that is dependent on temperature and the energy of the new system. The art in a Monte-Carlo simulation lies in the choice of the type of move, as well as the proportion of moves attempted.

In the NEMC procedure used in this work, the following mix of attempted moves was used: reptations, 10%; rotations, 2%; flips, 6%; intra-chain bridges, 32%; end-bridges, 49%; volume fluctuations, 1%. These moves, as well as the choice of percentages from the total number of attempted moves have been discussed in detail previously [53, 54]. In the course of a simulation, the total number of chains *N*, the total number of particles *n*, the pressure *b*, the temperature *T* and the relative chemical potential μ^* are kept constant (the *NnbT*μ^* ensemble).

§3.2.1 *Thermodynamic Considerations*

Following the definition of the conformation tensor **c** (eq. 1.13), it is more convenient to work in terms of the normalized confirmation tensor $\tilde{\mathbf{c}}$:

$$\tilde{\mathbf{c}} = 3\frac{\mathbf{c}}{\left\langle R^2 \right\rangle_0} = \mu\mathbf{c} \tag{3.1}$$

where $\left\langle R^2 \right\rangle_0$ is the mean-squared end-to-end distance, taken as an ensemble average over all chains at equilibrium and μ is the normalization factor. Clearly, by definition, the normalized conformation tensor $\tilde{\mathbf{c}}$ at equilibrium is the identity matrix **I**. At this

point, it is postulated that the Helmholtz free energy function governing the oriented melt has a direct dependence on $\tilde{\mathbf{c}}$:

$$\frac{A}{N_{ch}} = \frac{A}{N_{ch}}\left(\rho, T, \tilde{\mathbf{c}}\right) \tag{3.2}$$

where ρ is the mass density, T is the temperature and N_{ch} is the number of chains.

Then, the "orienting field" $\boldsymbol{\alpha}$ is introduced as the thermodynamic conjugate variable to $\tilde{\mathbf{c}}$:

$$\alpha_{\gamma\delta} = \frac{1}{k_B T}\left[\frac{\partial}{\partial \tilde{c}_{\gamma\delta}}\frac{A}{N_{ch}}\left(\rho, T, \tilde{\mathbf{c}}\right)\right]_{T,\rho,\tilde{c}_{[\gamma\delta]}} \tag{3.3}$$

In equation (3.3), the orienting field $\boldsymbol{\alpha}$ is defined at constant density ρ. However, the NEMC simulations are performed at constant pressure b, therefore it is more useful to define a new thermodynamic potential function (the Gibbs free energy function) by performing a Legendre transformation of the Helmholtz free energy with respect to V/N_{ch} and $\tilde{\mathbf{c}}$:

$$\frac{G}{N_{ch}}\left(b, T, \alpha\right) = \frac{A}{N_{ch}}\left(\rho, T, \tilde{\mathbf{c}}\right) + \frac{b}{\rho}\frac{M}{N_A} - k_B T\alpha : \tilde{\mathbf{c}} \tag{3.4}$$

where G is the Gibbs free energy function, M is the number average molecular weight of the chains, N_A is Avogadro's number and $k_B T\alpha : \tilde{\mathbf{c}}$ is the term accounting for the energy of the imposed field.

We now have the definition of a thermodynamic potential function in terms of our control quantities (b,T and $\boldsymbol{\alpha}$). It immediately follows that

$$\widetilde{c}_{\gamma\delta} = -\frac{1}{k_B T}\left[\frac{\partial}{\partial \alpha_{\gamma\delta}}\frac{G}{N_{ch}}(b,T,\alpha)\right]_{T,b,\alpha_{[\gamma\delta]}} \tag{3.5}$$

where $\alpha_{[\gamma\delta]}$ represents all other components of the orienting field tensor $\boldsymbol{\alpha}$ except $\alpha_{\gamma\delta}$.

Our ultimate goal in these simulations is to evaluate the change in the Helmholtz free energy with respect to the quiescent melt. To this end, equation 3.4 presents itself as very useful. By performing simulations with applied orienting fields of varying strength, the conformation tensor can be easily calculated and the Gibbs free energy can then be evaluated via a simple thermodynamic integration:

$$\frac{G}{N_{ch}} - \frac{G_0}{N_{ch}} \equiv \frac{G}{N_{ch}}(b,T,\alpha) - \frac{G}{N_{ch}}(b,T,\mathbf{0}) = -k_B T\left[\sum_{\gamma}\sum_{\delta}\int_0^{\alpha_{\gamma\delta}} \widetilde{c}_{\gamma\delta}\,\mathrm{d}\alpha_{\gamma\delta}\right]_{T,b,\alpha_{[\gamma\delta]}} \tag{3.6}$$

Combining equations 3.4 and 3.6, the following is obtained for the change in Helmholtz free energy:

$$\frac{A}{N_{ch}} - \frac{A_0}{N_{ch}} = -k_B T\left[\sum_{\gamma}\sum_{\delta}\int_0^{\alpha_{\gamma\delta}} \widetilde{c}_{\gamma\delta}\,\mathrm{d}\alpha_{\gamma\delta}\right]_{T,b,\alpha_{[\gamma\delta]}} - b\frac{M}{N_A}\left(\frac{1}{\rho} - \frac{1}{\rho_0}\right) + k_B T\boldsymbol{\alpha} : \widetilde{\mathbf{c}} \tag{3.7}$$

Moreover, the internal energy U/N_{ch} can be evaluated directly from simulation by evaluating the total interaction energy between selected pairs of sites in the system according to prescribed interaction functions, which make up the so-called "force field".

§3.2.2 *Potential Model Details*

The force field used in this study is the Siepmann-Karaborni-Smit (SKS) force field [58], which was specifically parameterized to fit experimental thermodynamic data for alkane systems. In the SKS description, there are two types of interactions present in

the system: bonded interactions and non-bonded interactions. The CH_2 groups that form the molecular chain are collapsed into a single interaction site, by using the so-called "united atom" approach. This approach is possible given the relative small size of the hydrogen atoms when compared to the carbon atoms. It is well known in the simulation community that the computational expense is proportional to the second power of the number of sites in the system [59]. By collapsing the CH_2 group into a single interaction site, the total number of particles in the system is reduced by a factor of three, yielding a reduction of about one order of magnitude in the computational expense, without any loss in accuracy. From this point on, we will refer to the CH_2 sites as "atoms".

Typically, the total potential energy function in a molecular level simulation is given as

$$U = U_{bond} + U_{angle} + U_{torsion} + U_{non-bonded} \tag{3.8}$$

where U_{bond}, U_{angle} and $U_{torsion}$ represent the "bonded" interactions while $U_{non\text{-}bonded}$ represents the "non-bonded" interactions and may include van der Waals terms, coulombic terms etc.

In equation 3.8, U_{bond} represents the covalent bond-stretching interaction (Fig. 3.1a) and is typically represented by a harmonic spring with an equilibrium length r_0. In the SKS description, this term is omitted and the covalent chemical bonds are modeled as rigid rods 1.54Å in length. U_{angle} describes the angle bending interaction between two covalent bonds (Figure 3.1b) and is given by a harmonic potential around an equilibrium value θ_0,

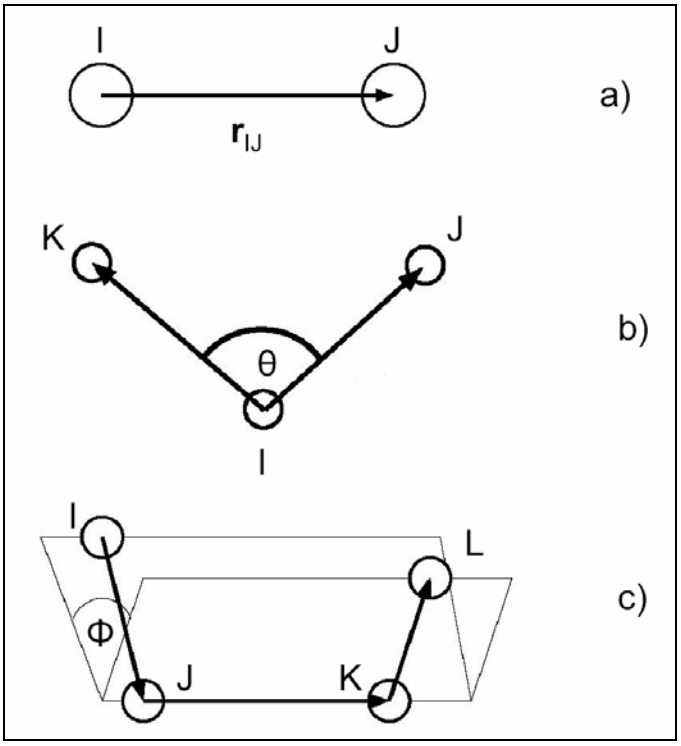

Figure 3.1: *Schematic representations of bond stretching interaction a); angle bending interaction b); torsion interaction c).*

$$U_{angle} = \frac{1}{2} k_\theta (\theta - \theta_0)^2 \tag{3.9}$$

where k_θ is the harmonic spring constant. The torsional potential $U_{torsion}$ is described by a function proposed by Jorgensen and co-workers [60],

$$U_{torsion} = \sum_{k=0}^{3} a_k (\cos \Phi)^k \tag{3.10}$$

where a_k are constants and Φ is the dihedral angle depicted in Figure 3.1c).

The non-bonded interactions are given by a 12-6 Lennard-Jones (LJ) interaction potential (eq. 3.11). Non-bonded interactions occur between atoms on the same chain separated by mode than three covalent bonds, and between all atoms belonging to separate chains. For computational cost reduction, the non-bonded potential is truncated for distances grater than a specified cutoff radius (r_{cut}) [59]. In this study, a cutoff radius of 2.8·σ was chosen [53, 56].

$$U_{non-bonded} = 4\varepsilon \left[\left(\frac{\sigma}{r} \right)^{12} - \left(\frac{\sigma}{r} \right)^{6} \right] \tag{3.11}$$

In Table 3.1, the summary of the force field as well as the parameters for each type of interaction is presented.

With the interaction potentials defined, the total potential energy over the course of a simulation run can be calculated as an ensemble average over all configurations. Since the simulations are performed at constant temperature, there would be no change in kinetic energy; the change in the internal energy of an oriented configuration with respect to equilibrium will be given by the difference between the average total potential energy of the oriented system and the average total potential energy of the

Table 3.1. *Details of the Potential Model Used in the Simulations*

Type	Functional Form	Parameters
U_{bond}	Rigid $r=r_0$	r_0 = 1.54Å
U_{angle}	$\frac{1}{2}k_\theta(\theta-\theta_0)^2$	k_θ/k_B=62500 K/rad^2 θ_0=114^o
$U_{torsion}$	$\sum_{k=0}^{3} a_k(\cos\Phi)^k$	a_0/k_B = 1010 K a_1/k_B = 2019 K a_2/k_B = 136.4 K a_3/k_b = - 3165 K
$U_{non\text{-}bonded}$	$4\varepsilon\left[\left(\frac{\sigma}{r}\right)^{12}-\left(\frac{\sigma}{r}\right)^{6}\right]$	$\varepsilon_{CH_2}/k_B=\varepsilon_{CH_3}/k_B=47$ K $\sigma_{CH_2}=\sigma_{CH_3}=3.93$ Å

system at equilibrium:

$$\frac{\Delta U}{N_{ch}}=\frac{\langle U\rangle}{N_{ch}}(\rho,T,\mathbf{c})-\frac{\langle U\rangle}{N_{ch}}(\rho,T,\mathbf{I}) \tag{3.12}$$

This equation will not only allow us to calculate the change in the total internal energy, but also it will allow us to calculate individual contributions from different types of interactions present (see equation 3.8).

§3.2.3 *Simulated System Details*

Using the Monte-Carlo procedure described above, four different systems of linear alkane chains of increasing average molecular weight have been considered. The average chain lengths for the four systems are as follows: system 1, with an average chain length of 24 carbon atoms; system 2, with an average chain length of 36 carbon atoms; system 3, with an average chain length of 50 carbon atoms; system 4, with an average chain length of 78 carbon atoms. From this point onward, these systems will be

referred to as C_{24}, C_{36}, C_{50} and C_{78} respectively. One of the most appealing aspects of the end-bridging algorithm is the ability to generate polydisperse systems of controlled molecular weight distribution. As in refs. [53, 56], the molecular weights for the systems considered in this study were uniformly distributed between $0.5 \cdot \langle \mathrm{MW} \rangle$ and $1.5 \cdot \langle MW \rangle$, corresponding to polydispersity indices of ≈ 1.09 (see Table 3.2). For example, for the C_{24} system the chain lengths were uniformly distributed between 12 and 36 carbon atoms. For all systems, the input configurations were initially well equilibrated using an Equilibrium Molecular Dynamics (EMD) code, DL_POLY_2.0 [61]. The equilibration was performed at a constant temperature of 500K under constant pressure conditions (1 atm.) for a period of 2.5 ns. The well-equilibrated configurations thus obtained were then input into the NEMC code as initial configurations for each run. The applied orienting field $\boldsymbol{\alpha}$ employed was in the form proposed by Mavrantzas and Öttinger [56], and corresponds to a uniaxial extensional field in the *x* direction:

$$\alpha = \begin{pmatrix} \alpha_{xx} & 0 & 0 \\ 0 & -\alpha_{xx}/2 & 0 \\ 0 & 0 & -\alpha_{xx}/2 \end{pmatrix} \tag{3.13}$$

Table 3.2. *Molecular Aspects of the Simulated Systems*

System	*N* (total number of chains)	*n* (total number of particles)	*MWDI* (distribution interval)	*PI* (polydispersity index)
C_{24}	100	2400	12 – 36	1.0902
C_{36}	64	2304	18 – 54	1.0953
C_{50}	49	2450	25 – 75	1.0866
C_{78}	40	3120	39 – 117	1.0854

Clearly, the magnitude of α_{xx} uniquely defines the "strength" of the orienting field. Therefore, α_{xx} will be used from this point on as a basis to relate various physical properties to the strength of the orienting field. For all systems, simulations were carried out with α_{xx} ranging from 0.0 (equilibrium case) to 0.7 in 0.1 increments. To investigate temperature effects, separate runs were performed at 300K, 350K, 400K and 450K for all systems and field strengths considered. In Table 3.2, the molecular aspects of the systems considered are presented in terms of average chain lengths, distribution intervals, number of chains, number of atoms and polydispersity indices.

3.3 Results and Discussion

§3.3.1 *The Mean-Squared End-to-end Distance*

First, let us look at the simulated equilibrium properties. Perhaps the most useful quantity that can be evaluated from the equilibrium simulations is the mean-squared end-to-end distance $\left\langle R^2 \right\rangle_0$. This quantity will let us define two other useful parameters, which will be extensively used in our analysis; namely, the conformation tensor normalization factor μ (see equation 3.1) and the overall chain spring constant *K(T)* [1, 2]. These quantities are defined as

$$\mu = \frac{3}{\left\langle R^2 \right\rangle_0} \tag{3.14}$$

$$K(T) = \frac{3k_B T}{\left\langle R^2 \right\rangle_0} = \mu k_B T \tag{3.15}$$

As detailed in ref. [20], *K(T)* originated from early statistical models of chain molecules, and was taken as a linear function of temperature (i.e., μ was taken as independent of temperature) under the assumption that the internal free energy of an ensemble of polymer chains was purely entropic in nature. Later, this assumption was removed, and an energetic component to the free energy was identified based upon the nonlinearity of *K(T)* with temperature [1, 2]. Moreover, the same study identified a "conformational component" to the heat capacity (see equation 1.18), which came as the first theoretical suggestion that the heat capacity of a polymer melt changes with degree of orientation.

Let us now examine the behavior of the mean-squared end-to-end distance with respect to chain length and temperature. Following a similar procedure as in ref. [53], $\left\langle R^2 \right\rangle_0$ can be calculated from one simulation for the entire molecular weight distribution interval. In Figure 3.2, $\left\langle R^2 \right\rangle_0$ is given for all four systems investigated at 450K as a function of chain length. Notice the seamless overlap in the regions where chains having the same length are found in two adjacent systems. The scatter found in the C_{78} system data is attributed to poor statistical sampling in the calculation of the ensemble average. The C_{78} system contains only 40 chains, while the molecular weight interval spans over 78 carbon atoms. By contrast, the C_{24} system contains 100 chains, while the molecular weight interval spans over 24 carbon atoms, resulting in much better statistics. Mavrantzas and Theodorou fitted the equilibrium mean-squared end-to-end distance data to a polynomial expression with very good results [53]:

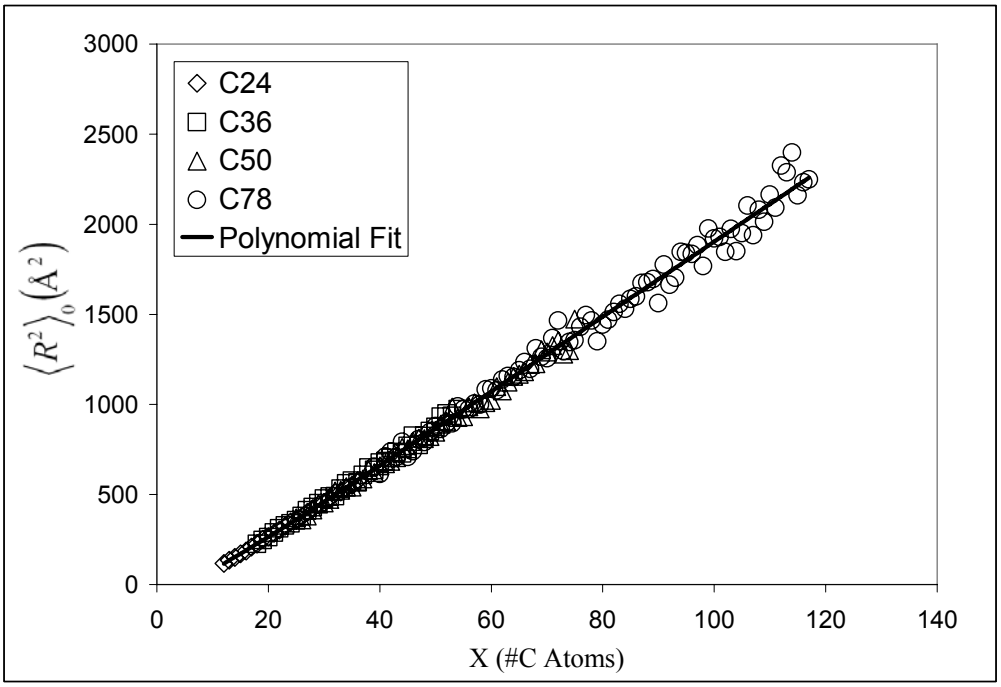

Figure 3.2: *Equilibrium mean-squared end-to-end distance at T=450K.*

$$C_X \equiv \frac{\left\langle R^2 \right\rangle_0}{(X-1)b^2} = \alpha_0 + \frac{\alpha_1}{X-1} + \frac{\alpha_2}{(X-1)^2} + \frac{\alpha_3}{(X-1)^3} \tag{3.16}$$

where C_x is the "characteristic ratio", X is the number of carbon atoms in a chain, b is the C-C bond length in Å (1.54Å) and α_i (i = 0 - 3) are fitting constants. In Table 3.3, the fitting constants derived from the equilibrium simulations in this study are given, along with the published ones from the previous study [53]. However, in the previous study, only data from the C_{24} and C_{78} systems were used at a single temperature (450K). In this study, the $\left\langle R^2 \right\rangle_0$ data in the overlap regions was averaged, and the average value was considered in the polynomial fitting.

As pointed out in ref. [53], α_0 is the characteristic ratio at infinite chain length C_∞. The value reported in this study at 400K is slightly lower than the one previously reported [53], and closer to C_∞ = 7.8 ± 0.4 measured for polyethylene using neutron diffraction at 413K [62, 63].

Table 3.3. *Characteristic Ratio Fitting Parameters*

Temperature	α_0	α_1	α_2	α_3
450K	8.8427	-77.9066	521.951	-2141.85
400K	8.6677	-30.5968	-681.681	6030.121
350K	9.219	-9.298	-1573.36	13064.89
300K	11.9351	-183.756	2022.19	-9320.51
450K [53]	9.1312	-75.1865	315.742	-500.3518

In Figure 3.3, the results of the polynomial fits in terms of $\langle R^2 \rangle_0$ are plotted against chain length (X). We observe a very close agreement between our own results and those previously published. Furthermore, we observe a strong temperature effect in $\langle R^2 \rangle_0$ in the sense that as the temperature is lowered, $\langle R^2 \rangle_0$ increases. In most cases this aspect has been overlooked before, and $\langle R^2 \rangle_0$ (or $\mu = 3/\langle R^2 \rangle_0$) was taken as independent of temperature, with some exceptions [2, 64]. The temperature dependence of μ was introduced by Gupta and Metzner [64] into an extra term in their constitutive equation to account for non-isothermal effects. Under isothermal conditions, their model reduces to the UCMM. By contrast to our simulation results, they report an increase in $\langle R^2 \rangle_0$ with increasing temperature. However, we found that the functional form for μ fitted our simulation data very well, except for the opposite behavior observed:

$$\mu = \nu T^{-(B+1)} \tag{3.17}$$

where ν and B are fitting constants. Gupta and Metzner pointed out that B is a number greater than –1, and ν is a positive constant. With B greater than –1, μ will decrease with decreasing temperature and $\langle R^2 \rangle_0$ will increase with temperature. Our simulation results seem to suggest the opposite effect (see Figure 3.3). However, our simulation results are in good quantitative agreement with data reported by Flory [46] for cross-linked polyethylene at 140°C ($\partial \ln \langle R^2 \rangle_0 / \partial T = -1.1 \cdot 10^{-3} K^{-1}$). If we combine equations 3.14 and 3.17 and take the derivative with respect to temperature, we obtain B = – 1.45 from Flory's data.

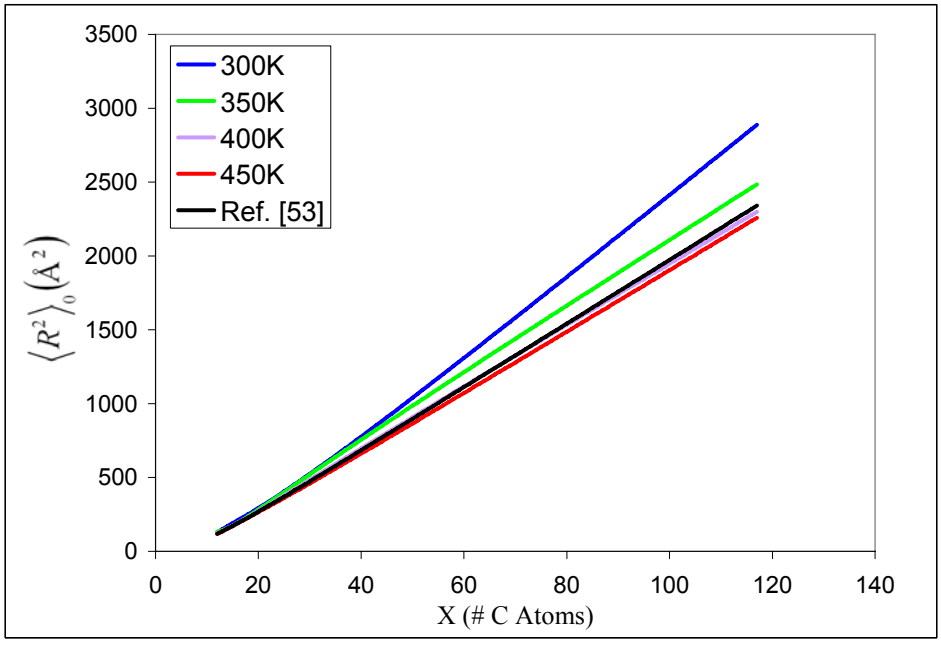

Figure 3.3: $\langle R^2 \rangle_0$ *polynomial fits using equation 3.16 and the fitting parameters in Table 3.3.*

In Figure 3.4, the temperature exponent B resulting from fitting the data in Figure 3.3 is plotted against chain length. We observe that the temperature exponent extrapolates to $B = 1$ at zero chain length (i.e., no temperature dependence in μ). The temperature exponent B decreases with increasing chain length, and seems to asymptote a constant value of 1.62 for very high chain lengths, not too far from the reported experimental value (see previous paragraph).

§3.3.2 *Energy Balances for the Oriented Systems*

The equilibrium simulations provided two very important bits of information that are useful in the next step in our analysis: first, they provided the normalizing coefficient μ and its temperature dependence, which will be used further for calculating the normalized conformation tensor for the oriented systems; second, they provided the reference for calculating the change in internal energy of the oriented structures (eq. 3.12). Furthermore, it was shown that $\left\langle R^2 \right\rangle_0$ is indeed dependent on temperature, and corrections to existing data [53] need to be made in order to calculate the correct normalized conformation tensors.

Next, we proceeded to examine these systems with the orienting field turned on. First, we needed to make sure that there are no system-size effects influencing the results. It is well known that highly oriented polymer chains may develop unphysical artifacts introduced by interactions between extended images of the same chain.

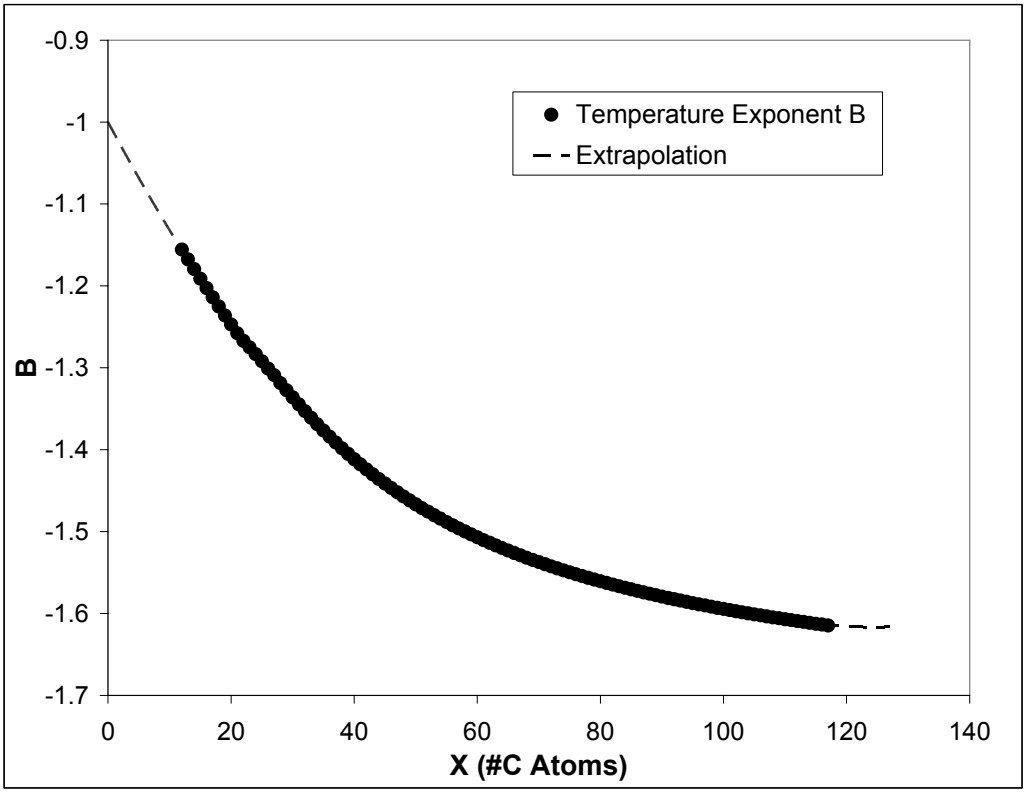

Figure 3.4: *The temperature exponent B with respect to chain length.*

These artifacts are known to induce "premature crystallization", and can be eliminated by increasing the system size. To test the system-size effect, we picked the C_{78} system as being the most vulnerable to such artifacts (because it had the largest molecular weight). We then generated two additional systems two and four times larger than the original system (6240 and 12480 particles respectively) and monitored the evolution of all three systems under applied orienting fields with α_{xx} up to 0.7 at T = 450K. We monitored all relevant quantities (energies, conformation tensor, end-to-end vector auto-correlation functions) for symptoms of "premature crystallization", and concluded that within statistical uncertainty, all these quantities converged to the same value for a sufficiently large number of iterations. It is worth pointing out that the computational toll of a typical Monte-Carlo code is proportional to the second power of the number of particles (N^2); therefore, by doubling the system size, we would essentially need to quadruple the simulation time in order to generate the same statistics. Therefore, we concluded that for the range of field strengths employed in this study, larger systems would not be necessary.

Let us now examine the conformation tensor (or more conveniently, its normalized form) calculated for the oriented structures. By definition (eq. 3.1), the normalized conformation tensor $\tilde{\mathbf{c}}$ is symmetric and reduces to the unit tensor **I** at equilibrium for any given temperature. When the orienting field is applied, the chains will adopt extended conformations, oriented in the direction of the deformation and $\tilde{\mathbf{c}}$ will depart from its equilibrium value. In this situation, the degree of extension and orientation will be uniquely described by the six independent components of $\tilde{\mathbf{c}}$.

Following the definition of the orienting field $\boldsymbol{\alpha}$ (eqns. 3.3, 3.5 and 3.13), one would expect the off-diagonal components of $\tilde{\mathbf{c}}$ to be zero as well. Indeed, our simulations confirmed the diagonal form of $\tilde{\mathbf{c}}$, therefore the trace of $\tilde{\mathbf{c}}$ (tr($\tilde{\mathbf{c}}$)) will be used to quantify the degree of extension and orientation generated by the orienting field in our simulations. In Figure 3.5, we examine the molecular weight (Fig. 3.5a) and the temperature (Fig. 3.5b) effect on conformation as the strength of the orienting field α_{xx} is increased. As expected, we observe an increase of the degree of orientation with molecular weight at a particular temperature, given the fact that the relaxation time increases with molecular weight (Fig. 3.5a). For the same reason, we observe an increase in the degree of orientation with decreasing temperature for a particular molecular weight (C_{36}, Fig. 3.5b).

Having performed the conformation tensor $\tilde{\mathbf{c}}$ calculations for every molecular weight, temperature T and field strength α_{xx}, the Helmholtz free energy $\Delta A/N_{ch}$ relative to the unperturbed state can now be easily calculated by performing a series of thermodynamic integrations (eq. 3.7). Furthermore, the change in internal energy $\Delta U/N_{ch}$ with respect to equilibrium is readily available directly from simulation, which allows us to compare the two quantities directly.

In Figure 3.6 we present the molecular weight effect on $\Delta A/N_{ch}$ and $\Delta U/N_{ch}$ at 450K (Fig. 3.6a) and the temperature effect on the same quantities for the C_{36} system (Fig. 3.6b). First, we observe that $\Delta A/N_{ch}$ and $\Delta U/N_{ch}$ are of about the same magnitude and opposite sign for all cases considered. This suggests that the internal energy is a very important component of the free energy in the energetic balance of the system.

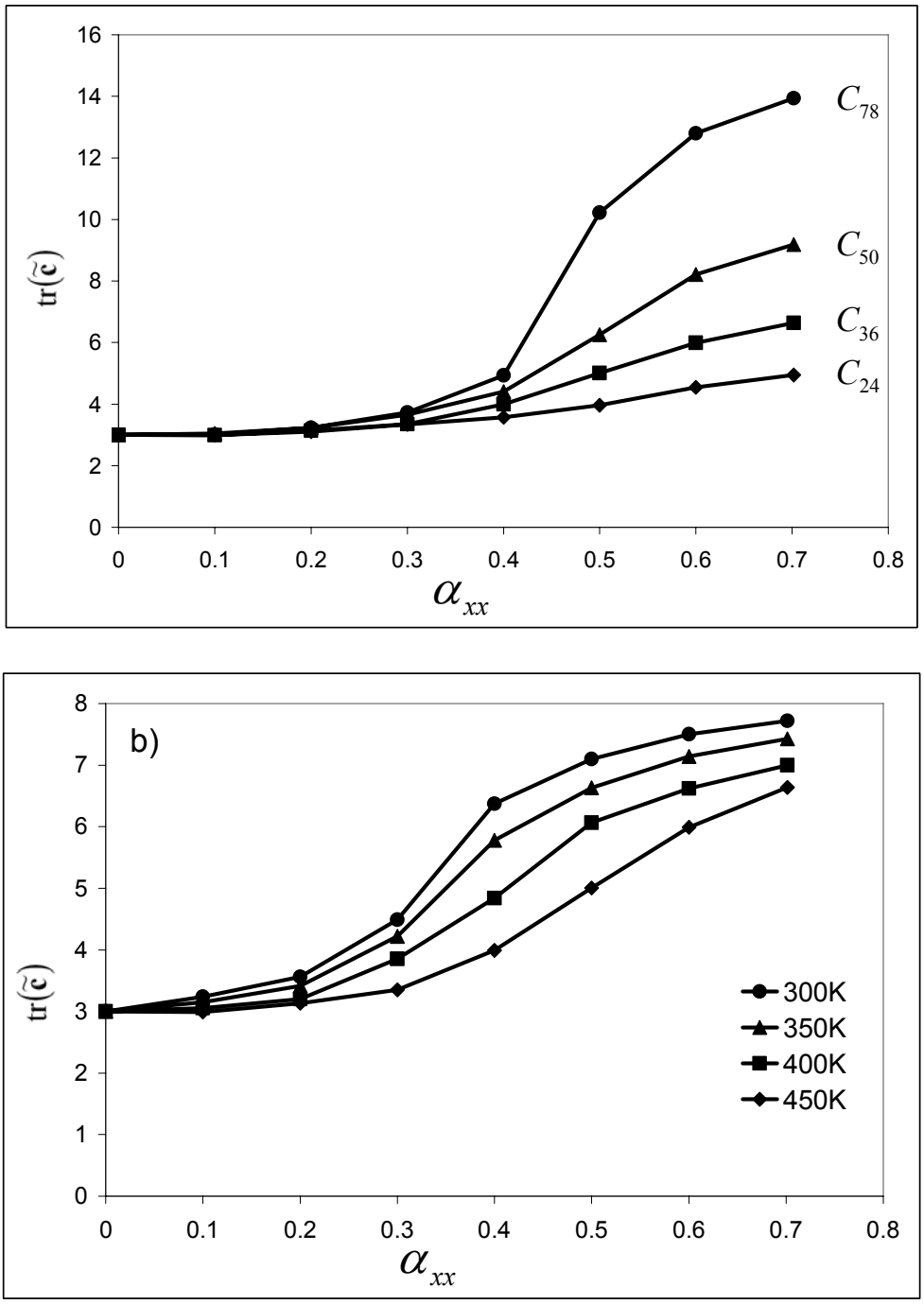

Figure 3.5: *Molecular weight effect on conformation at T = 450K a); temperature effect on conformation for the C_{36} system b).*

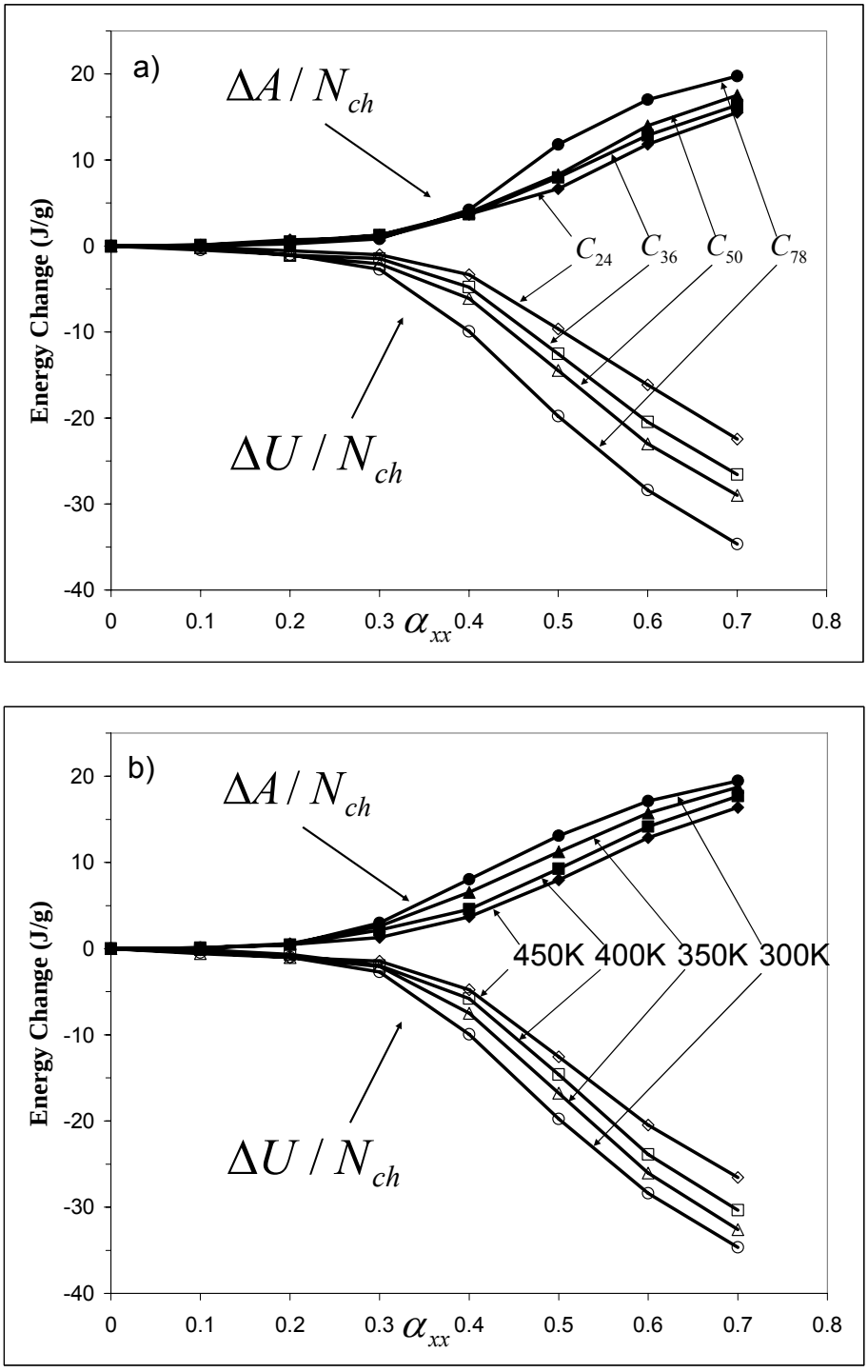

Figure 3.6: *Molecular weight influence on the change in internal and Helmholtz free energy at T = 450K a); temperature influence on the change in internal and Helmholtz free energy for the C_{36} system b).*

Furthermore, mirroring the results presented in Fig. 3.5, we see the same behavior in terms of the free energy change as a function of both molecular weight and temperature. This is not at all surprising, since the change in free energy has an explicit dependence on the conformation tensor (see eq. 3.7).

If we examine the molecular weight behavior of the change in internal energy, we see that as the chain length increases, the decrease in internal energy for a given temperature and field strength is more pronounced. In our simulations, we have the ability to evaluate the inter-molecular and intra-molecular contributions to the non-bonded energy separately. As we shall see later, the most important contributor to the total energy of the system is the intermolecular non-bonded energy. As the molecular weight increases, it is easier for the chains to establish favorable side-side interactions, generating a more pronounced decrease in the total internal energy. The temperature dependence of the internal energy (Fig. 3.6b) can be explained using the same line of thought. As the temperature decreases, the relaxation time of the chains will increase, thus making it easier for the chains to align and develop side-side interactions for a given field strength.

As mentioned earlier, we have the ability to investigate the individual contribution of each type of interaction to the total internal energy (see §3.2.2 – Table 3.1). According to equation 3.8, the total potential energy is equal to the sum of all bonded and non-bonded interactions. In our simulations, the bonded interactions are represented by the angle bending and torsion interaction potentials (see Figure 3.1), while the non-bonded interactions are represented by the 12-6 LJ pair interaction

potential (eq. 3.11). The non-bonded interactions can further be split into two distinct contributions: the intra-molecular interactions, in which pairs of atoms belonging to the same chain separated by more than three covalent bonds interact through the LJ potential; and the inter-molecular interactions, in which all pairs of atoms belonging to different chains interact through the same potential. This distinction is important, because as it will be shown in Figure 3.7, the two components exhibit opposite behavior with respect to degree of orientation. The potential energy balance of the system in terms of the change in energy relative to equilibrium can be written as

$$\frac{\Delta U_{total}}{N_{ch}} = \frac{\Delta U_{angle}}{N_{ch}} + \frac{\Delta U_{torsion}}{N_{ch}} + \frac{\Delta U_{intra}}{N_{ch}} + \frac{\Delta U_{inter}}{N_{ch}} \tag{3.18}$$

In Figure 3.7, the four energetic components on the right side of equation 3.18 are given for the C_{24} system at $T = 400$K as a function of α_{xx}. As previously mentioned, it is clear from Figure 3.7 that the two components of the non-bonded energy are of opposite sign and different in magnitude. The orienting field has almost no effect on the angle-bending energy, while the torsional energy is decreasing because in the extended chains, the lower energy *trans* dihedral conformations are enhanced. In a previous discussion (see Section 1.2) it was mentioned that for a single isolated chain, the internal energy of the extended chain does not change significantly with degree of extension, thus the purely entropic elastic response. This behavior can easily be explained upon close examination of Figure 3.7.

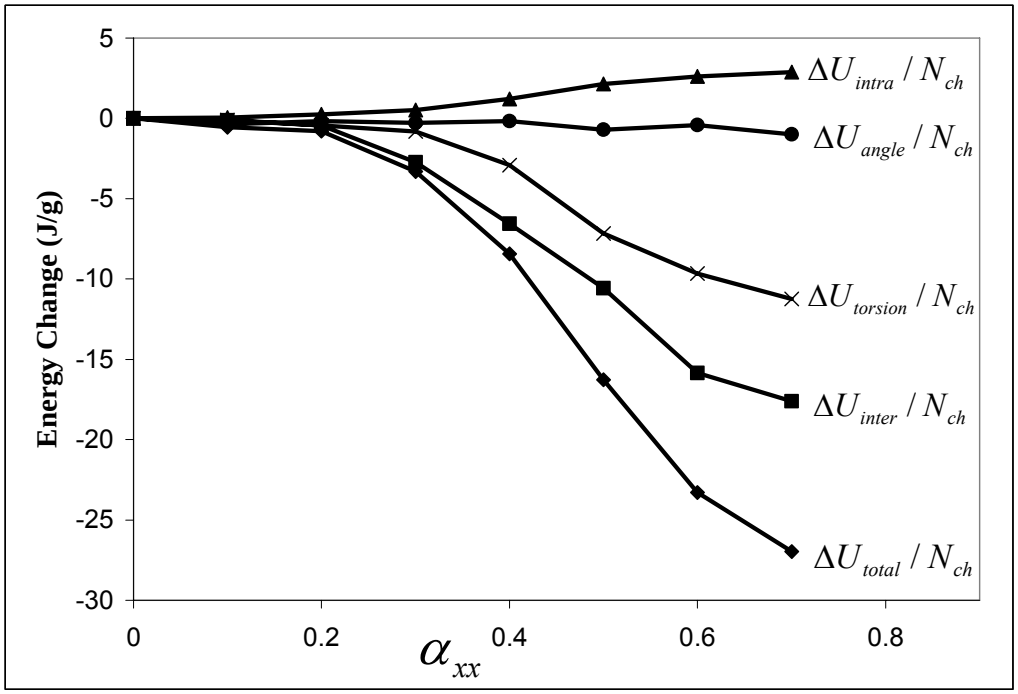

Figure 3.7: *Individual component contributions to the total internal energy change for the C_{24} system at T = 400K.*

Unless extreme conditions are applied (i.e., the chain is fully extended, and additional energy is put into bending the valence angles), the angle energy does not change with degree of extension. With increasing deformation, the dihedral angles on the chain will gradually start to adopt the *trans* conformation (their lowest energy configuration), thus reducing the overall torsion energy, while the intra-molecular LJ energy will increase due to greater distances between the pairs of atoms in the extended configurations. It is clear from Figure 3.7 that the changes in torsional and intra-molecular potential energies are of about the same magnitude and opposite sign, offsetting each other.

Of course, in a molecular level simulation, the extent to which these energy components will change will be sensitive to the potential model used. It has been suggested that the potential model used in this study to describe the torsional interactions is in fact artificially enhancing the *trans* conformations, which explains the over-prediction of the characteristic ratio at infinite chain length C_∞ when compared to experiment [53]. A more realistic potential model for the torsional angles would yield a smaller decrease in the torsional term at a given extension.

Another important conclusion to be drawn from the analysis of Figure 3.7 is the fact that the most important contributor to the change in total energy is the inter-molecular LJ energy. This is perhaps the most important conclusion from our simulations, and explains why the *Purely Entropic Elasticity* assumption is not applicable to polymer melts. While the total internal energy of a single isolated chain may not change with extension (due to the two components discussed above offsetting

each other), the internal energy of an *ensemble* of chains will change significantly, due to favorable inter-chain interactions that will lower the overall energy. Macroscopically, this will translate into additional energy being generated within the material, increasing the temperature of the fluid. Indeed, this aspect is confirmed by our experimental observations in which the calculated temperature increase due to viscous heating using the PEE assumption is under-predicted by up to a factor of two at the highest strain-rates (see §2.4.2 – Figures 2.8 and 2.9).

The change in Helmholtz free energy $\Delta A/N_{ch}$ can also be evaluated by using the UCMM [1, 2, 56]:

$$\frac{\Delta A}{N_{ch}} = \frac{1}{2} k_B T \left(\mathrm{tr}\left(\tilde{\mathbf{c}}\right) - 3\right) - \frac{1}{2} k_B T \ln\left(\det\left(\tilde{\mathbf{c}}\right)\right) \tag{3.19}$$

This expression was derived as the elastic contribution to the thermodynamic potential of the Hookean dumbbell model with infinite chain extensibility, accounting for the internal microstructure [1, 2]. Using equation 3.19, the UCMM change in Helmholtz free energy can be calculated directly using the normalized conformation tensor data from the simulations, without the need for thermodynamic integration. In Figure 3.8, $\Delta A/N_{ch}$ is shown for the C_{78} system at T = 450K calculated via the thermodynamic integration method (eq. 3.7) and using the UCMM (eq. 3.19). We observe an excellent agreement between the two methods.

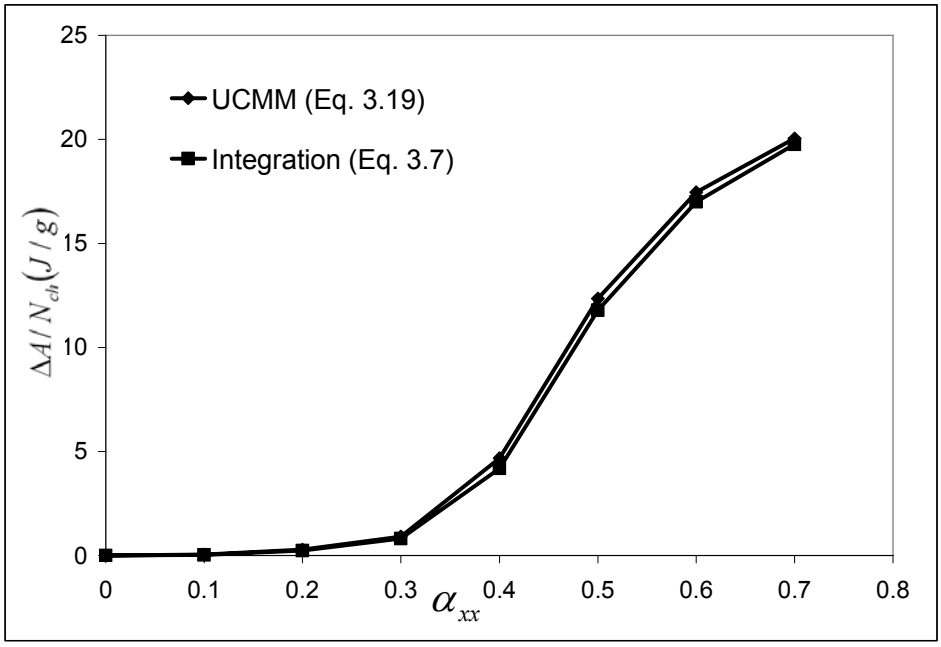

Figure 3.8: *UCMM performance for predicting $\Delta A/N_{ch}$ for the C_{78} system at T = 450K.*

§3.3.3 *Conformation Dependent Heat Capacity*

As mentioned earlier, Dressler and co-workers used the UCMM to derive the "conformational component" to the heat capacity [1, 2] (see equation 1.18).

$$c_{conf} = -\frac{1}{2}\alpha T \frac{\partial^2 K(T)}{\partial T^2}\left(\mathrm{tr}(\mathbf{c}) - \mathrm{tr}(\mathbf{c}_0)\right) \tag{3.20}$$

The second derivative of the chain spring constant *K(T)* can be easily evaluated by using the conformation tensor normalization factor μ and the temperature exponent *B* obtained by fitting the equilibrium simulation data (see figure 3.4). Combining equations 3.15 and 3.17 and taking the second derivative of *K(T)* with respect to temperature, we find

$$\frac{\partial^2 K(T)}{\partial T^2} = \frac{B(B+1)\mu k_B}{T} \tag{3.21}$$

Plugging 3.21 into 3.20 and using

$$\mathrm{tr}(\tilde{\mathbf{c}}) = \mu \mathrm{tr}(\mathbf{c}) \tag{3.22}$$

we obtain the following for the conformational part of the heat capacity:

$$c_{conf} = -\frac{1}{2}\alpha B(B+1)\left(\mathrm{tr}(\tilde{\mathbf{c}}) - 3\right) \tag{3.23}$$

With the conformation tensor and the temperature exponent *B* already available from the simulations, the molecular weight dependence of c_{conf} is presented in Figure 3.9a) and the temperature dependence of c_{conf} is presented in Figure 3.9b). Since c_{conf} has a linear dependence on $\mathrm{tr}(\tilde{\mathbf{c}})$, the behavior we see in Figure 3.9 is in fact mirroring the behavior we observed earlier in Figure 3.5.

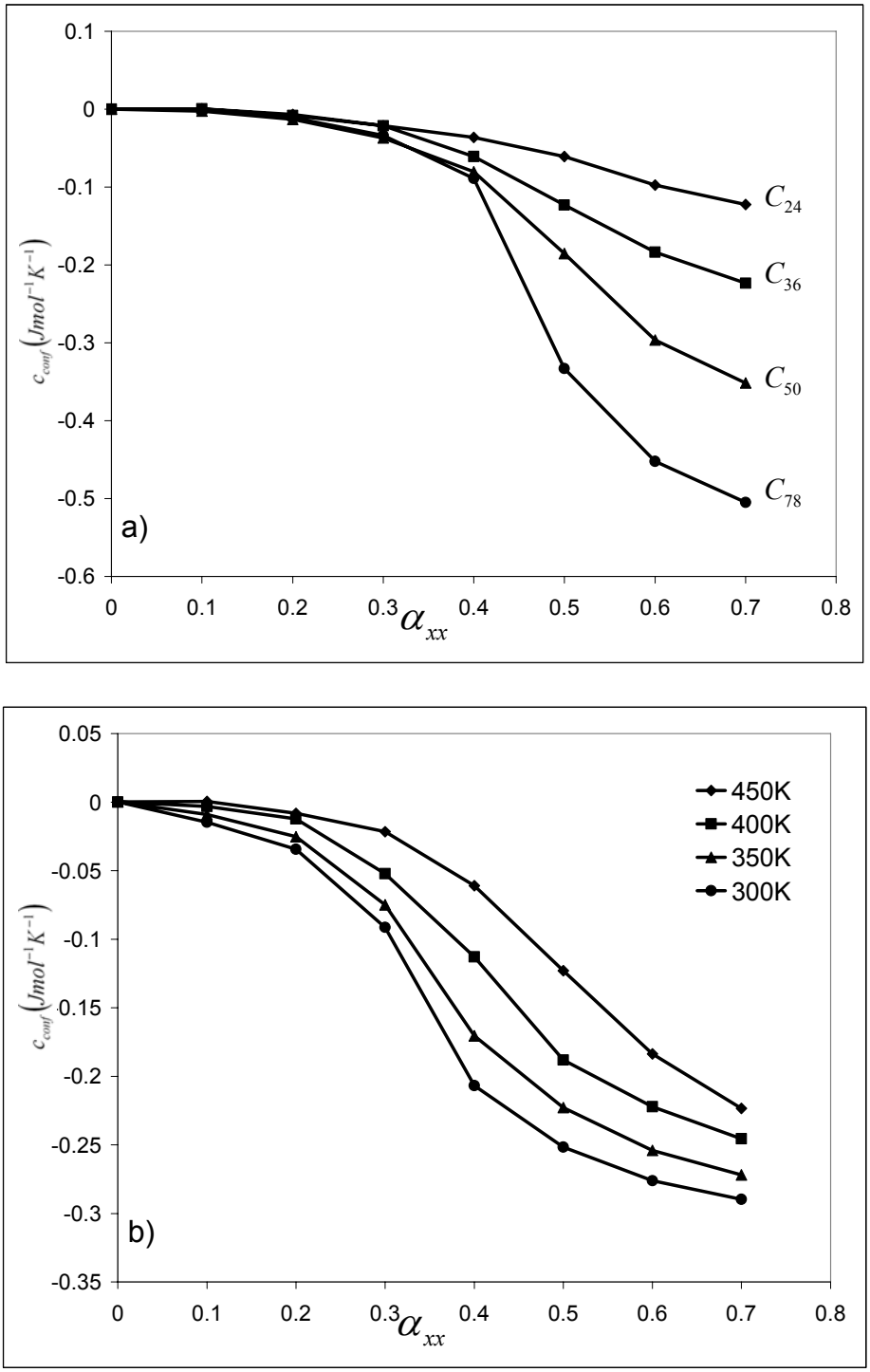

Figure 3.9: *Molecular weight dependence of c_{conf} at T = 450K a); temperature dependence of c_{conf} for the C_{36} system b).*

The behavior of c_{conf}, coupled with the behavior of the internal energy components (see Figure 3.7), provides us with the theoretical bases for the hypotheses made in the concluding section of Chapter 2. Even though a rather simplistic model has been used to calculate c_{conf}, these results predict the same qualitative trends we saw during the experiments. Furthermore, the direct calculation of the internal energy change indicates a strong dependence on the degree of orientation. In the concluding section of Chapter 2, we identified two possible corrections that would bring agreement between the calculated and the measured temperature profiles, which are both consequences of the PEE assumption being invalid: first, the heat capacity had to decrease at high strain rates; and second, the internal energy had to decrease with $\tilde{\mathbf{c}}$. The simulation results seem to substantiate both of these corrections.

3.4 Concluding Remarks

The atomistic molecular simulation results presented in this chapter come to complement and substantiate the experimental results presented in Chapter 2. Furthermore, new molecular insights have been given to explain the trends and the deviations from theory observed during the experiments. First, we examined some equilibrium properties for the systems investigated. It was shown that the chain spring constant *K(T)* is not a linear function of temperature, as was previously assumed. The temperature exponent *B* was calculated for chain lengths between C_{12} and C_{117}, and excellent agreement with previous experimental measurements and simulation results

was found. Later, we used the temperature exponent B in order to calculate the "conformational part" of the heat capacity, and the trends observed are in excellent qualitative agreement with our own experimental measurements. Examining the behavior of the internal energy components, we gained new and useful insights into the molecular aspects of PEE, and we indicated the reasons why we expect it to fail in describing oriented polymer melts. Qualitatively, we confirmed the two possible reasons for the failure of PEE in our experiments.

Chapter 4

Structure Formation under Steady-State Isothermal Planar Elongational Flow of *n*-Eicosane: A Comparison between Simulation and Experiment

This chapter is a revised version of a journal article by the same name published in *Physical Review Letters* in 2006 by T.C. Ionescu, C. Baig, B.J. Edwards, D.J. Keffer, and A. Habenschuss:

T.C. Ionescu, C. Baig, B.J. Edwards, D.J. Keffer, and A. Habenschuss: *Structure formation under steady-state isothermal planar elongational flow of n-eicosane: A comparison between simulation and experiment.* Physical Review Letters, 2006. **96**(037802).

My contributions to this article include: (1) performing the structural analysis of the configurations resulting from nonequilibrium molecular dynamics (NEMD) and equilibrium molecular dynamics (EMD) simulations and (2) preparation of the published manuscript. In this chapter, by the use of "we" I will refer to all five authors of the article.

4.1 Introduction

The crystallization of polymer melts under flow has generated a tremendous amount of interest over the years. Understanding crystallization mechanisms, kinetics, and crystallite morphologies are just a few of the problems that present an ongoing interest among research communities [65-67]. Short and long chain *n*-alkanes have been

extensively used to model the behavior of polyethylene, in particular, and polymers in general. In practice, polymers are known to form ordered domains when subjected to deformation either in the melt or solid states. In industrial applications such as fiber spinning or film blowing, this phenomenon is desired, and a precise control over the nucleation rates, crystallite growth, and morphology is critical. From an experimental perspective, it is very challenging to investigate the individual phenomena taking place during polymer crystallization, given the different length and time scales involved. This is why molecular simulation is potentially the ideal tool for investigating these processes.

Crystallization of long chain molecules from quiescent melts is particularly difficult to attain with the molecular simulation techniques available today, due to the long simulation times and atomistic-level detail needed to observe such phenomena. Extensive studies have been dedicated to characterizing melting and crystallization of *n*-alkanes under equilibrium conditions using Molecular Dynamics [47, 68-74] or Monte Carlo [67, 75, 76] techniques. Even for the relatively short alkane chains, the simulation times needed to observe ordered phase formation are on the order of tens of nanoseconds, which is prohibitive on most supercomputers today. To this end, alternative methods have been proposed in order to enhance the crystallization rates, which include crystallization in the presence of a surface [66] or increasing the melting point by driving the system away from equilibrium via uniaxial stretching [70, 77, 78] or shear flow [47-49].

In rheology, there are two major types of flow: elongational flow and shear flow. For shear flow, there have been several successful attempts at developing Nonequilibrium Molecular Dynamics (NEMD) algorithms for simulating rheological and structural properties of chain molecules. Phenomena such as shear thickening, associated with crystalline structure formation under extreme shear rates, have also been reported [47, 49]. For elongational flow, however, the situation is different. It was not until recently [50, 51, 79, 80] that a theoretically sound algorithm (called "*p*-SLLOD") was developed. It was shown that *p*-SLLOD is suitable for simulating any type of flow in general, and planar elongational flow (PEF), in particular. For shear flow, early studies employed the SLLOD algorithm [48, 49], but as clearly shown in Ref. [51], *p*-SLLOD and SLLOD are equivalent in this flow.

Some recent studies focused on characterizing the crystallization behavior of oriented *n*-alkane melts [66, 70, 78] by means of uniaxial stretching. It should be noted, however, that no rigorous NEMD algorithm capable of steady state simulation was employed in any of these studies. The uniaxial stretching was accomplished by applying an artificial stress in one preferred direction for a short period of time (usually on the order of one nanosecond). By doing this, the Newtonian dynamics were altered and any physical quantity measured during this time frame would be subject to doubt. That is probably the reason why the authors only applied this stretching technique in order to obtain "stretched amorphous configurations", and all meaningful physical quantities were measured after the applied stress was turned off. While providing valuable insight upon crystallization mechanisms and kinetics at various temperatures and for various

chain lengths after the applied stress stopped, these methods are merely equilibrium molecular dynamics simulations using stretched initial configurations.

4.2 Methodology

In the present study, we have employed a proper NEMD algorithm, and the transition to the crystalline-like structure was observed during steady-state PEF; therefore, the present case is much more relevant to a real physical situation of flow-induced crystallization at a constant temperature above the melting point.

Aspects concerning the simulation method and algorithm, as well as the potential model used to describe the interactions between the atomistic chains, have been presented in great detail in a series of papers [50, 51, 79, 80]. It should be noted, however, that the cited work dealt with measuring rheological properties of decane, hexadecane, and tertacosane, while in the present study we focus our attention on the structural properties of eicosane, and comparison with experimental x-ray diffraction data for both the liquid and crystalline states.

In a typical x-ray diffraction experiment, the quantity measured is the static structure factor, $s(k)$. The structure factor is of particular importance to molecular simulation, because its Fourier transform gives the total pair correlation function, $g(r)$, through the equation

$$g(r) = 1 + \left(2\pi^2 r\rho_0\right)^{-1} \int_0^\infty k\left(s(k) - 1\right)\sin(kr)\mathrm{d}k \tag{4.1}$$

where k is the wave number and ρ_0 is the particle number density.

The total pair correlation function, $g(r)$, is a quantity readily available from any molecular level simulation, and, conversely, it can be transformed to obtain the static structure factor through the equation

$$s(k) = 1 + \frac{4\pi\rho_0}{k}\int_0^\infty r\left(g(r)-1\right)\sin(kr)\mathrm{d}r \qquad (4.2)$$

Thus, equations 4.1 and 4.2 allow us to compare directly, structural information obtained from simulation and x-ray diffraction experiments.

4.3 Results and Discussion

First, let us examine the liquid structure of *n*-eicosane predicted by simulation under equilibrium conditions. In Figure 4.1, the simulated static structure factor computed as the Fourier transform of the total pair correlation function, $g(r)$, (eq. 4.2) is shown. We make a distinction here between the total pair correlation function $g(r)$ (Figure 4.2a), and the inter-molecular pair correlation function $g\_inter(r)$ (Figure 4.2b). For $g(r)$, the distance distribution is computed between pairs involving all sites (CH_2 groups) in the system, while for $g\_inter(r)$, distances between pairs of sites belonging to the same chain were excluded. Consequently, there are two structure factors associated with each pair correlation function, the total structure factor, $s(k)$ (Figure 4.3a), and the inter-molecular structure factor, $s\_inter(k)$ (Figure 4.3b).

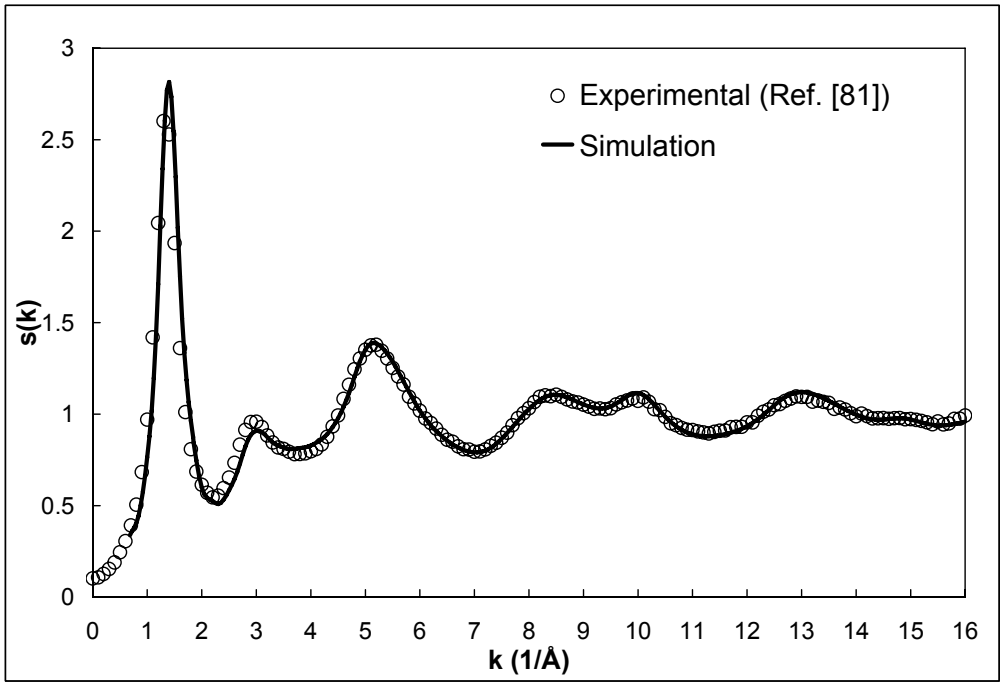

Figure 4.1: *Comparison of the structure factor, s(k), comparison between experiment (Ref. [81]) and simulation under quiescent conditions at T = 315 K and ρ = 0.81 g/cm^3.*

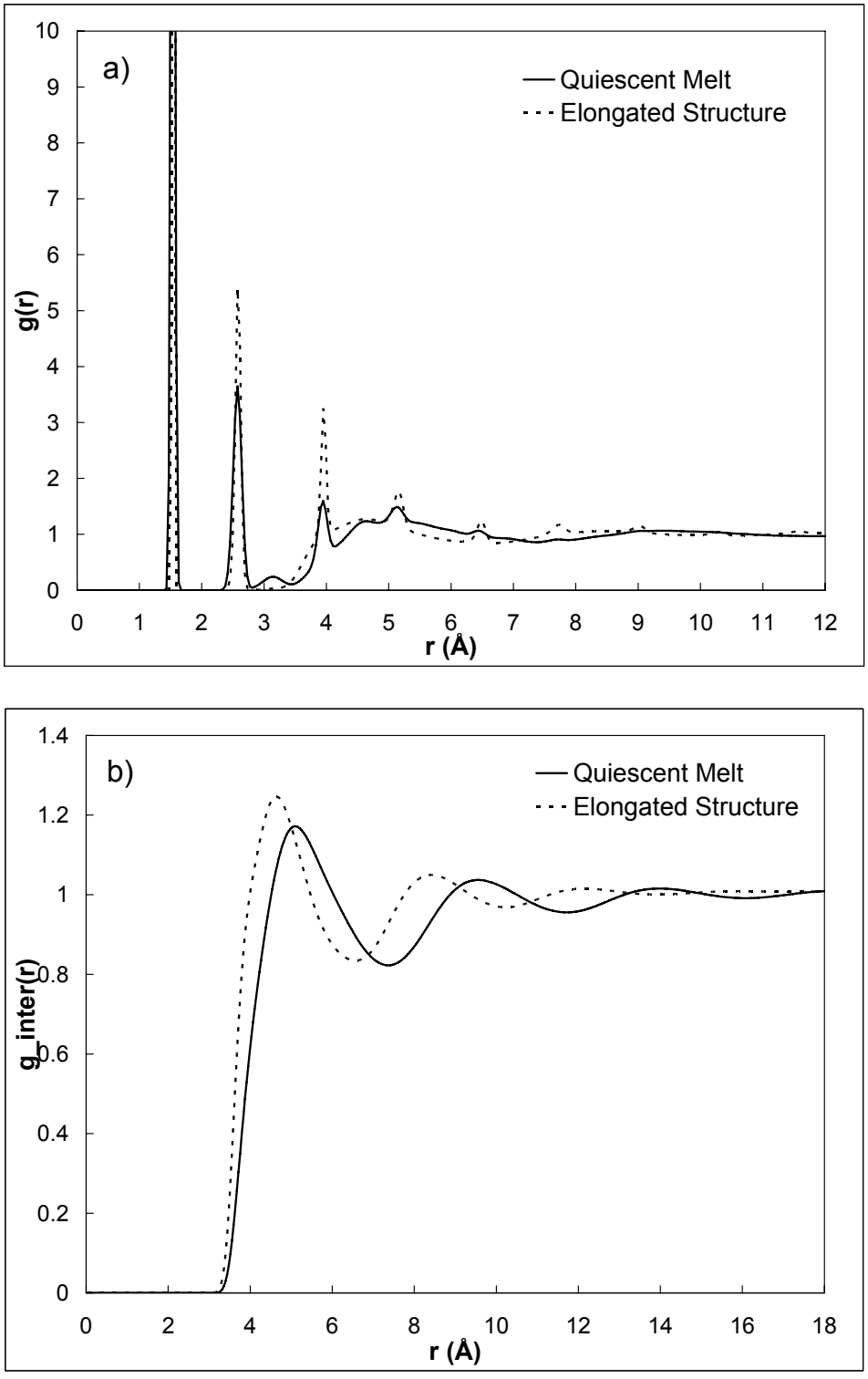

Figure 4.2: *Simulated structures in terms of: total pair correlation function g(r) a); intermolecular pair correlation function g_inter(r) b) at T = 315K and ρ = 0.81 g/cm^3.*

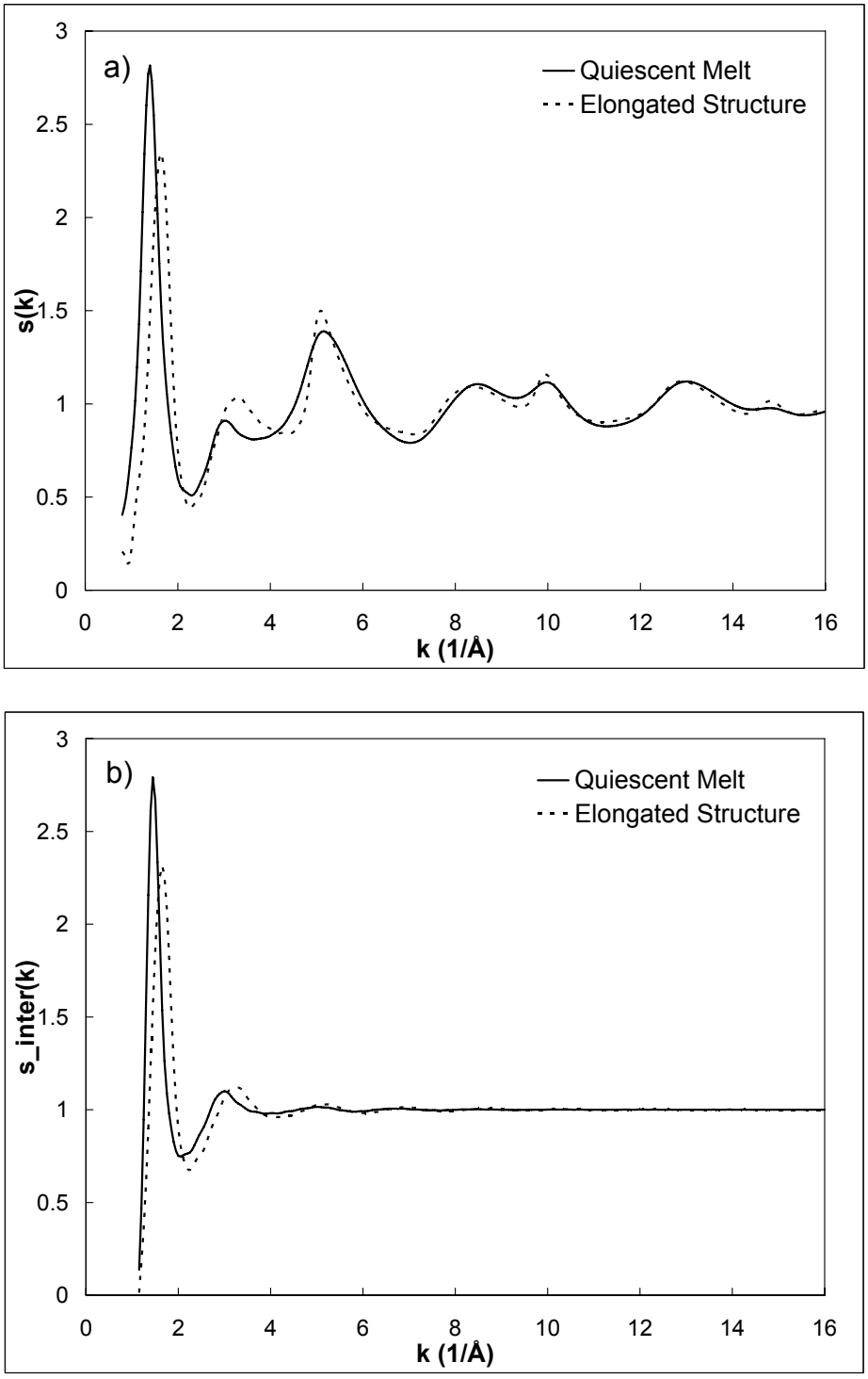

Figure 4.3: *Simulated structures in terms of: total static structure factor s(k) a);intermolecular static structure factor s_inter(k) b) at T = 315K and ρ = 0.81 g/cm^3.*

The liquid *n*-eicosane was simulated in the *NVT* ensemble, where the total number of particles, *N*, the simulation box volume, *V*, and the temperature, *T*, are kept constant. In Figure 4.1, comparison is made with existing x-ray scattering data for liquid *n*-eicosane [81]. The simulation was performed employing 200 eicosane molecules in the cubic box with each side of 48.7 Å at the same state point as the experiment (T = 315 K and ρ = 0.81 g/cm^3). As clearly shown in Figure 4.1, we see an excellent agreement between the simulated and experimentally determined liquid structures.

Let us now examine the structure when the flow field is turned on at steady state, at a reduced elongation rate $\dot{\varepsilon}(m\sigma^2/\varepsilon)^{1/2}$=1.0. Here, $\dot{\varepsilon}$ denotes the elongation rate, *m* mass of the CH_2 group, σ and ε, respectively, the size and energy parameters of the CH_2 group in the Lennard-Jones potential. It is worth pointing out that the temperature and density were maintained constant throughout the flow simulation at T = 315K and ρ = 0.81 g/cm^3, respectively; thus any differences we see are due neither to temperature nor density changes, but to structural rearrangements. For the NEMD simulation, we employed 648 eicosane molecules using a non-cubic box, since *x*-and *y*-dimensions are contracting and extending with time (after applying the initial orientation angle), and chains are aligned and extended in those directions. The box dimension ($x\times y\times z$ in unit of Å) of 90.4×90.4×47.2 was chosen, in particular for *x*-and *y*-dimensions, to be much larger than the fully-stretched chain length with the *trans*-conformation of 24.5 Å for $C_{20}H_{42}$ in order to eliminate any system-size effect.

In Figures 4.2a) and 4.2b), we present the total and inter-molecular pair correlation functions $g(r)$ and $g\_inter(r)$ respectively, under quiescent and steady-state

flow conditions. In Figure 4.2a), it is readily observed that the peak at 3.16 Å in the total pair correlation function for the quiescent melt has completely vanished in the elongated structure. This peak is associated with the 1-4 pair distance on the same chain in the *gauche* conformation, and its disappearance is indicative that the chains have adopted the all-*trans* fully extended conformation. This fact is also supported by the heightening of the peak at 3.94 Å, which is associated with the 1-4 pair distance on the same chain in the *trans* conformation. On the same note, the 1-2 and 1-3 peaks at 1.54 Å and 2.58 Å, respectively, also present significant narrowing and increase in height. This is a clear indication that the distribution around the respective equilibrium distances is narrowed in the elongated state. These facts represent the first indication of a transition to a crystalline-like precursor state where the individual molecular chains take on conformations very similar to those in the solid phase. Moreover, the narrowing of the peaks is indicative of a freezing-out of the low wavelength vibrational degrees of freedom, another shift toward a solid phase. Evidence in the form of the decrease in the vibrational energy as a function of elongation rate for decane, hexadecane, and tertacosane corroborates this statement [50]. In Fig. 4.2b), one notices that all inter-molecular peaks have shifted towards lower distances and heightened in the elongated state compared to the quiescent melt. This is very important, and is indicative of closer lateral packing distances between neighboring chains. As a reminder, both pair correlation functions in Fig. 4.2b) were generated under the same temperature and density conditions, thus the differences arise solely from structural rearrangements.

Mirroring the pair correlation functions (Figures 4.2a and 4.2b), we focus our attention now on the total and inter-molecular static structure factors (Figures 4.3a and 4.3b, respectively). We readily observe the shift of the first peak at k = 1.4 in the equilibrium melt structure towards a higher value (k=1.65) in the elongated state. As Figure 4.3a) clearly shows, this peak is solely associated with inter-molecular distances, and the shift mirrors the shift in the first peak in Fig. 4.2b).

With the view of comparing the simulated structure factor for the elongated structures to the measured one for the crystal, we undertook x-ray scattering measurements from *n*-eicosane in the solid state. The *n*-eicosane, $C_{20}H_{42}$, from Aldrich [82], was measured at room temperature (melting point 36-38 °C), and the x-ray measurements were in reflection geometry using MoK_α radiation (λ = 0.71069 Å). The range of scattering angles covered the interval $0.16 < k < 16 Å^{-1}$, where $k = (4\pi/\lambda)\sin\theta$, with 2θ the scattering angle. Corrections for background, absorption [83], polarization, incoherent scattering [84], detector energy discrimination [85], and multiple scattering [86] were applied.

Following the procedure for the analysis of the *n*-eicosane melt [81], the corrected, measured scattering pattern of the crystalline material was normalized to the scattering expected from uncorrelated, independent scattering sites CH_3 and CH_2 . We use "united atom" scattering factors for CH_3 and CH_2 [31], since the simulations were performed using united atom sites.

The structure factor, $s(k)$, for the crystalline material is compared to the melt in Fig. 4.4a). The sharp Bragg peaks below $k = 6 Å^{-1}$ have been indexed in a triclinic unit

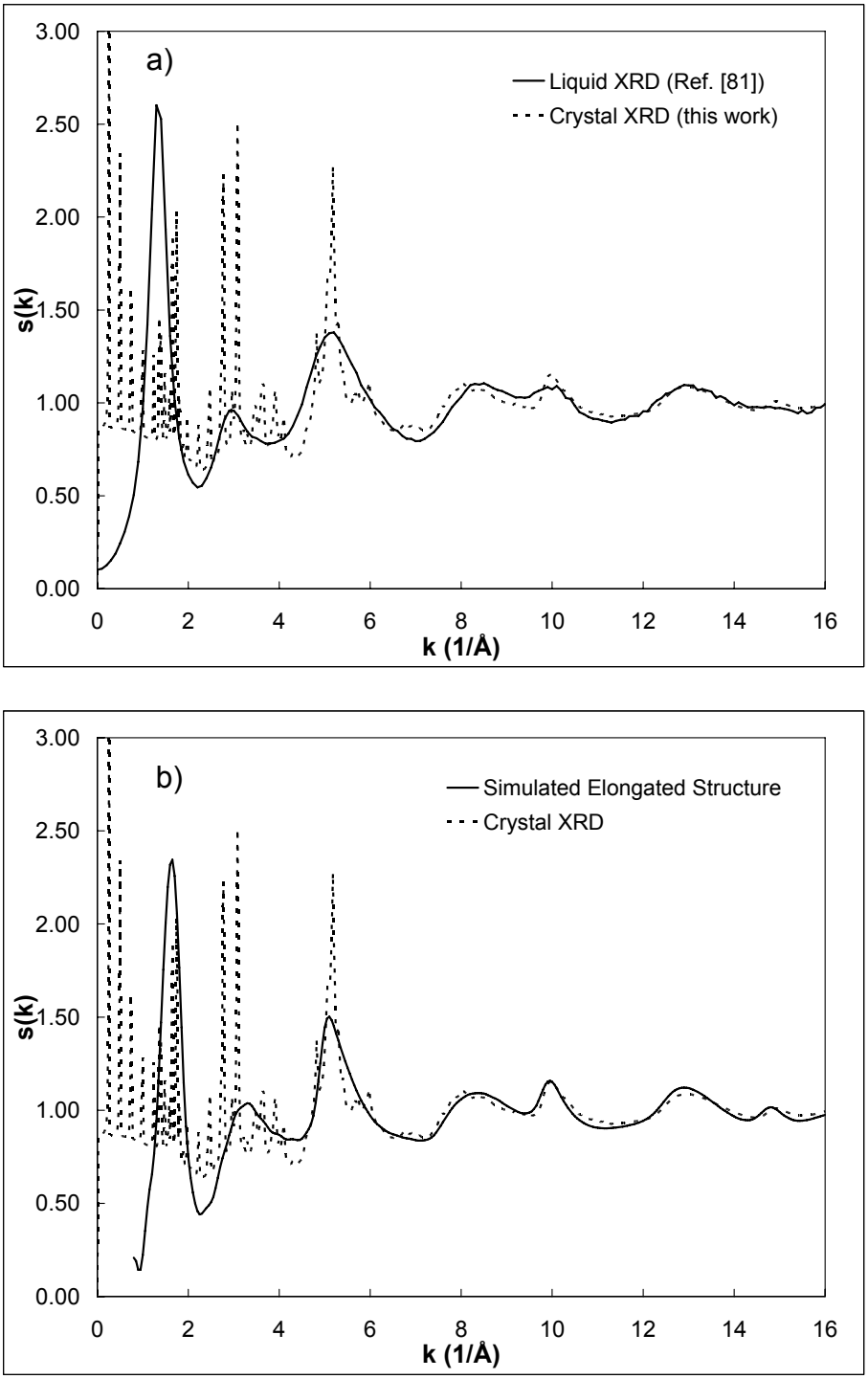

Figure 4.4: *Structure comparison in terms of x-ray diffraction data between liquid (Ref. [81]) and crystalline n-eicosane a); structure comparison in terms of total static structure factor between x-ray diffraction data for the crystalline n-eicosane and the simulated elongated structure b).*

cell, and the unit cell parameters obtained by least-squares refinement [87] of 22 reflections are a = 4.322(9) Å, b = 4.799(10) Å, c = 27.43(5) Å, α = 84.98(35)°, β = 67.48(23)º, γ = 72.03(28)°, V = 499.6 Å^3. These are in good agreement with literature values [88].

The dominant contributions to the structure factors at large k (> ~6 Å^{-1}), for both the melt and the crystalline material, are from the local intra-molecular structure. These intra-molecular contributions consist of correlations between sites within the molecular chain; that is, from bonded carbon atoms, C1-C2, C1-(C2)-C3, C1-(C2-C3)-C4, etc. These correlations determine the short-range order of the molecular chains, in the sense that correlations C1-C4 and higher depend on the internal rotations along the carbon chain. The C1-C2 distance is simply the carbon-carbon bond distance in the chain; the C1-C3 distance is determined by the C1-C2 bond distance and the C1-C2-C3 bond angle; for the C1-C4 correlation distances we can have values that correspond to *trans (t)* and *gauche (g)* conformations; for the C1-C5 correlations we can have distances corresponding to *tt*, *tg*, and *gg* conformations, and so on.

Clearly, for the *n*-eicosane melt, we should have an equilibrium between the *trans* and *gauche* conformations determined by the rotational potential of the C-C bond. In the case of the crystalline material, the molecular chains are forced into an all-*trans* conformation dictated by the crystal structure. So these differences in the melt and crystalline intra-molecular structure will appear in the high-k region of the structure factor. Beyond the Bragg peaks, the structure factors for the melt and the crystalline material in Fig. 4.4a) differ significantly. The crystal structure factor shows sharper

features at 5 $Å^{-1}$, 10 $Å^{-1}$ and 15 $Å^{-1}$, and overall, all the peaks are asymmetric compared to the melt. This is also in quantitative agreement with simulation, as it is readily observable in Figures 4.3a) and 4.4b).

4.4 Concluding Remarks

To conclude, the local intramolecular structure has been found to be in very good quantitative agreement with the actual crystalline structure of *n*-eicosane. The molecules adopt the all-*trans* fully stretched conformations, with closer lateral chain packing distances. However, we found no evidence of global long-range order, which would qualify the elongated structures as a truly crystalline structure. However, the excellent agreement between simulation and experiment for $k > 5$ $Å^{-1}$ suggests that the individual chains have taken on conformations consistent with a precursor structure to the crystalline phase. The lack of global long-range order might be due to the simulation technique, where the structure has not been allowed to relax under a constant pressure algorithm; i.e., the volume change between the liquid and solid phases has not been allowed. Moreover, the applied planar elongational deformation rate might also be too low for the long-range order to form; i.e., the simulation is limited at high elongational rates by thermostat artifacts.

Chapter 5

Conclusions and Directions for Future Work

5.1 Summary

The underlying theme of this dissertation was to investigate the nature of the elastic energy stored by polymer melts subjected to deformation using experimental measurements, molecular theory and simulation. Contrary to common beliefs, our model polymer (polyethylene) was found to show strong energetic effects when subjected to uniaxial elongational stretching.

This study may be broken down into three parts. The first part focused on extending an existing experimental method for testing the nature of the elastic energy stored by a polymer melt, but this time under processing conditions closer to what one would expect to find in an industrial setting. The balance equation used to model the flow process was derived under less restrictive assumptions than in the original experiments (but purposely keeping the *Purely Entropic Elasticity* assumption). Our experimental measurements showed significant deviations from the model equation. Next, molecular theory was used to isolate the cause of the deviations observed in the

experimental part, and it was concluded that the PEE assumption was solely responsible for the differences observed. Moreover, using the Upper-Convected Maxwell Model, the PEE assumption was removed and a new form of the temperature equation was proposed. This new model equation was found to bring significant improvements over the classical form. To further refine the UCMM predictions, the single-mode Giesekus model was introduced and its single parameter was adjusted to faithfully reproduce the experimental measurements. To the best of our knowledge, we are the first to report reliable experimental evidence that the assumption of PEE is not universally valid for polymer melts under a wide range of processing conditions.

The purpose of the second part of the dissertation was to provide molecular level insights into the reasons why the assumption of PEE would not be valid for polymer melts. To this aim, atomistic molecular simulations of oriented long alkane melts were performed using an existing Non-equilibrium Monte-Carlo (NEMC) procedure. First, it was found that for the oriented melts, the changes in free and internal energy with respect to the quiescent state were similar in magnitude. Next, the internal energy change was broken down into its constituents and it was concluded that the most important contributor to the overall energetic balance of the system is the "inter-molecular" non-bonded energy. This aspect has been overlooked in existing theories, which described the elastic response of a polymer *melt* based upon the elastic response of *single* polymer chains.

The third part of the dissertation was aimed at filling a void in the fundamental research of "flow-induced crystallization" phenomena. We were the first to report

crystalline-like structure formations under *steady-state* planar elongational flow of long chain molecules. This was accomplished by analyzing the structures generated under non-equilibrium conditions via calculations of the x-ray diffraction patterns. The simulated structures were then compared to the experimentally determined crystalline structure of the same material. The agreement found between the simulated and experimentally determined intra-molecular structures was excellent.

5.2 Directions for Future Research

The work presented in this study has indeed clarified some important aspects concerning the non-isothermal flow of polymer melts. Given the large number of industrial applications involving non-isothermal flow of polymeric materials, it is our belief that the present study will pave the way for more research in this area. In the future, it would be useful to extend the present study to more polymers and processing conditions. Also, the effect of the molecular characteristics of the polymers would be interesting to investigate, such as molecular weight, polydispersity, branching, stiffness etc. There is room for improvement in the theoretical aspect this work as well. It would be interesting to explore more sophisticated viscoelastic models. The UCMM employed in this study has been shown in the past to predict the correct properties only at low deformation rates. Even so, the UCMM did an excellent job in describing the measured temperature profiles.

In Chapter 4, it was suggested that one of the possible reasons why long range order was not observed during the simulations was the fact that the density was fixed. In reality, crystallization is associated with a sudden density increase due to closer packing distances between neighboring molecules. Currently, there is a constant pressure version of the NEMD algorithm under development in our group, which should be able to capture the density change associated with the alignment of the molecules. Moreover, in order to bridge the gap between the relatively short chain simulated system and real polymers, longer chains need to be investigated. Also, it would be interesting to see x-ray diffraction experiments that capture the formation of the oriented structures *in situ*, under flowing conditions.

BIBLIOGRAPHY

Bibliography:

1. Dressler, M., B.J. Edwards, and H.C. Ottinger, *Macroscopic thermodynamics of flowing polymeric liquids.* Rheologica Acta, 1999. **38**(2): p. 117-136.

2. Dressler, M., *The Dynamical Theory of Non-Isothermal Polymeric Materials*. 2000, ETH: Zurich.

3. Delhommelle, J., *Should "lane formation" occur systematically in driven liquids and colloids?* Physical Review E, 2005. **71**(1).

4. Petravic, J. and J. Delhommelle, *Nonequilibrium molecular dynamics simulations of molten sodium chloride.* International Journal of Thermophysics, 2004. **25**(5): p. 1375-1393.

5. Treloar, L.R.G., *The Physics of Rubber Elasticity*. 3rd ed. 2005, Oxford: Clarendon Press.

6. Coleman, B.D., *On Thermodynamics, Strain Impulses, and Viscoelasticity.* Archive for Rational Mechanics and Analysis, 1964. **17**(3): p. 230-254.

7. Coleman, B.D., *Thermodynamics of Materials with Memory.* Archive for Rational Mechanics and Analysis, 1964. **17**(1): p. 1-46.

8. Ferry, J.D., *Viscoelastic Properties of Polymers*. 1961: John Wiles and Sons, Inc.

9. Astarita, G., *Thermodynamics of Dissipative Materials with Entropic Elasticity.* Polymer Engineering and Science, 1974. **14**(10): p. 730-733.

10. Astarita, G. and G.C. Sarti, *Dissipative Mechanism in Flowing Polymers - Theory and Experiments.* Journal of Non-Newtonian Fluid Mechanics, 1976. **1**(1): p. 39-50.

11. Sarti, G.C. and N. Esposito, *Testing Thermodynamic Constitutive Equations for Polymers by Adiabatic Deformation Experiments.* Journal of Non-Newtonian Fluid Mechanics, 1977. **3**(1): p. 65-76.

12. Astarita, G. and G.S. Sarti, *Approach to Thermodynamics of Polymer Flow Based on Internal State Variables.* Polymer Engineering and Science, 1976. **16**(7): p. 490-495.

13. Nakajima, K., H. Watabe, and T. Nishi, *Single polymer chain rubber elasticity investigated by atomic force microscopy.* Polymer, 2006. **47**(7): p. 2505-2510.

14. Ortiz, C. and G. Hadziioannou, *Entropic elasticity of single polymer chains of poly(methacrylic acid) measured by atomic force microscopy.* Macromolecules, 1999. **32**(3): p. 780-787.

15. Lu, Z.Y., W. Nowak, G.R. Lee, P.E. Marszalek, and W.T. Yang, *Elastic properties of single amylose chains in water: A quantum mechanical and AFM study.* Journal of the American Chemical Society, 2004. **126**(29): p. 9033-9041.

16. Shi, W.Q., Y.H. Zhang, C.J. Liu, Z.Q. Wang, X. Zhang, and Y.M. Chen, *Toward understanding the effect of substitutes and solvents on entropic and enthalpic elasticity of single dendronized copolymers.* Polymer, 2006. **47**(7): p. 2499-2504.

17. Bedrov, D. and G.D. Smith, *The role of local conformations in the stretching of a poly(ethylene oxide) chain in solution.* Journal of Chemical Physics, 2003. **118**(14): p. 6656-6663.

18. Smith, J.S., D. Bedrov, G.D. Smith, and E.M. Kober, *Thermodynamic and conformational changes upon stretching a poly(dimethylsiloxane) chain in the melt.* Macromolecules, 2005. **38**(19): p. 8101-8107.

19. Ionescu, T.C., C. Baig, B.J. Edwards, D.J. Keffer, and A. Habenschuss, *Structure formation under steady-state isothermal planar elongational flow of n-eicosane: A comparison between simulation and experiment.* Physical Review Letters, 2006. **96**(3).

20. Beris, A.N. and B.J. Edwards, *Thermodynamics of Flowing Systems With Internal Microstructure*, ed. O.U. Press. 1994, Oxford.

21. Meissner, J. and J. Hostettler, *A New Elongational Rheometer for Polymer Melts and Other Highly Viscoelastic Liquids.* Rheologica Acta, 1994. **33**(1): p. 1-21.

22. Meissner, J., *Experimental Aspects in Polymer Melt Elongational Rheometry.* Chemical Engineering Communications, 1985. **33**(1-4): p. 159-180.

23. Meissner, J., *Development of a Universal Extensional Rheometer for Uniaxial Extension of Polymer Melts.* Transactions of the Society of Rheology, 1972. **16**(3): p. 405-&.

24. Feigl, K., F. Tanner, B.J. Edwards, and J.R. Collier, *A numerical study of the measurement of elongational viscosity of polymeric fluids in a*

semihyperbolically converging die. Journal of Non-Newtonian Fluid Mechanics, 2003. **115**(2-3): p. 191-215.

25. Collier, J.R., *US Patent 5,357,784*. 1994.

26. Collier, J.R., O. Romanoschi, and S. Petrovan, *Elongational rheology of polymer melts and solutions.* Journal of Applied Polymer Science, 1998. **69**(12): p. 2357-2367.

27. Petrovan, S., J.R. Collier, and G.H. Morton, *Rheology of cellulosic N-methylmorpholine oxide monohydrate solutions.* Journal of Applied Polymer Science, 2000. **77**(6): p. 1369-1377.

28. Kamerkar, P.A. and B.J. Edwards, *An Experimental Study of Slip Flow in Capillary and Semi-hyperbolically Converging Dies.* Polymer Engineering and Science, 2006(accepted for publication).

29. Choy, C.L., W.H. Luk, and F.C. Chen, *Thermal-Conductivity of Highly Oriented Polyethylene.* Polymer, 1978. **19**(2): p. 155-162.

30. Bird, R.B., R.C. Armstrong, and O. Hassager, *Dynamics of Polymeric Liquids*. Second Edition ed. Vol. Volume 1: Fluid Mechanics. 1987, New York: John Wiley & Sons, Inc.

31. Bird, R.B., W.E. Stewart, and E.N. Lightfoot, *Transport Phenomena*. Second Edition ed. 2001, New York: John Wiley & Sons, Inc.

32. COMSOL, *FEMLAB 3.0*. 2004.

33. *Polymer Handbook*. 1999, New York: Wiley Interscience.

34. Choy, C.L., Y. Fei, and T.G. Xi, *Thermal-Conductivity of Gel-Spun Polyethylene Fibers.* Journal of Polymer Science Part B-Polymer Physics, 1993. **31**(3): p. 365-370.

35. Dai, S.C. and R.I. Tanner, *Anisotropic thermal conductivity in sheared polypropylene.* Rheologica Acta, 2006. **45**(3): p. 228-238.

36. Hands, D., *The Effect of Biaxial Orientation on the Thermal-Conductivity of Vulcanized and Un-Vulcanized Rubber.* Rubber Chemistry and Technology, 1980. **53**(1): p. 80-87.

37. Iddir, H., D.C. Venerus, and J.D. Schieber, *Measuring anisotropic thermal conduction in polyisobutylene following step shear strains.* Aiche Journal, 2000. **46**(3): p. 610-615.

38. Kurabayashi, K., *Anisotropic thermal properties of solid polymers.* International Journal of Thermophysics, 2001. **22**(1): p. 277-288.

39. Venerus, D.C., J.D. Schieber, V. Balasubramanian, K. Bush, and S. Smoukov, *Anisotropic thermal conduction in a polymer liquid subjected to shear flow.* Physical Review Letters, 2004. **93**(9).

40. Venerus, D.C., J.D. Schieber, H. Iddir, J. Guzman, and A. Broerman, *Anisotropic thermal diffusivity measurements in deforming polymers and the stress-thermal rule.* International Journal of Thermophysics, 2001. **22**(4): p. 1215-1225.

41. Venerus, D.C., J.D. Schieber, H. Iddir, J.D. Guzman, and A.W. Broerman, *Measurement of thermal diffusivity in polymer melts using forced Rayleigh light scattering.* Journal of Polymer Science Part B-Polymer Physics, 1999. **37**(11): p. 1069-1078.

42. Venerus, D.C., J.D. Schieber, H. Iddir, J.D. Guzman, and A.W. Broerman, *Relaxation of anisotropic thermal diffusivity in a polymer melt following step shear strain.* Physical Review Letters, 1999. **82**(2): p. 366-369.

43. Wallace, D.J., C. Moreland, and J.J.C. Picot, *Shear Dependence of Thermal-Conductivity in Polyethylene Melts.* Polymer Engineering and Science, 1985. **25**(2): p. 70-74.

44. Balasubramanian, V., K. Bush, S. Smoukov, D.C. Venerus, and J.D. Schieber, *Measurements of flow-induced anisotropic thermal conduction in a polyisobutylene melt following step shear flow.* Macromolecules, 2005. **38**(14): p. 6210-6215.

45. Vandenbrule, B., *A Network Theory for the Thermal-Conductivity of an Amorphous Polymeric Material.* Rheologica Acta, 1989. **28**(4): p. 257-266.

46. Ciferri, A., C.A.J. Hoeve, and P.J. Flory, *Stress-Temperature Coefficients of Polymer Networks and Conformational Energy of Polymer Chains.* Journal of the American Chemical Society, 1961. **83**(5): p. 1015-&.

47. Gray, R.A., P.B. Warren, S. Chynoweth, Y. Michopoulos, and G.S. Pawley, *Crystallization of Molecular Liquids through Shear-Induced Nucleation.* Proceedings of the Royal Society of London Series a-Mathematical and Physical Sciences, 1995. **448**(1932): p. 113-120.

48. Daivis, P.J., D.J. Evans, and G.P. Morriss, *Computer-Simulation Study of the Comparative Rheology of Branched and Linear Alkanes.* Journal of Chemical Physics, 1992. **97**(1): p. 616-627.

49. Morriss, G.P., P.J. Daivis, and D.J. Evans, *The Rheology of Normal Alkanes - Decane and Eicosane.* Journal of Chemical Physics, 1991. **94**(11): p. 7420-7433.

50. Baig, C., B.J. Edwards, D.J. Keffer, and H.D. Cochran, *Rheological and structural studies of liquid decane, hexadecane, and tetracosane under planar elongational flow using nonequilibrium molecular-dynamics simulations.* Journal of Chemical Physics, 2005. **122**(18).

51. Baig, C., B.J. Edwards, D.J. Keffer, and H.D. Cochran, *A proper approach for nonequilibrium molecular dynamics simulations of planar elongational flow.* Journal of Chemical Physics, 2005. **122**(11).

52. Pant, P.V.K. and D.N. Theodorou, *Variable Connectivity Method for the Atomistic Monte-Carlo Simulation of Polydisperse Polymer Melts.* Macromolecules, 1995. **28**(21): p. 7224-7234.

53. Mavrantzas, V.G. and D.N. Theodorou, *Atomistic simulation of polymer melt elasticity: Calculation of the free energy of an oriented polymer melt.* Macromolecules, 1998. **31**(18): p. 6310-6332.

54. Mavrantzas, V.G., T.D. Boone, E. Zervopoulou, and D.N. Theodorou, *End-bridging Monte Carlo: A fast algorithm for atomistic simulation of condensed phases of long polymer chains.* Macromolecules, 1999. **32**(15): p. 5072-5096.

55. Mavrantzas, V.G. and D.N. Theodorou, *Atomistic Monte Carlo simulation of steady-state uniaxial, elongational flow of long-chain polyethylene melts: dependence of the melt degree of orientation on stress, molecular length and elongational strain rate.* Macromolecular Theory and Simulations, 2000. **9**(8): p. 500-515.

56. Mavrantzas, V.G. and H.C. Ottinger, *Atomistic Monte Carlo simulations of polymer melt elasticity: Their nonequilibrium thermodynamics GENERIC formulation in a generalized canonical ensemble.* Macromolecules, 2002. **35**(3): p. 960-975.

57. Karayiannis, N.C., V.G. Mavrantzas, and D.N. Theodorou, *A novel Monte Carlo scheme for the rapid equilibration of atomistic model polymer systems of precisely defined molecular architecture.* Physical Review Letters, 2002. **88**(10).

58. Siepmann, J.I., S. Karaborni, and B. Smit, *Simulating the Critical-Behavior of Complex Fluids.* Nature, 1993. **365**(6444): p. 330-332.

59. Allen, M.P. and D.J. Tildesley, *Computer Simulation of Liquids*. 1987, Oxford: Oxford University Press.

60. Jorgensen, W.L., J.D. Madura, and C.J. Swenson, *Optimized Intermolecular Potential Functions for Liquid Hydrocarbons.* Journal of the American Chemical Society, 1984. **106**(22): p. 6638-6646.

61. Smith, W. and T.R. Forester, *DL_POLY_2.0: A general-purpose parallel molecular dynamics simulation package.* Journal of Molecular Graphics, 1996. **14**(3): p. 136-141.

62. Fetters, L.J., W.W. Graessley, R. Krishnamoorti, and D.J. Lohse, *Melt chain dimensions of poly(ethylene-1-butene) copolymers via small angle neutron scattering.* Macromolecules, 1997. **30**(17): p. 4973-4977.

63. Horton, J.C., G.L. Squires, A.T. Boothroyd, L.J. Fetters, A.R. Rennie, C.J. Glinka, and R.A. Robinson, *Small-Angle Neutron-Scattering from Star-Branched Polymers in the Molten State.* Macromolecules, 1989. **22**(2): p. 681-686.

64. Gupta, R.K. and A.B. Metzner, *Modeling of Non-Isothermal Polymer Processes.* Journal of Rheology, 1982. **26**(2): p. 181-198.

65. Liu, C. and M. Muthukumar, *Langevin dynamics simulations of early-stage polymer nucleation and crystallization.* Journal of Chemical Physics, 1998. **109**(6): p. 2536-2542.

66. Waheed, N., M.S. Lavine, and G.C. Rutledge, *Molecular simulation of crystal growth in n-eicosane.* Journal of Chemical Physics, 2002. **116**(5): p. 2301-2309.

67. Sadler, D.M. and G.H. Gilmer, *Rate-Theory Model of Polymer Crystallization.* Physical Review Letters, 1986. **56**(25): p. 2708-2711.

68. Meyer, H. and F. Muller-Plathe, *Formation of chain-folded structures in supercooled polymer melts examined by MD simulations.* Macromolecules, 2002. **35**(4): p. 1241-1252.

69. Esselink, K., P.A.J. Hilbers, and B.W.H. Vanbeest, *Molecular-Dynamics Study of Nucleation and Melting of N-Alkanes.* Journal of Chemical Physics, 1994. **101**(10): p. 9033-9041.

70. Koyama, A., T. Yamamoto, K. Fukao, and Y. Miyamoto, *Molecular dynamics studies on polymer crystallization from a stretched amorphous state.* Journal of Macromolecular Science-Physics, 2003. **B42**(3-4): p. 821-831.

71. Fujiwara, S. and T. Sato, *Molecular dynamics simulation of structure formation of short chain molecules.* Journal of Chemical Physics, 1999. **110**(19): p. 9757-9764.

72. Liao, Q. and X.G. Jin, *Formation of segmental clusters during relaxation of a fully extended polyethylene chain at 300 K: A molecular dynamics simulation.* Journal of Chemical Physics, 1999. **110**(17): p. 8835-8841.

73. Kavassalis, T.A. and P.R. Sundararajan, *A Molecular-Dynamics Study of Polyethylene Crystallization.* Macromolecules, 1993. **26**(16): p. 4144-4150.

74. Takeuchi, H., *Structure formation during the crystallization induction period of a short chain-molecule system: A molecular dynamics study.* Journal of Chemical Physics, 1998. **109**(13): p. 5614-5621.

75. Toma, L., S. Toma, and J.A. Subirana, *Simulation of polymer crystallization through a dynamic Monte Carlo lattice model.* Macromolecules, 1998. **31**(7): p. 2328-2334.

76. Xu, G.Q., H. Lin, and W.L. Mattice, *Configuration selection in the simulations of the crystallization of short polyethylene chains in a free-standing thin film.* Journal of Chemical Physics, 2003. **119**(13): p. 6736-6743.

77. Ko, M.J., N. Waheed, M.S. Lavine, and G.C. Rutledge, *Characterization of polyethylene crystallization from an oriented melt by molecular dynamics simulation.* Journal of Chemical Physics, 2004. **121**(6): p. 2823-2832.

78. Lavine, M.S., N. Waheed, and G.C. Rutledge, *Molecular dynamics simulation of orientation and crystallization of polyethylene during uniaxial extension.* Polymer, 2003. **44**(5): p. 1771-1779.

79. Baig, C., B.J. Edwards, D.J. Keffer, H.D. Cochran, and V.A. Harmandaris, *Rheological and structural studies of linear polyethylene melts under planar elongational flow using nonequilibrium molecular dynamics simulations.* Journal of Chemical Physics, 2006. **124**(8).

80. Edwards, B.J., C. Baig, and D.J. Keffer, *A validation of the p-SLLOD equations of motion for homogeneous steady-state flows.* Journal of Chemical Physics, 2006. **124**(19).

81. Habenschuss, A. and A.H. Narten, *X-Ray-Diffraction Study of Some Liquid Alkanes.* Journal of Chemical Physics, 1990. **92**(9): p. 5692-5699.

82. *Sigma-Aldrich Co., Aldrich catalog # 21, 927-4*.

83. Levy, H.A., P.A. Agron, and M.D. Danford, *X-Ray Diffractometry with Slightly Absorbing Samples.* Journal of Applied Physics, 1959. **30**(12): p. 2012-2013.

84. Cromer, D.T. and J.B. Mann, *Compton Scattering Factors for Spherically Symmetric Free Atoms.* Journal of Chemical Physics, 1967. **47**(6): p. 1892-&.

85. Narten, A.H. and H.A. Levy, *In Water: A Comprehensive Treatise*, ed. F. Franks. Vol. I. 1972, New York: Plenum.

86. Warren, B.E. and R.L. Mozzi, *Multiple Scattering of X-Rays by Amorphous Samples.* Acta Crystallographica, 1966. **21**: p. 459-&.

87. *Scintag refinement program in DMS/NT crystalography package*. 2001, ThermoARL, Inc.

88. Nyburg, S.C. and A.R. Gerson, *Crystallography of the Even N-Alkanes - Structure of C20h42.* Acta Crystallographica Section B-Structural Science, 1992. **48**: p. 103-106.

Appendix

Temperature Profile Calculations for Shear Flow in a Capillary Tube

Following the same procedure presented in Section 2.4, the FEM analysis was performed for shear flow generated in a capillary tube 1 mm in diameter and 25 mm in length. The polymer used was LDPE at the same inlet temperature points as in the elongational flow case (150°C, 170°C and 190°C). First, the shear viscosity was measured using ACER (see Section 2.3, equation 2.11). The temperature dependence of the shear viscosity was then determined using equation 2.12. The shear rates at the tube wall investigated (see equation 2.9) spanned between $150s^{-1}$ and $4500s^{-1}$. The modeling equation used to determine the spatial temperature distributions was the same as in the elongational flow case (equation 2.13), with the following modifications:

1. The heat generation term: $\left(\tau : \nabla v\right) = \eta_{shear}\dot{\gamma}^2$ (A.1)

2. The velocity profile: $v_r = 0\,;\; v_z = \dfrac{\Delta P R^2}{4\eta_{shear} L}\left(1 - \dfrac{r^2}{R^2}\right)$ (A.2)

where η_{shear} is the shear viscosity, $\dot{\gamma}$ is the shear rate, ΔP is the pressure drop along the length of the tube, R is the radius of the tube, L is the length of the tube and r is the axial position inside the tube. The shear rate was considered constant with respect to axial position and variable with respect to radial position, according to

$$\dot{\gamma} = \frac{\mathrm{d}v_z}{\mathrm{d}r} \tag{A.3}$$

In Figure A.1, the temperature profiles in terms of the change with respect to the inlet is presented for three selected shear rates for the HDPE melt at T_{in} = 170°C. We observe sharp radial temperature gradients developing towards the exit of the capillary tube as the shear rate is increasing, mainly because the heat generation term given by equation A.1 is increasing with radial position. Let us examine the case of the highest shear rate considered (4500 s^{-1}). For the exit cross-section, the temperature at the center is very close to the inlet and wall temperatures. As we move towards the wall, there is a temperature increase of over 20°C, followed by a sharp decrease at the wall. This behavior is easily explained upon close examination of the individual terms in the heat equation. At the center of the channel, the shear rate is zero; therefore the heat generation term is also zero. The heat conduction from the hotter domains is increasingly compensated by convection of colder fluid from the entrance as the shear rate is increased. The sharp radial temperature gradients propagate through the measuring device, and the temperature increase due to viscous effects would not be accurately captured by this particular experimental design. However, a different design in which the fluid coming out of the capillary tube is perfectly mixed would be able to capture these viscous heating effects. By contrast, the radial temperature profiles at the exit of the Hencky die in the elongational flow case are fundamentally different (see Figure 2.6b). Moreover, the velocity profiles at the die exit are different for the two type of flow. While in the shear flow case the axial velocity is a strong function of radial position (see equation A.2), in the elongational flow case the axial velocity is independent of radial position (see equation 2.16).

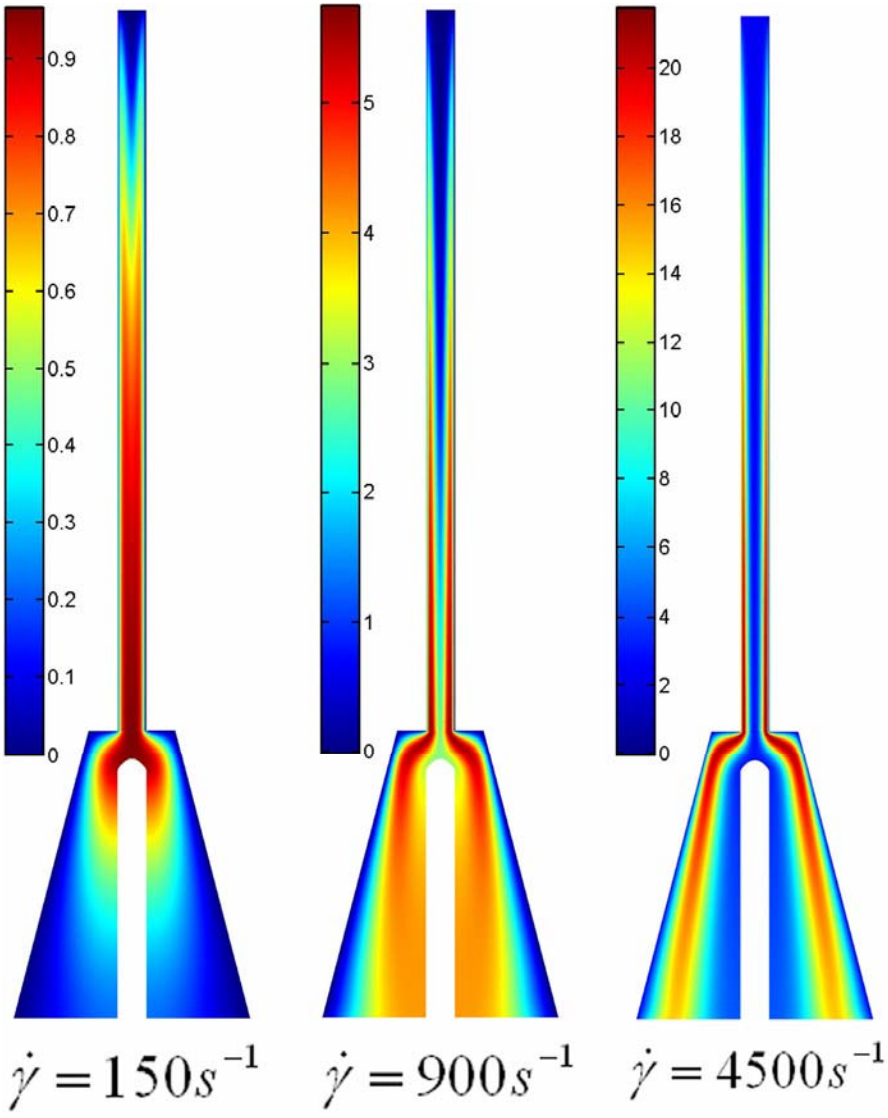

Figure A.1: *Temperature profiles in the measuring device for the shear flow of LDPE at T_{in} = 170°C.*

In Figure A.2, the temperature profiles inside the measuring device are shown for the elongational flow case for three selected flow rates for the LDPE melt at T_{in} = 170°C. Clearly, in the elongational flow case, the temperature increase is captured much more accurately by the tip of the thermocouple than in the shear flow case (Figure A.1). Given the different behaviors observed in Figures A.1 and A.2, we decided not to pursue the shear flow case any further. However, given the industrial importance of this particular type of flow, it would be interesting to improve this experimental design in the future and investigate the energetic effects generated through shear flow as well.

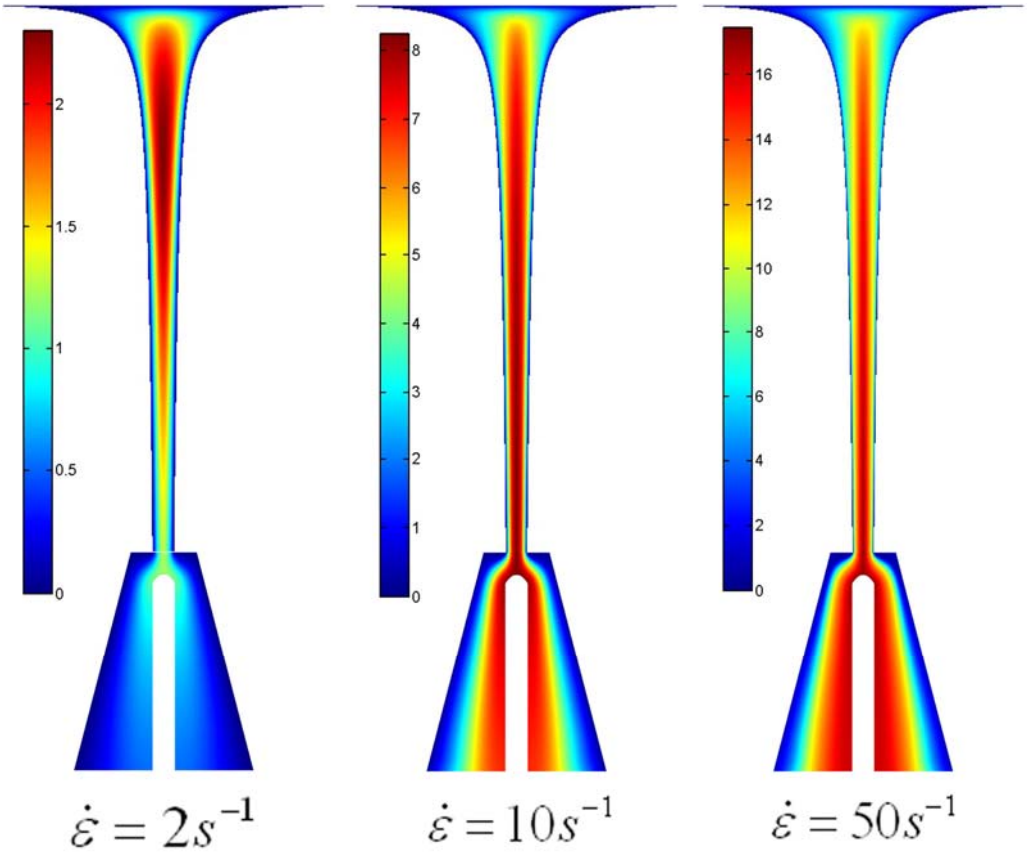

Figure A.2: *Temperature profiles in the measuring device for the elongational flow of LDPE at* T_{in} *= 170°C.*

Vita

Tudor Constantin Ionescu was born in Iaşi, Romania on May 6, 1977. He attended high school at "Emil Racoviță" high school in his hometown, from which he graduated in 1995. From there, he joined the Chemical Engineering Department at the Technical University "Gheorghe Asachi" Iaşi as an undergraduate student, and in 2001 graduated first in class with a BS degree in Polymer Science and Engineering. In 2001 he joined the Chemical Engineering Department at the University of Tennessee, Knoxville as a graduate student. In 2002 he moved to Vanderbilt University, and obtained his MS degree in Chemical Engineering in 2004. Currently, Tudor is pursuing his doctorate in Chemical Engineering at the University of Tennessee, Knoxville.